Novel Ir(III)-based Triplet Photosensitisers For Triplet-Triplet Annihilation Upconversion

Colin Caverly B.A. (Mod.)

A thesis submitted to the University of Dublin for the degree of Master of Science

School of Chemistry
Trinity College Dublin

February 2019

Declaration

I declare that this thesis has not been submitted as an exercise for a degree at this or any other university and it is entirely my own work.

I agree to deposit this thesis in the University's open access institutional repository or allow the library to do so on my behalf, subject to Irish Copyright Legislation and Trinity College Library conditions of use and acknowledgement.

_____

Colin Caverly B.A. (Mod.)

Acknowledgements

I would like to express my sincere thanks to my supervisor, Prof. Sylvia Draper, for giving me the opportunity to do this work and for all of her support throughout the process. I would also like to extend my sincerest thanks to Dr. John O'Brien, Dr. Manuel Rüether, Dr. Martin Feeney and Dr. Gary Hessman for their significant time and even more significant expertise in NMR and mass spectrometry analysis, without which I would most certainly not have been able to succeed at this work.

I also want to sincerely thank Prof. Jianzhang Zhao and his group, including Dr. Wanhua Wu, for their help, time and patience in allowing me to work in their labs and giving me all the help I needed in a completely new environment.

My sincerest thanks to the members of the Draper group, including Claire, Lukas, Raj, Martha, Nidhi, Bryan and Eugene for their support during my time there. I need to give special thanks to Yue, Junsi, Rob, Justo and Xiaoneng for taking so much time to help me when I needed it and being so patient and helpful to me.

Of course, I also want to thank my parents for their support, both nutritional and financial, and my friends and family for their support throughout. And lastly, to take a page out of the book of my first mentor, Yue, thanks to myself!

Summary

Chapter 1

This chapter contain introduction to the topic of triplet-triplet annihilation upconversion (TTA-UC), including the process of upconversion, the properties of efficient photosensitiser (PS) molecules and the other uses that these PS molecules may have. Also included is a brief literature review regarding the development of various PS molecules for upconversion. This chapter also covers the aims of the thesis, and the synthetic background used to create the novel Ir(III)-based PS molecules within.

Chapter 2

This chapter covers the synthesis of each complex, the difficulties encountered, and the attempts taken to circumvent these. Also covered is the structural characterisation of each complex using nuclear magnetic resonance (NMR) and mass spectrometry (MS).

Chapter 3

This chapter covers the photophysical investigations of **Ir1 – Ir4**, including UV-vis absorption, emission, singlet oxygen sensitisation, transient absorption, quenching and TTA-UC measurements. Also, the cyclic voltammetry measurements of Ir1 – Ir4 are described. Lastly, the extensive results of density functional theory (DFT) calculations into Ir1 – Ir4, and comparison of the calculated values to the experimentally determined analogues are detailed.

Chapter 4

Similarly to Chapter 3, this chapter covers the photophysical, cyclic voltammetric and DFT investigations into the dinuclear Ir5 and Ir6.

Chapter 5

This chapter gives a detailed account of each successful reaction carried out, including reagents, solvents, molar details, purification details and yields. The NMR, IR and melting point data of each product is also given here.

Table of Contents

Table of Figures

Table of Schemes

Table of Tables

Table of Abbreviations

Abbreviation	*Meaning*
A	Acceptor molecule
Ar	Argon
BODIPY	Boron-dipyrromethene
BPEA	9,10-bis(phenylethynyl)anthracene
bpy	2,2'-bipyridine
C6	Coumarin-6
CH_2Cl_2	Methylene chloride
$CHCl_3$	Chloroform
COSY	Correlation spectroscopy
CV	Cyclic voltammetry
DEP	1,6-diethynylpyrene
DEPT	Distortionless enhancement by polarisation transfer
DMF	Dimethylformamide
DNA	Deoxyribonucleic acid
DPA	Diphenylanthracene
DPBF	1,3-diphenylisobenzofuran
DSSC	Dye-sensitised solar cell
EP	1-ethynylpyrene
Et_3N	Triethylamine
EtOAc	Ethyl acetate
HMBC	Heteronuclear multiple-bond correlation
HOMO	Highest-occupied molecular orbitals
HRMS	High-resolution mass spectrometry
HSQC	Heteronuclear single quantum spectroscopy
IL	Intraligand
ILCT	Intraligand charge transfer
ISC	Inter-system crossing
K	Kelvin
KDP	Potassium Dihydrogen Phosphate
KSV	Stern-Volmer constant
LC	Ligand centred
LLCT	Ligand to ligand charge transfer
LMCT	Ligand to metal charge transfer
LUMO	Lowest-unoccupied molecular orbitals
MALDI	Matrix assisted laser desorption
MC	Metal-centred
MeCN	Acetonitrile
MeOH	Methanol
MLCT	Metal-to-ligand charge transfer
NaOH	Sodium hydroxide
NHSB	N-heterobenzocoronene

NIR	Near infrared
NMR	Nuclear magnetic resonance
OLED	Organic light-emitting diode
PDT	Photodynamic therapy
PEPA	9-(4-phenylethynyl)-10-phenylanthracene
phen	1,10-phenanthroline
ppy	2-phenylpyridine
PS	Photosensitiser
ROS	Reactive oxygen species
RT	Room temperature
S	Singlet state
S_2Cl_2	Sulphur monochloride
SDT	Sonodynamic therapy
SOC	Spin-orbit coupling
SS	Sonosensitiser
T	Triplet state
TDDFT	Time-dependent density functional theory
TLC	Thin-layer chromatography
TMSA	Trimethylsilylacetylene
TOCSY	Total correlation spectroscopy
TOF	Time of flight
TPA	Two-photon absorption
TTA	Triplet-triplet annihilation
TTET	Triplet-triplet energy transfer
UC	Upconversion
US	Ultrasound
UV	Ultraviolet
V	Volts
ε	Molar absorption coefficient
λ	Wavelength
Φ_{UC}	Upconversion quantum yield
Φ_{Δ}	Singlet oxygen sensitisation quantum yield

Chapter 1

Introduction

1.1 Upconversion

Upconversion is the process by which a system absorbs multiple photons of relatively low energy before combining their energy and emitting a single photon of high-energy light. It is a process which presents numerous opportunities for exploitation in the electronic, industrial, and energy sectors.[1-10] There are four main types of upconverting compounds which have been investigated to a significant extent. The first are inorganic crystals, such as potassium dihydrogen phosphate (KDP), but which are weakly absorbing across the desired range of wavelengths, thus severely limiting their efficiency. The second are rare earth element-based materials.[11, 12] These are also inefficient due to their narrow and characteristic ranges of absorption, but can include a range of $NaYF_4$ compounds doped with lanthanide ions (*e.g.* Yb^{3+}, Er^{3+}, *etc*.). The third type is a family of two-photon absorption (TPA) dyes, in which the main drawback is the initial power requirement - these dyes use high power density laser sources to achieve absorption of multiple photons per molecule in rapid succession, as the atomic transition rate depends on the square of the light intensity.

The final and most promising type of upconverting system is based on triplet photosensitiser (PS) molecules, coupled with an acceptor/annihilator molecule. These systems generally utilise heavy transition metal centres to induce spin-orbit coupling, such as Ru(II), Ir(III), Pd(II), and Pt(II). The mechanism at the heart of this process is called triplet-triplet annihilation upconversion (TTA-UC), and was first reported by Parker and Hatchard in the 1960's.[13-15] It does not require high energy densities in its power sources and tends to use molecules with strong visible and near-IR (NIR) absorptions. This makes it the most efficient of the upconversion processes, and is thus viable using solar energy sources. Solar irradiation at sea level provides 0.1 $W \cdot cm^{-2}$ of energy, while the excitation power requirement of TTA upconversion photosensitisers is often just a few $mW.cm^{-2}$.[16]

The issue of finding alternative and sustainable processes for energy generation has become more and more urgent. The climatic consequences of an over-reliance on fossil fuels coupled with the increased energy demands of a growing human population have prompted the need for action. Alternative renewable energy sources are being developed and implemented on larger and larger scales, however they need to be accelerated in order to avoid catastrophic and irreversible climate change, as well as to avert the risk of

frequent power shortages in the future. Each form of renewable or carbon-neutral energy has its own set of advantages and disadvantages. Wind is one of the most easily harnessed but is dependent on inclement weather, rendering it unreliable at times and increasing the need for high-volume battery storage facilities. Tidal and wave powers face the same issues, while hydroelectric power stations are costly and can have serious negative environmental impacts. Biomass (using biological material as fuel) produces carbon monoxide and dioxide, as well as nitrogen oxides, particulates and organic compounds amongst other atmospheric pollutants, making it sub-optimal as a long term energy source.[17, 18]

Solar energy is extremely desirable as it is generally reliable and plentiful. More solar irradiation arrives at the Earth's surface in under an hour than the total energy requirements of the planet for a year. However, harvesting this energy efficiently is difficult. To date it has relied largely on solar cells, either based on semiconductor materials or dye-sensitised nanoparticles.[19]

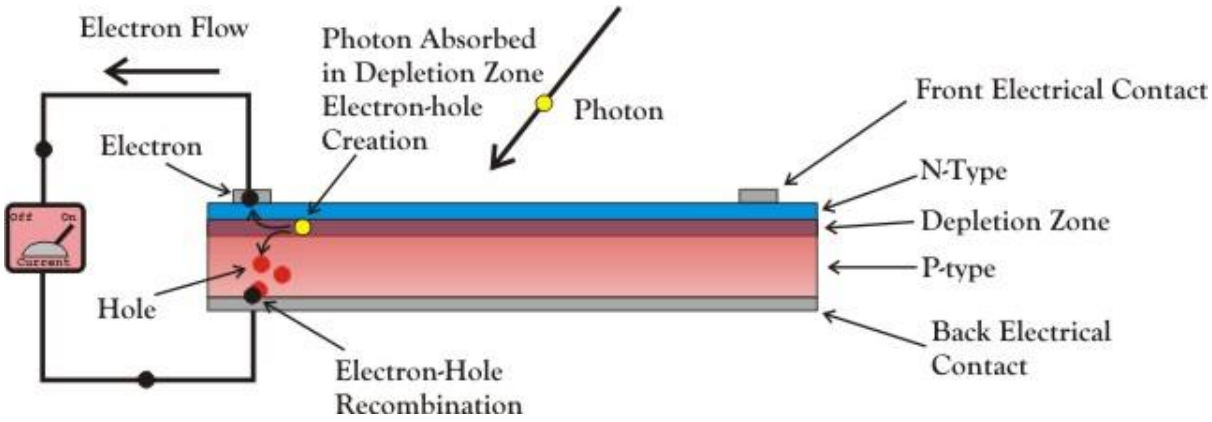

***Figure 1.1**: A typical semiconductor solar cell.[20] Some of the solar energy which reaches the cell causes electrons at the p-n junction to be excited. These are then free electrons, and their mobility results in positively charged holes in their former positions. Electrons are free to move within the N-layer, and holes in the P-layer. An external circuit can allow the flow of electrons from the N-layer to the P-layer without the need to traverse the barrier, generating an electrical current.*

Semiconductor solar cells (Figure 1.1) are the older and more costly of the two types of solar cells.[19] They rely on the excitation by solar light of electrons in a thick layer of doped silicon, specifically the depletion zone of the n-type layer, which are not able to recombine with holes in the p-type layer due to the existence of a charged depletion zone around the p-n junction. This can be remedied by connecting a circuit around the junction to allow the free movement of the excited electrons, which can then be used as an energy

source. The need for this thick layer of silicon increases the cost of these devices and cannot be avoided as thin layers do not absorb solar photons in sufficient yields. These silicon-based semiconductor solar cells must also contend with the Shockley-Queisser limit, a theoretically calculated yield of 30% energy conversion which the systems cannot exceed.[14]

The second type of system is the dye-sensitised solar cell (DSSC, Figure 1.2).[19] These rely on metal-organic dyes with strong absorption characters that are doped onto the surface of titanium dioxide nanoparticles. This increases the capture of solar photons and thus the overall energy yield. The dyes are cheaper than silicon-based systems, however they generally suffer from low absorption coefficients in the red and NIR regions of the spectrum, such that the absorption of solar light is limited to high-energy photons and the absorption quantum yield (Φ_{abs}) is quite low. TTA upconverting systems introduced into the porous nanoparticle layer can help to remedy this, by upconverting low-energy red and NIR photons to photons of blue and UV-region energy levels. The generated photons could be reabsorbed by the organic dyes, along with the directly absorbed solar photons.

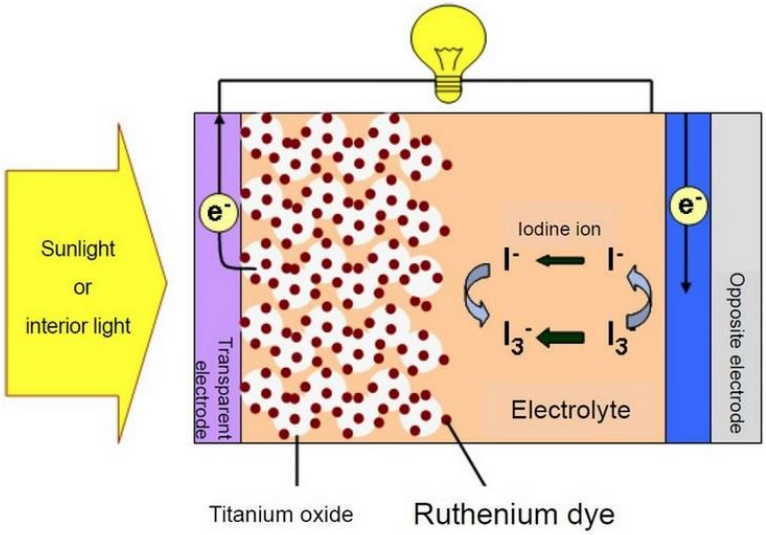

***Figure 1.2**: A DSSC showing the use of a ruthenium-based dye (i.e. triplet photosensitiser) on TiO_2 nanoparticles, and iodine as an electrolyte to complete the circuit.*[21]

1.1.1 TTA Upconversion

The process of TTA Upconversion is shown in Figure 1.3. Triplet photosensitising molecules can be excited to **S1** (shown in the Figure 1.3 as ^{1}MLCT*), in theory by red- or NIR-region photons, before undergoing an inter-system crossing (ISC) process to

eventually form a long-lived triplet excited state (^{3}MLCT*), promoted by the heavy atom effect (explained later in this section). This long-lived triplet excited state is then transferred *via* triplet-triplet energy transfer (TTET, a special case of Dexter energy transfer) to a triplet acceptor molecule (^{3}A*). This acceptor then accepts the excited energy of a second photosensitiser molecule *via* a collisional excimer in order to combine the energy of both and to form a high-energy singlet excited state. This higher excited singlet state can then relax to emit a single photon of higher energy than the original photons, *via* fluorescence.

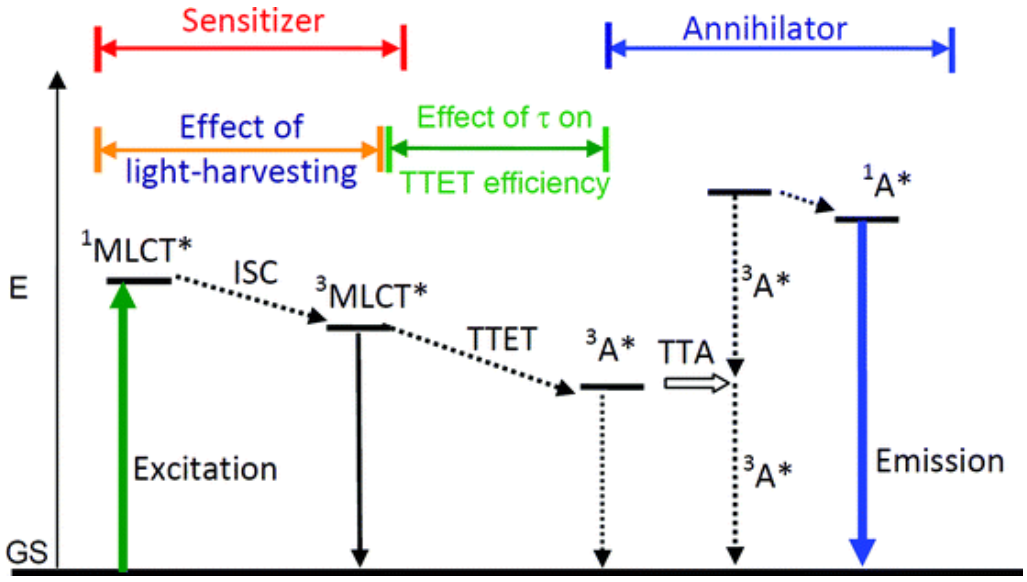

***Figure 1.3**: A qualitative Jablonski diagram exhibiting the photophysical processes of TTA-UC, and exhibiting the requirements for the relative energy levels of each excited state.*[22]

There are several important points to note about the processes and states involved.

- The photosensitisers must exhibit high molar absorption coefficients in the target absorption range in a solar cell (or at the excitation wavelength in the case of a laser test).

- Each excited state must be equal to or lower in energy to the previous excited state from which the energy was transferred, in order to allow the ISC and TTET processes to occur. This must fulfil the energetic requirement in Equation 1 below:

$$2 * E_{T_1} > E_{S_1}$$

Equation 1.1

The system has most often been researched in a liquid medium due to the collisional nature of the TTET process between the photosensitiser and acceptor molecules.

The quantum yield of upconversion can be calculated directly *via* the following equation:

$$\Phi_{UC} = \Phi_{ISC} * \Phi_{TTET} * \Phi_{TTA} * \Phi_{F}$$

Equation 1.2.

where Φ_{UC} is the upconversion quantum yield, Φ_{ISC} is the quantum yield of inter-system crossing in the photosensitiser, Φ_{TTA} is the quantum efficiency of the triplet-triplet annihilation process with the acceptor, and Φ_{F} is the quantum efficiency of the fluorescence from the excited singlet state of the acceptor to give the final upconverted emission.

The overall yield thus depends on the quantum yield of several processes, including efficient ISC in the triplet photosensitiser, efficient TTET between photosensitiser and annihilator, and efficient generation of the singlet excited state of the acceptor.

Spin-orbit coupling (SOC) is essential to the design of most triplet photosensitisers, and it is induced by the heavy atom effect.[23] Inter-system crossing is forbidden due to the spin selection rule, and requires a method of circumventing this issue. The electron in question is under a magnetic field due to the motion of the positively charged nucleus with respect to it, and this field is what causes mixing of singlet and triplet states of similar energy to each other. As this field is dependent on the nucleus, the strength of the SOC increases proportionally to the mass of the atom - therefore, SOC is best induced by the presence of heavy atoms and hence this property is known as the heavy atom effect.[23] Heavy transition metals such as iridium, ruthenium and platinum, as well as heavy halogens such as bromine and iodine, induce significant SOC. The heavy transition metals are most optimal for the purposes of triplet photosensitisers due to the range of structures possible when using them as building blocks, as well as their long lived triplet excited states.

1.2 The Structure of Triplet Photosensitisers

1.2.1 Increasing and Red-shifting Absorption in Triplet Photosensitisers

Increasing absorption in the visible and NIR regions has in recent years focused on the incorporation of organic chromophores into heavy transition metal centres, both as ancillary ligands coordinated directly to the metal centre, and as moieties which can be affixed to the ligands used in the complex.[22, 24-29]

Using these methodologies, the aim has been to create molecular systems in which absorption is strongest in the visible or IR region. This is in order to selectively target the absorption of low-energy photons to capitalise on the systems upconverting abilities. The Draper group[28] has previously built on the work of Borisov *et al.* in examining coumarin-6 as a possible ancillary ligand for Ir(III) complexes.[28] Borisov *et al.* found that a series of these complexes (Figure 1.4) exhibited strong absorption around λ = 472 nm (ε = 92,800 M^{-1} cm^{-1}), and phosphorescence at λ = 563 nm (Φ_P = 54%).[30]

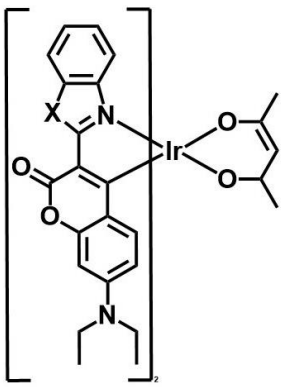

S1: X = N-Me
S2: X = O
S3: X = S

Figure 1.4*: Structures of complexes S1-S3.*[30]

In light of this, the Draper group recently carried out preliminary work to examine the use of coumarin-6 to increase the visible-region absorption of Ir(III)-based triplet photosensitisers. (Figure 1.5) These were found to have very promising properties, and as such are the starting point of much of the work in this thesis.[28]

Another focus is to append the ligands of the complex with organic chromophores in order to increase their base absorptivity, *via* an organic acetylene linkage. This also allows for the tactical addition of moieties which are known to have useful properties of their own - for example, pyrene exhibits strong absorptivity and has been well known for

decades to exhibit delayed fluorescence. [31] For this reason it is widely used in triplet photosensitisers,[25, 28] such as those shown in Figure 1.5.

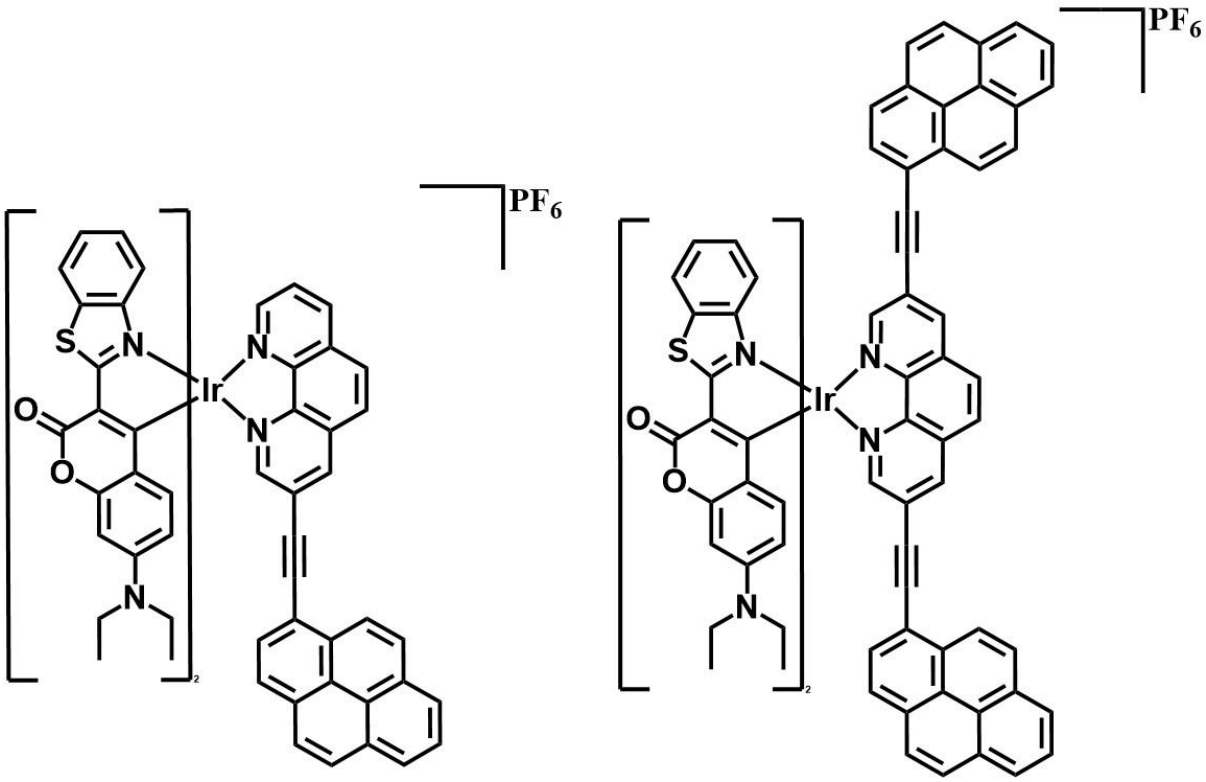

Figure 1.5*: Structures of Ir(III)-based triplet photosensitisers utilising coumarin-6 as ancillary ligands, previously prepared by the Draper group and featuring phen and pyrene as participating ligands.*[28]

1.2.2 The Choice of Acceptor

As the second part of the upconverting system, the choice of acceptor is as important as the triplet photosensitiser. However, due in part to its apparently simple function there has been far less focus on the development of a variety of acceptor molecules. 9,10-diphenylanthracene (DPA, **A1**) is generally the acceptor of choice as it has a high quantum yield and is readily available, but some research is now focusing on advancing the quantum yield of the final fluorescence of the acceptor. One such group, Gray *et al.*, has compared the yields of DPA with those of 9-(4-phenylethynyl)-10-phenylanthracene (PEPA, **A2**) and 9,10-bis(phenylethynyl)anthracene (BPEA, **A3**), shown in Figure 1.6. Their upconversion efficiencies are found to be 15.2 ± 2.8%, 15.9 ± 1.3%, and 1.6 + 0.8% respectively, of a maximum of 50% (due to the absorption of two photons and emission of one). [32]

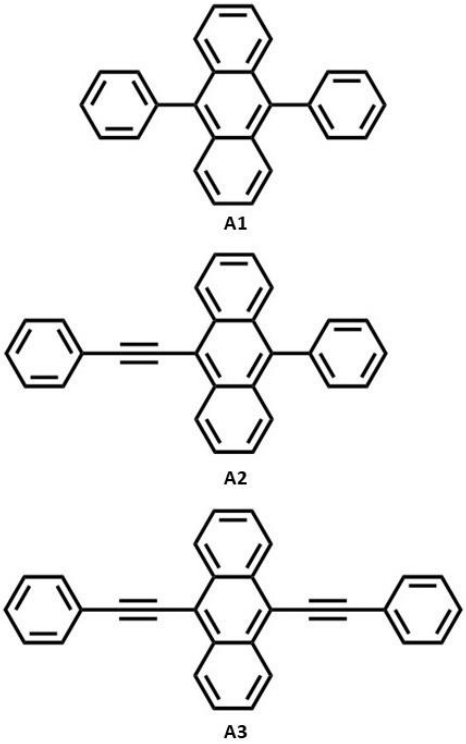

Figure 1.6*: The structures of DPA (**A1**), PEPA (**A2**) and BPEA (**A3**).*

As a result of this research, the highest efficiency of the PEPA acceptor is found to be only partly due to the minimal spectral overlap of the triplet photosensitiser, a zinc-porphyrin complex, and the acceptor. This is because the efficiency of DPA as an acceptor is minimally affected by its significantly larger spectral overlap, and so the spectral overlap appears not to be highly relevant in this case. The significantly lower efficiency of the BPEA, in spite of its comparable efficiency in processes such as TTET, was explained by the geometries of the excited triplet and singlet states, which do not overlap significantly, and so the energetic requirement of Equation 1.1 is statistically unlikely to be met.

These findings show the difficulty in designing acceptor molecules, coupled with the complexity of developing the triplet photosensitiser. For this reason, a reliable molecule such as DPA is commonly used as the first compound chosen for comparison of sensitisers, but also because modification of both molecules of the TTA-UC system presents a difficulty to accurately compare the effectiveness with systems currently in the literature. **A1**, **A3** and 1-chloro-9,10-bisphenylethynyl (**A4**, 1CBPEA) are all commonly used due to their high Φ_F and emission around 400 nm. However, many systems utilising platinum or palladium porphyrins will use perylene (**A5**), or rubrene (**A6**).[33-36]

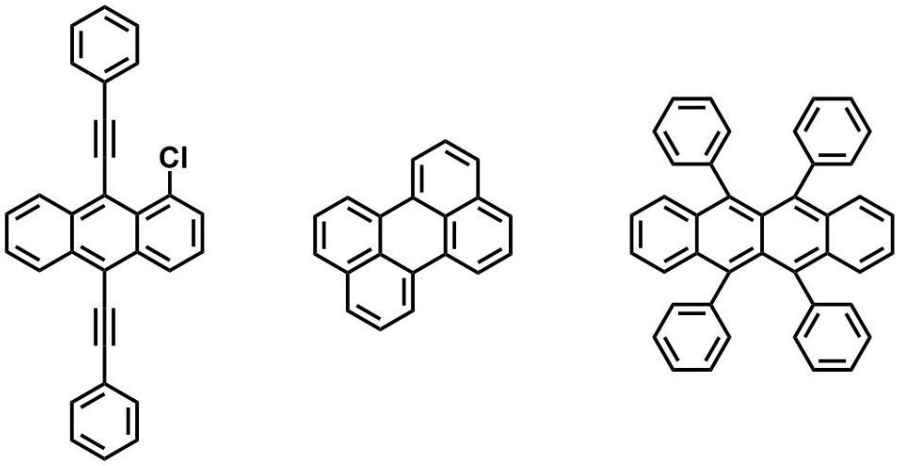

Figure 1.7*: The structure of 1CBPEA (**A4**), perylene (**A5**) and rubrene (**A6**).*

1.3 Triplet Photosensitiser Design

Triplet photosensitisers are chiefly designed with the aim of developing a long-lived, easily accessible triplet excited state. As such, the spin barrier of ISC must be overcome and the heavy atom effect is the most useful method available to reliably induce spin-orbit coupling.

Numerous heavy transition metals have been researched as potential triplet PS bases, particularly with a view to use in TTA-UC. Platinum and palladium have shown promise in the field,[22, 37-41] and both tend to absorb at longer wavelengths and are more suitable for biological or photovoltaic applications than those which require higher-energy input.

The first report of an upconversion emission *via* excitation by incoherent sunlight was reported in 2006 by Baluschev *et al.*, however the upconversion quantum yield was very low (~ 1%).[42] The group used PdOEP (Figure 1.8) as a triplet PS and DPA as the annihilator, with Islangulov *et al.* later managing to observe the same system achieve upconversion in a thin-film material.[43] These results illustrate that it is possible to carry out TTA-UC in ambient conditions, and even in the presence of oxygen, without complete quenching.

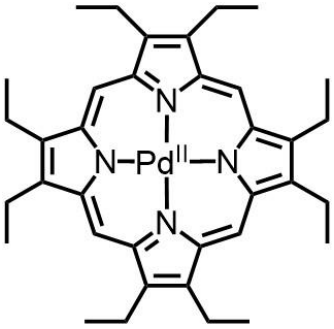

***Figure 1.8**: The structure of **PdOEP**.*[43]

Further Pd/Pt-porphyrin complexes have been extensively researched and found to have favourable photochemical properties, however a triplet PS with a particularly broad absorption band has been elusive. One further study by Baluschev *et al.* used a combination of two Pd-porphyrin PS molecules to increase the range of absorption by the overall system.[44]

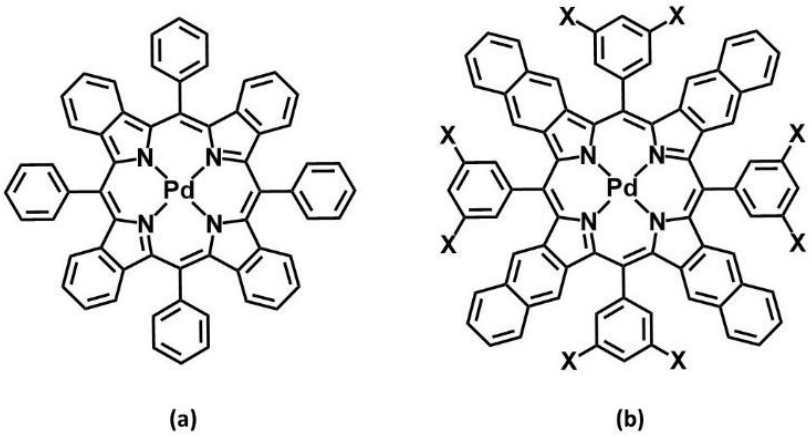

***Figure 1.9**: The two photosensitisers used by Baluschev et al.[44] (a) **PdPh$_4$TBP** and (b) **PdPh$_4$OMe$_8$TNP**.*

PdPh$_4$TBP (a) and **PdPh$_4$OMe$_8$TNP** (b) absorb at two different wavelengths (λ = 630 nm and λ = 700 nm respectively, Figure 1.10), while **A6**, used here as the acceptor molecule, absorbs in the region of 500 nm and does not overlap. A yellow upconverted fluorescence from **A6** was observed, which was notably more intense with the use of two light sources (λ_{ex} = 635 nm and 695 nm) for the two absorption bands than when using either source alone.

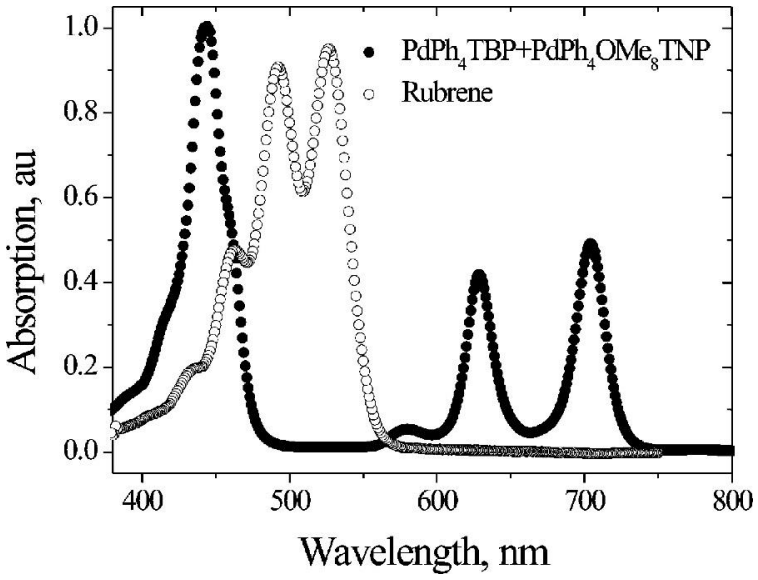

***Figure 1.10**: Absorption spectrum showing the Q-bands of **$PdPh_4TBP$** and **$PdPh_4OMe_8TNP$** at 630 nm and 700 nm respectively, and the Soret band of the porphyrin centres around 440 nm. The absorption of the acceptor, rubrene, is shown with pale dots.*[44]

While these porphyrin-based PS molecules can be difficult to modify chemically, their reliable properties provide a baseline from which to explore variations on the standard system of individual PS molecules in an UC system. In 2016, Xun *et al.* reported that a series of related Pd-porphyrin oligomers exhibited TTA-UC behaviour using DPA as the acceptor as expected. However, the absorption region of the oligomers had been broadened and their ability to harvest light had been enhanced in comparison to the analogous monomer complexes.[45] Also in 2016, Börjesson *et al.* published an exciting report of a Pd-porphyrin being embedded along with three anthracene derivatives in a liquid-crystal matrix, allowing directionally controlled TTA-UC.[46] The inability to control the direction of emission of the upconverted fluorescence in these systems is one of the drawbacks to use in an industrial setting, so directional control is a very promising development. Then in 2017, Fukuzaki *et al.* published a study of a TTA-UC system, again using a Pd-porphyrin PS and an anthracene-derivative acceptor, interacting with DNA.[47] The DNA was shown to be able to concentrate both the PS and acceptor molecules by proximal intercalation, resulting in a significantly increased upconverted fluorescence intensity.

Because of the difficulty in chemically altering the photophysical characteristics of porphyrin-based PS molecules, Pt(II)-bisacetylide complexes have been investigated.[48]

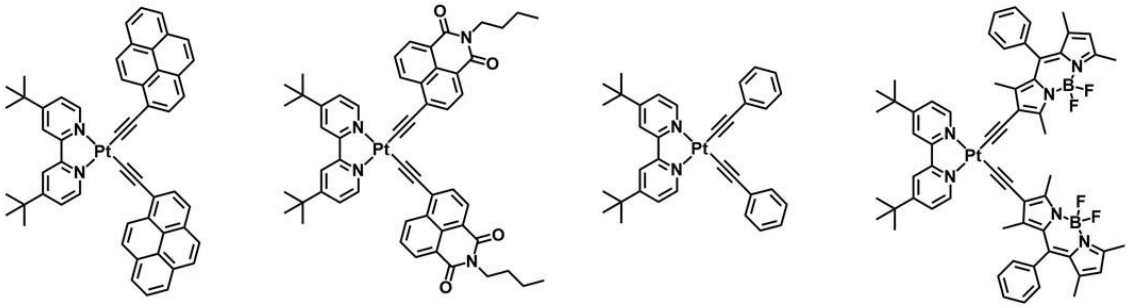

***Figure 1.11**: The structures of some platinum bisacetylide complexes, **Pt-1** – **Pt-4**.*[48]

In 2010, Guo *et al.* reported the novel platinum complex **Pt-2**, which was based on naphthalimide and compared it to the previously known **Pt-1**.[48] Both showed much stronger absorption than the model complex **Pt-3**, and both **Pt-1** and **Pt-2** exhibit long-lived ^{3}IL states, of 73.7 μs and 118 μs respectively. In turn these complexes respectively gave high Φ_{UC} values of 28.8% and 39.9%, and the group followed this with numerous N^N Pt(II) acetylide PS molecules wherein the chromophores were modified to alter the photochemical properties of the complexes.[49, 50]

1.4 Optimising the Photophysical Properties of Photosensitisers

While many metal centres have been investigated for applications as photosensitisers, only a few have exhibited optimal properties and quantum yields. Ligands can also have an effect on the energy levels of a complex due to their position in the spectrochemical series.[51]

There are three main transitions which occur in d^6 polyimine molecules. A metal-centred (MC) transition is a d-d electronic transfer. A metal-to-ligand charge transfer (MLCT) involves the transfer of charge from predominately metal-character orbitals to predominantly ligand-character orbitals, while intraligand (IL) transitions are π-π* in character. IL states are also referred to as ligand-centred (LC) states throughout the literature. As Kasha's rule states that, only the lowest-lying excited state will contribute significantly to the photophysical properties of a complex, it is this state that is generally discussed for emission-based properties.

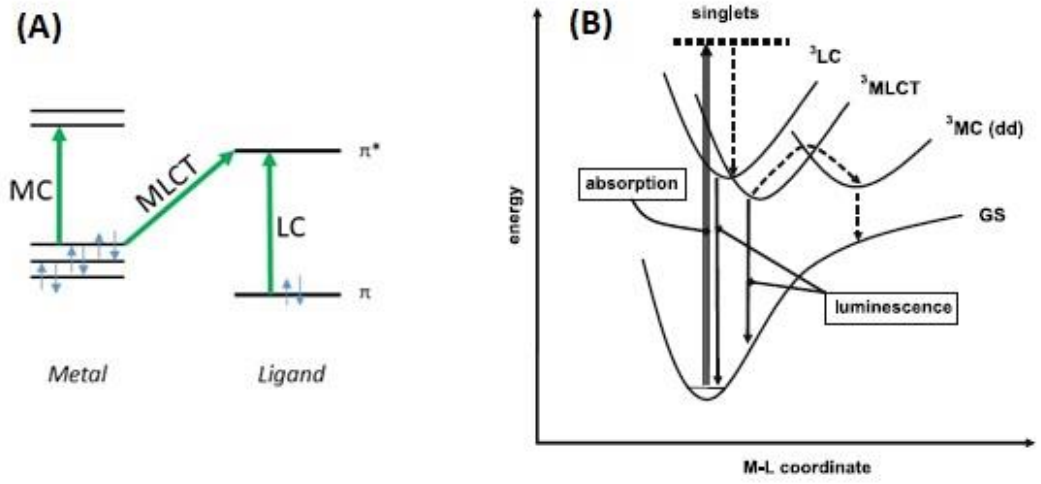

***Figure 1.12**: (A) A simple orbital diagram of MC, MLCT and LC transitions in a metal complex. (B) Electronic transitions involving MC, MLCT and LC excited states for a polyimine complex of a d^6 metal centre.*[52]

In the event that a MC transition is the lowest excited state, it may relax non-radiatively to the ground state, especially if there is near-overlap of the wavefunctions of the MC state and the ground state. In that case, the relaxation will be ultrafast and there will be no ISC. Fe(II)-polyimine complexes possess a small Δ_{oct}, resulting in a MC transition as the lowest-lying excited state and rendering Fe(II) unsuitable as a triplet photosensitiser. Conversely, in Os(II) and Ir(III) complexes the MC states are so high in energy due to large Δ_{oct} values that they are essentially irrelevant to the photophysical properties of the complex.

Both MLCT and IL states relax radiatively, and this luminescence can be long-lived. Many complexes have lifetimes in the range of microseconds or even longer. As the involvement of heavy metals results in a higher ISC rate constant, ^{3}MLCT states have significantly shorter lifetimes than those of ^{3}ILC states. Due to the energy gap law, if the lowest-lying state is ^{3}MLCT and there is a small energy gap between it and the ground state, the rate of non-radiative relaxation may dominate and no luminescence will be seen.[52] Ru(II) and Ir(III) usually feature ^{3}MLCT and ^{3}IL states which are well positioned for triplet PS complexes, and as they are readily modifiable. Previous studies have found that the TTA-UC process is more efficient in an intermolecular system, than in an intramolecular system.[53] However, in recent years the increased focus on the TTA-UC

has led to the development of systems which exhibit strong upconversion in rigid intramolecular systems,[54] as well as in water,[55] and in air.[56]

1.4.1 Design and Photophysical Properties of Ir(III) and Ru(II) complexes

Both ruthenium and iridium have been extensively studied as triplet photosensitisers.[22, 25-29, 38, 39, 57-60] Ruthenium typically forms complexes with a +2 oxidation state while iridium commonly forms +3 states. Ruthenium coordinates readily to N^N ligands such as 2,2'-bipyridine (bpy), while iridium ions generally coordinate to N^N, C^N or O^O ligands, such as 2-phenylpyridine (ppy) or acetylacetonate (acac). Iridium complexes are generally cationic or neutral, while ruthenium complexes are generally cationic.

The synthesis of complexes of either metal are similar. The metal salt, either $[RuCl_3]\cdot xH_2O$ or $[IrCl_3]\cdot xH_2O$, is reacted with two equivalents of the ligand generally utilised as the non-participating ligand in the final complex, *e.g.* bpy or ppy. This forms $[Ru(bpy)_2]Cl_2$, or a chlorine-bridged dimer of iridium, $[Ir(ppy)_2(\mu\text{-}Cl)]_2$, which can then be coordinated with a wide range of N^N ligands to form the typical octahedral complexes used as triplet PSs. (Figure 1.13)

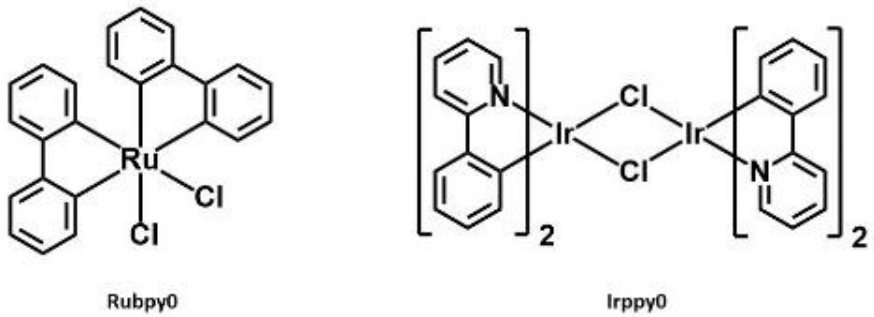

***Figure 1.13**: The precursors commonly used in the synthesis of Ru- and Ir-based PS molecules, $[Ru(bpy)_2]Cl_2$[61] (**Rubpy0**) and $[Ir(ppy)_2(\mu\text{-}Cl)]_2$ (**Irppy0**) respectively.*

The useful photophysical characteristics of Ru(II) and Ir(III) complexes include easy excitation to the singlet excited state followed by relatively facile ISC to the triplet excited state. The excited triplet state may relax radiatively, *i.e.* phosphorescence, The excited triplet state, due to the disallowed nature of both ISC and phosphorescence, tends to have a significantly longer lifetime than that of the singlet state, allowing other photophysical processes to occur. This is especially true in more recently published,

selectively-designed complexes utilising novel chromophores. It is the exaggeration of this characteristic which is ultimately the most significant in determining if a complex is a "good" PS. As explained, there are three main transitions which these complexes undergo. MC states are inaccessible for iridium molecules due to the debilitating high Δ_{oct} value[51], whereas they are accessible in some cases in ruthenium molecules. In these Ru complexes relaxation of the MC state, *via* a $^1\sigma_M$ to π_M transition, deactivates the long-lived triplet excited states which are sought for photosensitisation.[62] Otherwise, emission from Ru(II)-polyimine complexes is generally assigned to the ^{3}MLCT state (π_M to $^1\pi_L$) and iridium complexes often emit from a metal-ligand-to-ligand charge transfer state (^{3}MLLCT), a form of MLCT. Both also form ^{3}LC states *via* π_L to $^1\pi_L$ transitions.

The absorption of Ir(III) and Ru(II) complexes in the visible and IR regions is generally not very strong, and so much of the literature deals with attempting to improve this. Some basic complexes have already been used as part of organic light-emitting diodes (OLEDs).[63-65] These do not possess the intense absorption that is required when developing a PS molecule for TTA-UC. Chromophores are added to the metal centres in order to increase the molar absorptivity in the visible regions. For example, the use of coumarin-6 in iridium complexes results in a marked increase in the absorption of those complexes in the visible region, and thus increases the chances of successfully applying them in TTA-UC.

1.5 Organic Triplet Photosensitisers

The obvious limitations to using heavy transition metals is their cost, rarity, and frequent toxicity. Generally, below the first row d-block metals the elements are so rare that they are simply not commercially viable aside from use as catalytic products. As a result, purely organic photosensitisers are an area of focus. These incorporate no heavy metal centres, however they lose out on the orbital mixing which results from the heavy atom effect of the metal centre.

One of the first purely organic triplet photosensitisers used for upconversion was developed in 2009, by Sun *et al.*, **O1** (Figure 1.14) showed long-lived triplet excited states (τ_T = 25 μs), and a strong absorption in the visible region (λ_{abs} = 536 nm, ε = 91,200 M^{-1} cm^{-1}).[66] Sun used DPA as the acceptor in an upconversion system with this sensitiser, and observed a blue emission of upconverted light, with an upconversion quantum yield

of Φ_{UC} = 0.06%. This appeared white to the eye due to the much stronger green fluorescence of the complex with a yield of Φ_F = 13%.

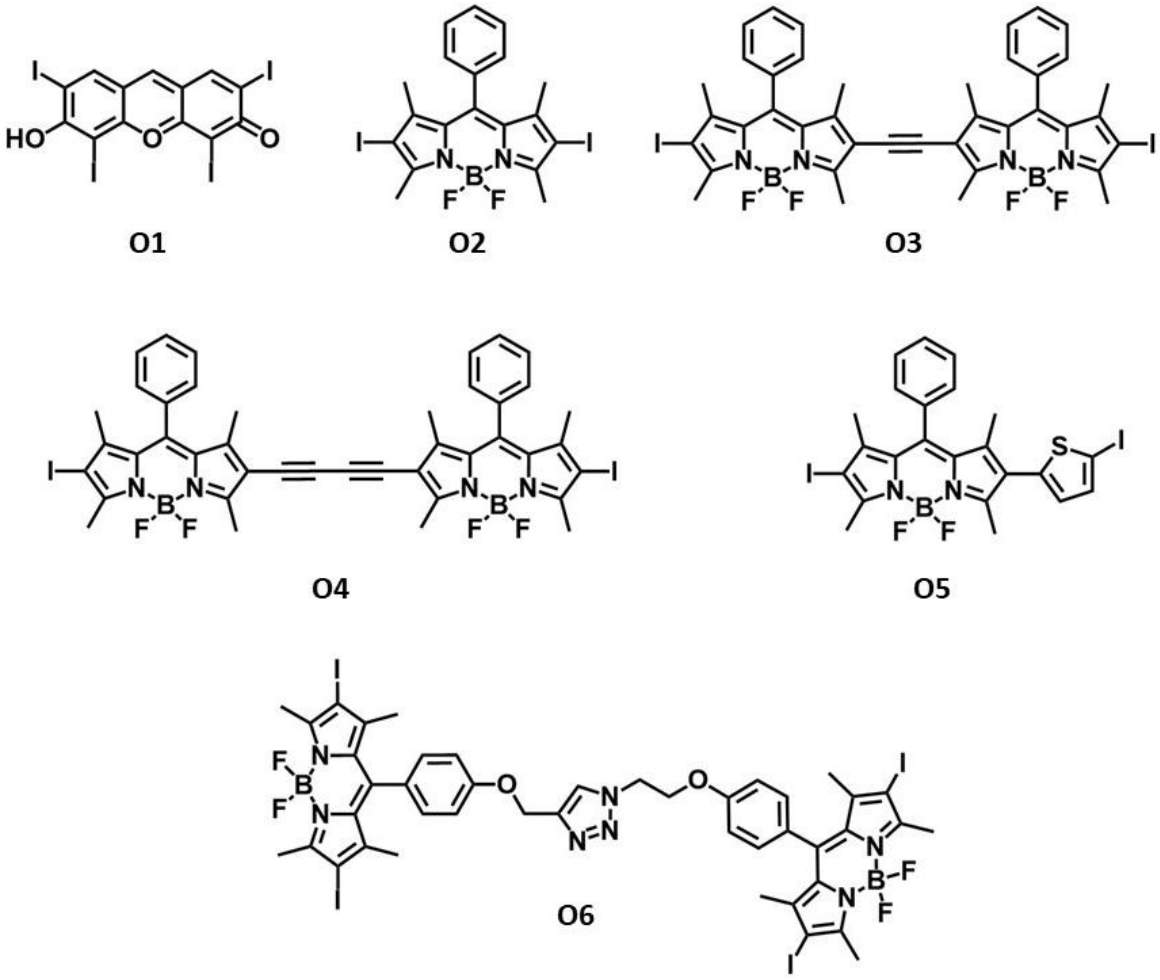

***Figure 1.14**: The structure of the organic triplet photosensitisers **O1** to **O6**.*

Related organic photosensitisers include a series of boron-dipyrromethene- (BODIPY) based compounds synthesised by Zhao *et al.* which utilise iodine atoms for their heavy atom needs. These molecules exhibit strong absorption in the region of 575-615 nm with strong absorption coefficients of up to 180,000 M^{-1} cm^{-1}. When perylene is used as the acceptor molecule in a TTA-UC system, an upconversion quantum yield of 5.4% is observed.[24] This is then increased to 16.5% when thiophene is incorporated into the structure (**O5**) of the PS molecule.[67]

There have also been reports of organic upconverting systems without the use of heavy atoms.[68] These have shown significantly lower upconversion quantum yields, but have proven that the process is possible even in the absence of the heavy atom effect. Castellano *et al.* reported a simple organic system using **O8** as the PS and **A7** as the

acceptor (Figure 1.15) in 2009.[69] Visible-to-UV upconversion was observed and an upconversion quantum yield of 0.0058% was found.

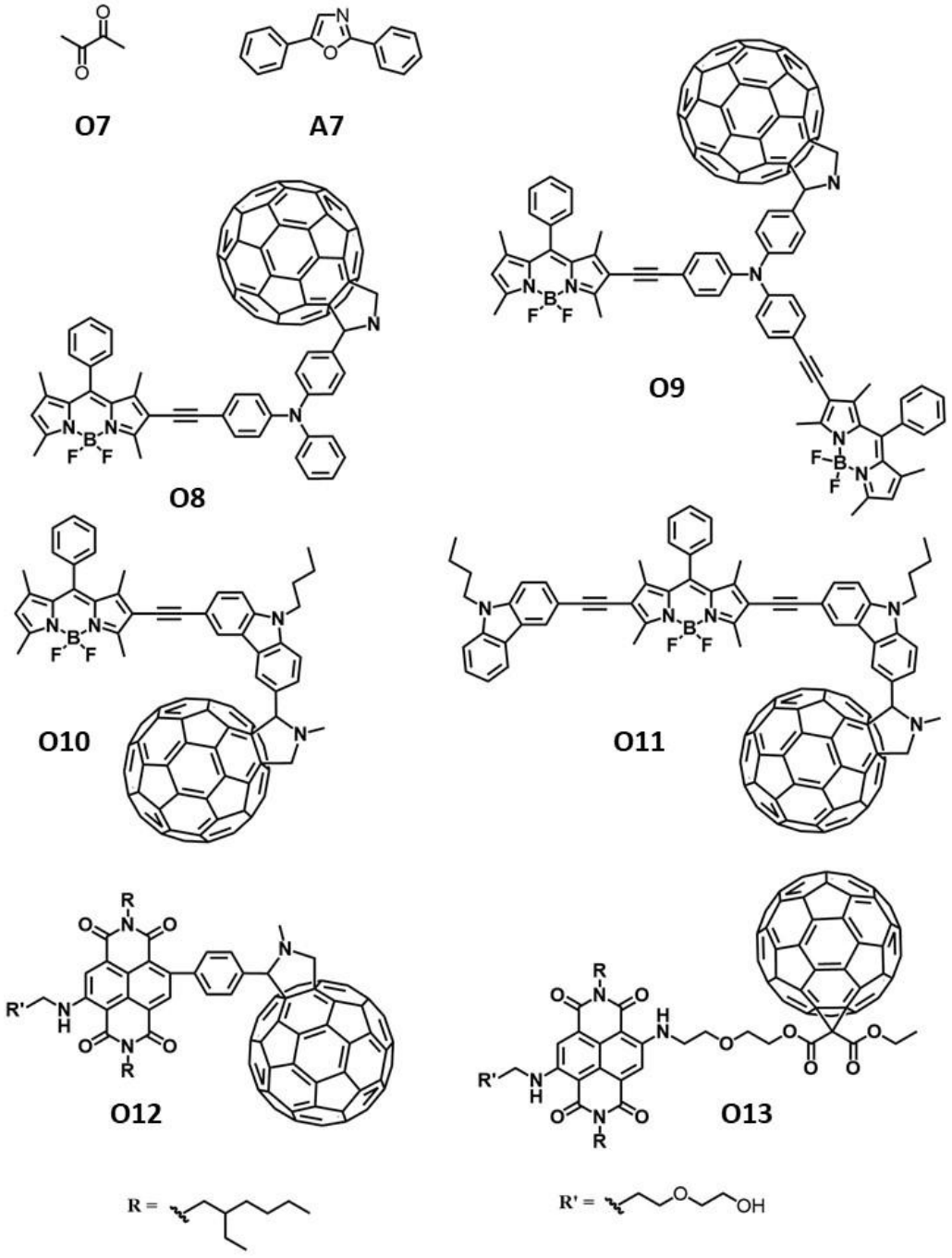

***Figure 1.15**: The structures of organic triplet photosensitisers **O-7** to **O-13**, and acceptor **A-7**.*

Many organic photosensitisers utilising fullerene (C_{60}) have also been explored as C_{60} exhibits an ISC efficiency near unity, meaning that it may be able to overcome the lack of

a heavy atom effect. Zhao *et al.* published a number of C_{60}-based compounds which were investigated for TTA-UC, with perylene again used as the acceptor.[70-72] **O8** and **O9** both show strong visible range absorption and extended triplet state lifetimes (for O-9, these were ε = 118,800 M^{-1} cm^{-1} at 539 nm, and τ_T = 32.3 μs). Their upconversion quantum yields were Φ_{uc} = 0.36% for **O9** and 0.18% for **O10**.[73] **O11** and **O12** each exhibit strong absorption in the visible region as well, within 540-600 nm, and they show stronger upconversion with values of Φ_{UC} = 2.3% for **O11** and Φ_{UC} = 2.9% for **O12**.[70] **O13** and **O14** are napthalenediimide (NDI) based compounds and also showed strong visible range absorption and triplet excited state lifetimes of 37.2 μs and 90.1 μs respectively. However, even though C_{60} has a value of Φ_{uc} = 0.8% on its own, **O13** and **O14** show lower upconversion quantum yield values – 0.46% and 0.33% respectively. These are among the most advanced organic photosensitisers for TTA-UC, however there is still significant room for improvement before purely organic compounds can replace the heavy metal-based complexes which are currently the most viable for commercial use.

1.6 Photodynamic Therapy

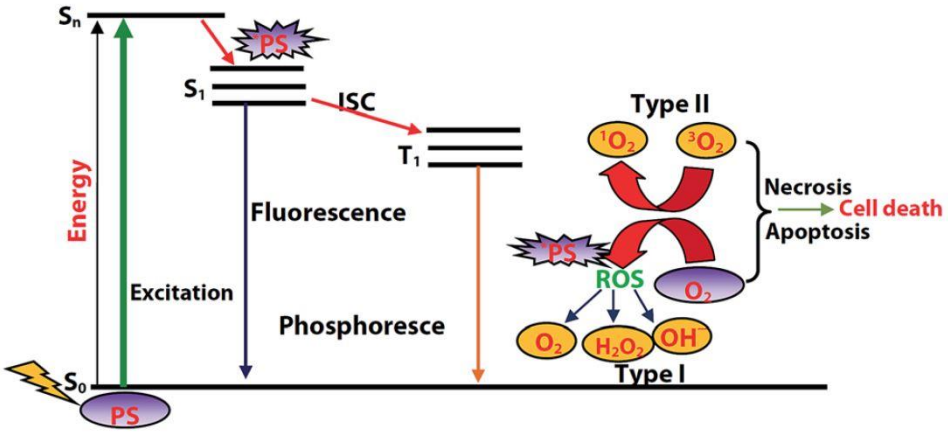

***Figure 1.16**: The Jablonski diagram of the process of singlet oxygen sensitisation for photodynamic therapy.*[74]

Photodynamic therapy (PDT) is the use of non-toxic TTA upconverting systems to produce singlet oxygen within a cancerous or harmful tissue, causing oxidative cell death.[75-77] Any versatile and targeted form of cancer treatment is treated with great excitement and PDT has been researched for over a century, since Tapennier used eosin to topically treat melanoma.[78] PDT has many benefits, however one major practical drawback is the penetration of light through the cellular material of the body, which limits its application in real-world medical use.

The excitation of the PS leads to cell death and damage *via* two distinct pathways. The type-I pathway involves direct proton or electron transfer from the PS complex to a bioorganic molecule in the cell, yielding a radical species which in turn reacts with present oxygen to form a reactive oxygen species (ROS). These carry out oxidative damage to the cells and can include the superoxide anion, $O_2^{\cdot -}$. The type-II pathway involves the excited PS molecule directly interacting with triplet oxygen present to form reactive singlet oxygen, which again goes on to oxidatively damage the surrounding cells.[74] The generation of these species is laid out in Figure 1.16.

The main benefit of PDT is that it is selective. If the PS used does not cause cell death in the absence of a light source (dark cytotoxicity), then only cells which contain the PS molecule and are subject to the light source used will be affected. The lifetime of a singlet oxygen molecule in a cell is around 3μs resulting in a diffusion range of just around 130nm, which is the cause of this selectivity.[79] However, the major drawback to PDT and other photo-initiated therapies is the low depth of penetration of the light source.[80] As a result of this, PDT has become viable for a more limited number of conditions than hoped, including skin and oesophageal cancers as these generally form at or near the surface of tissues.

As a result of this, an increasing area of research is that of sonodynamic therapy (SDT).[81-83] This uses species known as sonosensitisers (SS) with long-lived excited states to generate reactive species similar to PDT, however in this case the source of excitation is ultrasound (US) which causes cavitation and extremely high pressure and temperature in very localised areas. While SDT is subject to the metal ion used just as PDT is, US is able to penetrate tissues at any depth and overcome the "depth-penetration barrier" which PDT faces. Despite this, various biological processes seem to interfere with the sonoexcitation process. As such, generation of reactive species is weaker in SDT than in PDT and more investigation is needed.[80, 84, 85]

1.7 1,10-Phenanthroline as a Synthetic Base

1.7.1 Synthesis

Each of the products featured in this thesis (**Ir-1** to **Ir-6, Figures 1.18 and 1.19**) includes a functionalised 1,10-phenanhroline (phen) moiety which must first be synthesised by

selective bromination of the unmodified phen. Phen is popular in the literature as a synthetic chemical starting material and has been for decades, due to its planar geometry, low natural fluorescence, and bidentate chelating ability. It has a fluorescence lifetime of just $\tau < 1$ ns in cyclohexane at room temperature (RT), along with an emission around 360 nm and a negligible quantum yield ($\Phi_f \leq 0.01$).[86-88] Due to the presence of two nitrogen atoms within the π-conjugated framework, as with 2,2'-bipyridine (bpy) the system is electron deficient and can stabilise some metals complexes with a π-backbonding relationship. These properties have led to the use of phen across a range of applications, nearly always as a core building block.[87, 89-91]

1.7.2 Targeted Substitution of 1,10-Phenanthroline

Selective substitution of phen can be achieved by bromination under specific conditions. The position of bromination can be varied by changing the solvent, temperature, catalytic base, more typically, a combination of the various factors. These brominations occur in the 2,9-, 3,8-, 4,7- and 5,6- positions,[25, 27, 28, 92] with symmetric dibromination being far more straightforward than asymmetric monobromination of the 2-, 3-, 4-, or 5-positions. Substitution at each position results in variations in the standard photophysical properties of the phen. These changes can in turn be designed to more appropriately fit the role of a triplet photosensitiser ligand.

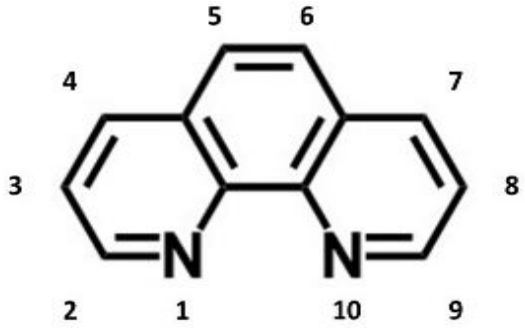

Figure 1.17*: The numbered positions of 1,10-phenanthroline.*

Once brominated, the system can undergo a targeted cross-coupling reaction such as a Sonogashira or Suzuki reaction. In spite of this, the couplings are successfully carried out across multiple positions on a phen ligand concurrently with minimal under-coupling, *i.e.* on a 3,8-dibromo-1,10-phenanthroline ligand, both positions can be coupled in the same reaction without formation of the mono-coupled product, simply by increasing the

catalyst and reaction time. These Sonogashira reactions are carried out on-the-complex, *i.e.* where the phen ligand is coordinated to a metal centre before the cross-coupling reaction. This is to reduce the instance of the copper co-catalyst coordinating to the nitrogen atoms of the phen, preventing the necessary co-catalyst cycle.

One particular modification which is used in this thesis is the insertion of acetylene linkages between the phen and its substituent moieties. This provides an increased distance between the chromophores, as well as a greater ability to tailor the planarity and size of the aromatic ligand.

As found by Tor *et al.* in their works, the addition of these acetylene linkages has a dramatic effect on the photophysical properties of the molecule.[93-95] They allow the transfer of energy or electrons in transitions between the phen and its substituents, the delocalisation of electronic states across them, and thus a red-shift of the emission wavelengths.

1.8 Aims of the Project

The aims of the project are to synthesise Ir(III)-based triplet photosensitisers utilising coumarin-6 (C6) and 2-phenylpyridine (ppy) as ancillary ligands. In Chapter 2, the novel complexes comprising the C6 ligands will follow on from complexes previously published by Lu *et al.* in order to compare the effect of varying the position and number of the 1-ethynylpyrene (EP) moieties.[28] One complex (**Ir4**) comprising ppy ancillary ligands will also be included in this chapter for the purposes of comparison to its C6 analogue. The target complexes are shown in Figure 1.18.

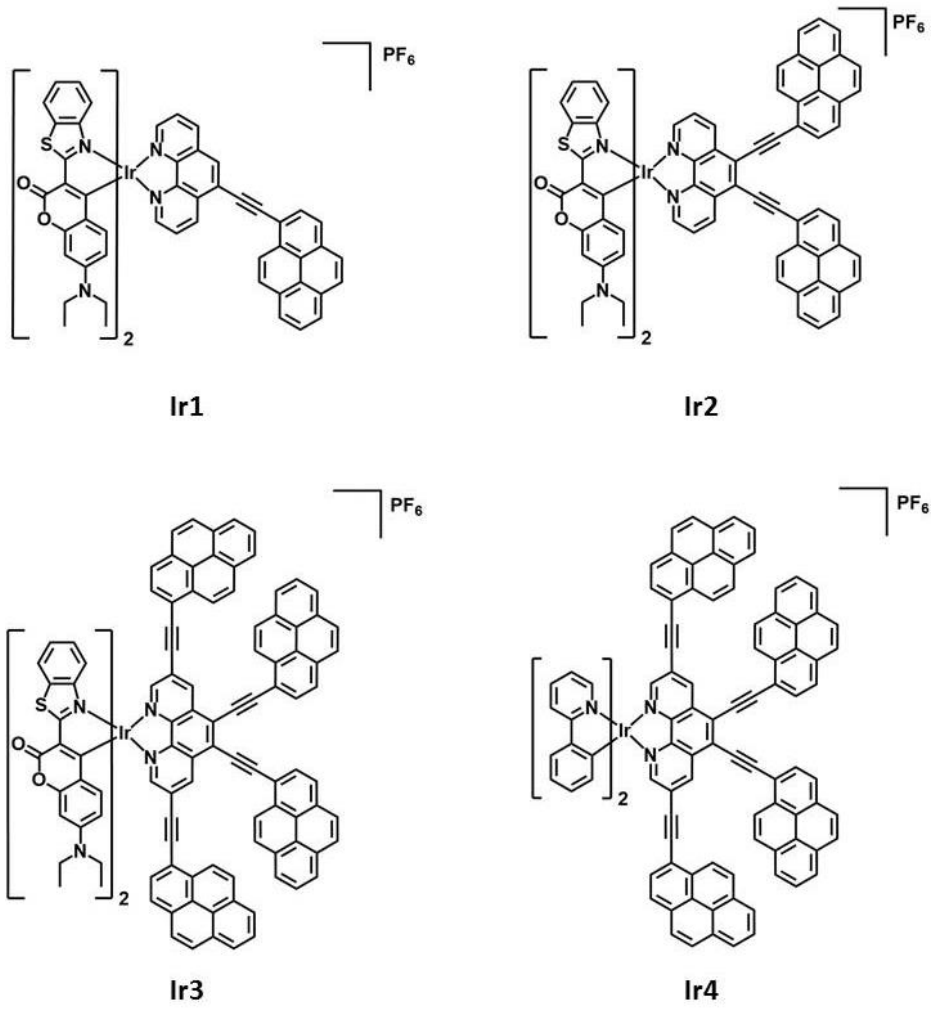

Figure 1.18*: The target Ir(III) complexes of Chapter 2.*

In Chapter 3, two novel dinuclear Ir(III) complexes will be presented. Their photophysical properties and computational calculations will be explored and compared to their previously published mononuclear analogues. These complexes are displayed in Figure 1.19.

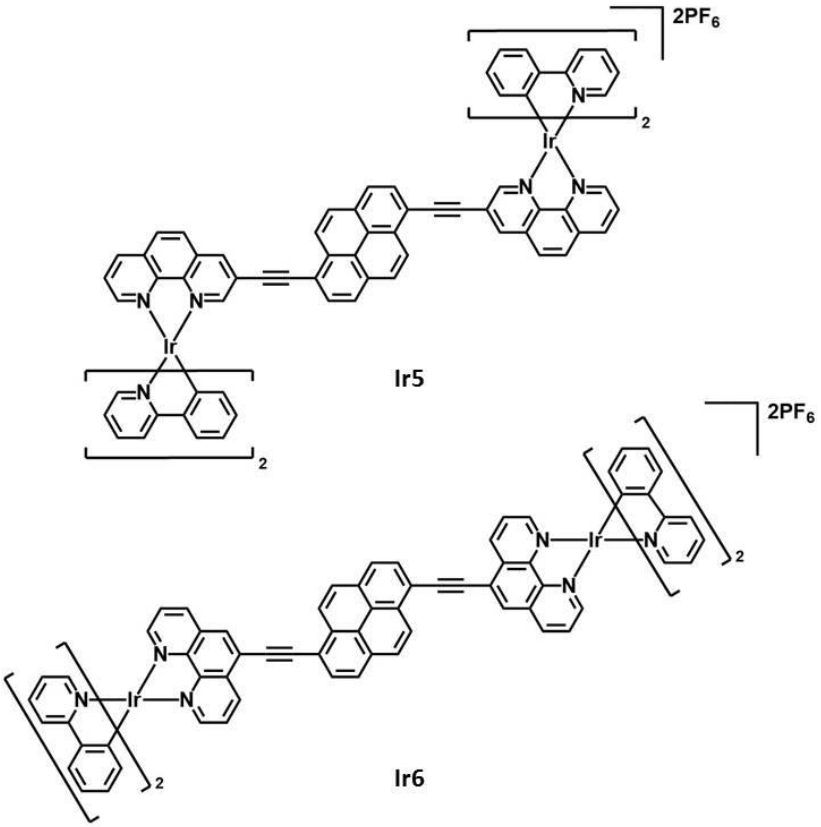

Figure 1.19*: The target dinuclear Ir(III) complexes of Chapter 3.*

The synthesis and structural characterisation of each complex will also be explored. The intended end-use of these triplet photosensitising molecules is as part of a TTA upconversion system, as discussed earlier, and it is for this purpose that the photophysical properties of each will be explored. It is hoped that these results will indicate which complexes are of greatest interest for further study.

Time dependent density functional theory (TDDFT) calculations were carried out in Dalian Institute of Technology in order to theoretically determine the orbital energy levels, the energy and character of excitations, and those of triplet excited states in particular. These calculations are referred to as time-dependent as they adapt theoretical techniques for ground-state calculations to deal with time-dependent activities. These calculations can then be compared to experimental results in order to confirm the theoretical conclusions drawn from those results.

The quantum yield of TTA-UC will be measured by the intensity of emission of DPA in the presence of a selected triplet photosensitiser when excited at 473 nm, and calculated

according to Equation 1.2. The photophysical results will be evaluated with regard to the structure of each complex in order to come to conclusions about future triplet PS design.

Chapter 2

Synthesis of Complexes

2.1 Synthesis of Ir1 – Ir4

2.1.1 Bromination of 1,10-Phenanthroline

A similar synthetic route was used to generate each of the complexes described in this chapter, with the exception of the selective bromination of 1,10-phenanthroline (phen, **L0**). Each of the bromination reactions is detailed in Scheme 2.1. For 5-bromo-1,10-phenanthroline (**L1**), a modified version of a previously published preparation was used.[96] Fuming sulphuric acid (30 %) was used as the solvent, with roughly 0.5 equivalents of bromine in order to prevent formation of side products. The reaction was carried out at high pressure, by using a pressure tube sealed with Teflon tape as the reaction vessel, and high temperature (135 °C), yielding the product after purification by column chromatography at 12 %.

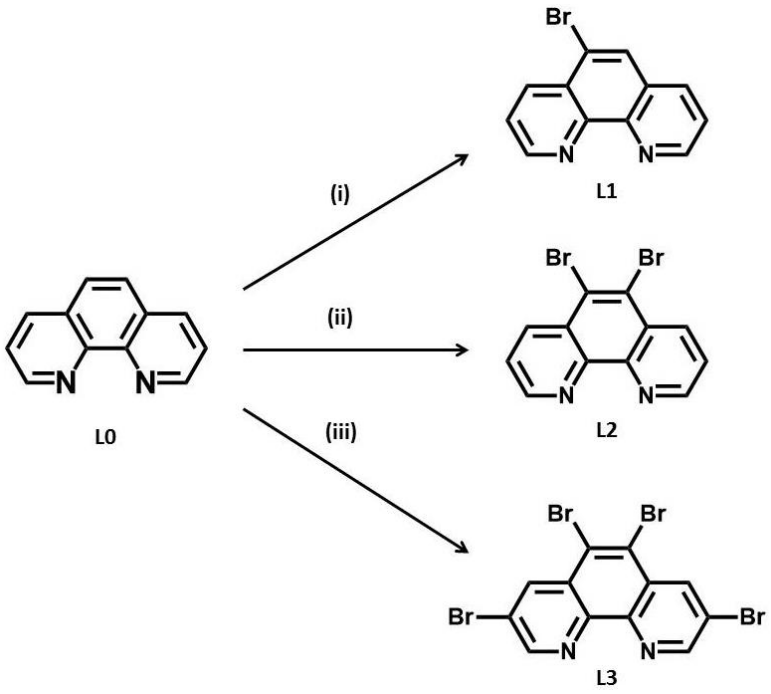

***Scheme 2.1**: The synthesis of 5-bromo-1,10-phenanthroline (**L1**), 5,6-dibromo-1,10-phenanthroline (**L2**) and 3,5,6,8-tetrabromo-1,10-phenanthroline (**L3**). (i) $H_2SO_4.SO_3$ (30 %), Br_2, 135°C, high pressure, 23 hrs, yield: 12 %; (ii) $H_2SO_4.SO_3$ (30 %), Br_2, 150°C, 72 hrs, yield: 6 %; (iii) $SOCl_2$, Br_2, 85°C, 44 hrs, yield: 38 %.*

The 5,6-dibromo-1,10-phenanthroline (**L2**) proved very difficult to synthesise, despite several published methods.[97] To a solution of phen in fuming sulphuric acid (30%), three equivalents of bromine were added dropwise, before being heated to 150 °C for 72 hours. The reaction was attempted three times with longer reaction times in order to obtain a higher yield, however the yield remained at 6%.

The generation of 3,5,6,8-tetrabromo-1,10-phenanthroline (**L3**) was prepared by a modified published method[98], but required the use of thionyl chloride ($SOCl_2$) as the reaction solvent. Excess bromine was added dropwise over an hour to the solution of phen in $SOCl_2$ as the solution was heated to 85 °C. After 44 hours at reflux, the solution was cooled and filtered using a dry fritted glass funnel. Taking extreme care, as $SOCl_2$ reacts violently with water, a 2 M aqueous solution of ammonia was washed through the solid slowly until the filtrate was clear. The resulting pink solid was purified by recrystallisation from toluene (using a small amount of $CHCl_3$ to initially solubilise the product), yielding the pure product (38 %).

2.1.2 Synthesis and Coordination of Coumarin-6- and 1-Phenylpyridine-based μ-Ir(III) Dimers

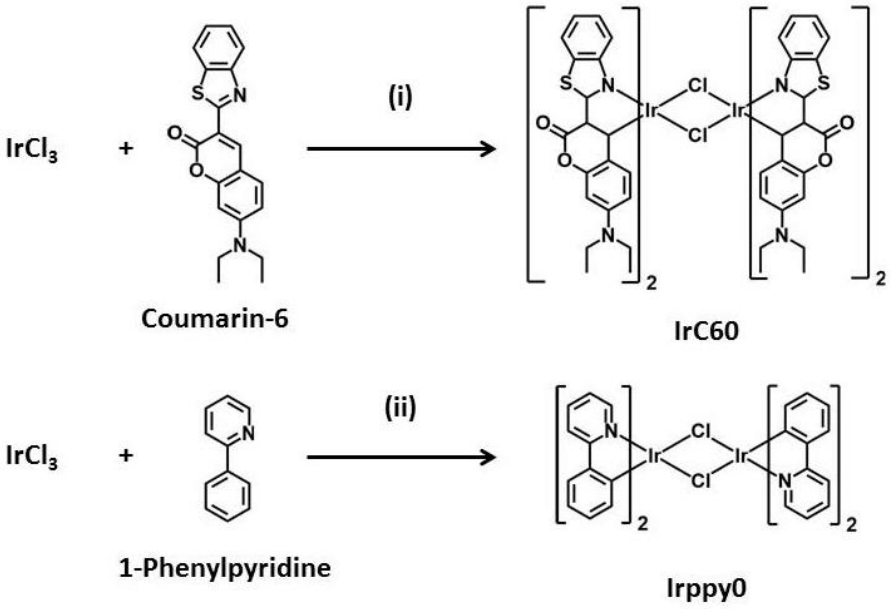

***Scheme 2.2**: Synthetic schemes of **IrC60** and **Irppy0**. (i) H_2O:2-ethoxyethanol (1:3, v/v), 130°C, 48 hrs, yield: 61%; (ii) H_2O:2-ethoxyethanol (1:3, v/v), 130°C, 24 hrs, yield: 83%.*

Each purified brominated phen compound was used as a ligand for coordination to a pre-prepared μ-Ir(III) dimer. This generated brominated metal complexes for use as the necessary starting materials for the Sonogashira cross-coupling reactions to generate the respective final compounds. Each μ-Ir(III) dimer was synthesised (Scheme 2.2) from $IrCl_3 \cdot H_2O$, with either coumarin-6 (C6, to form **IrC60**) or 2-phenylpyridine (ppy, to form **Irppy0**) as the auxiliary ligands.

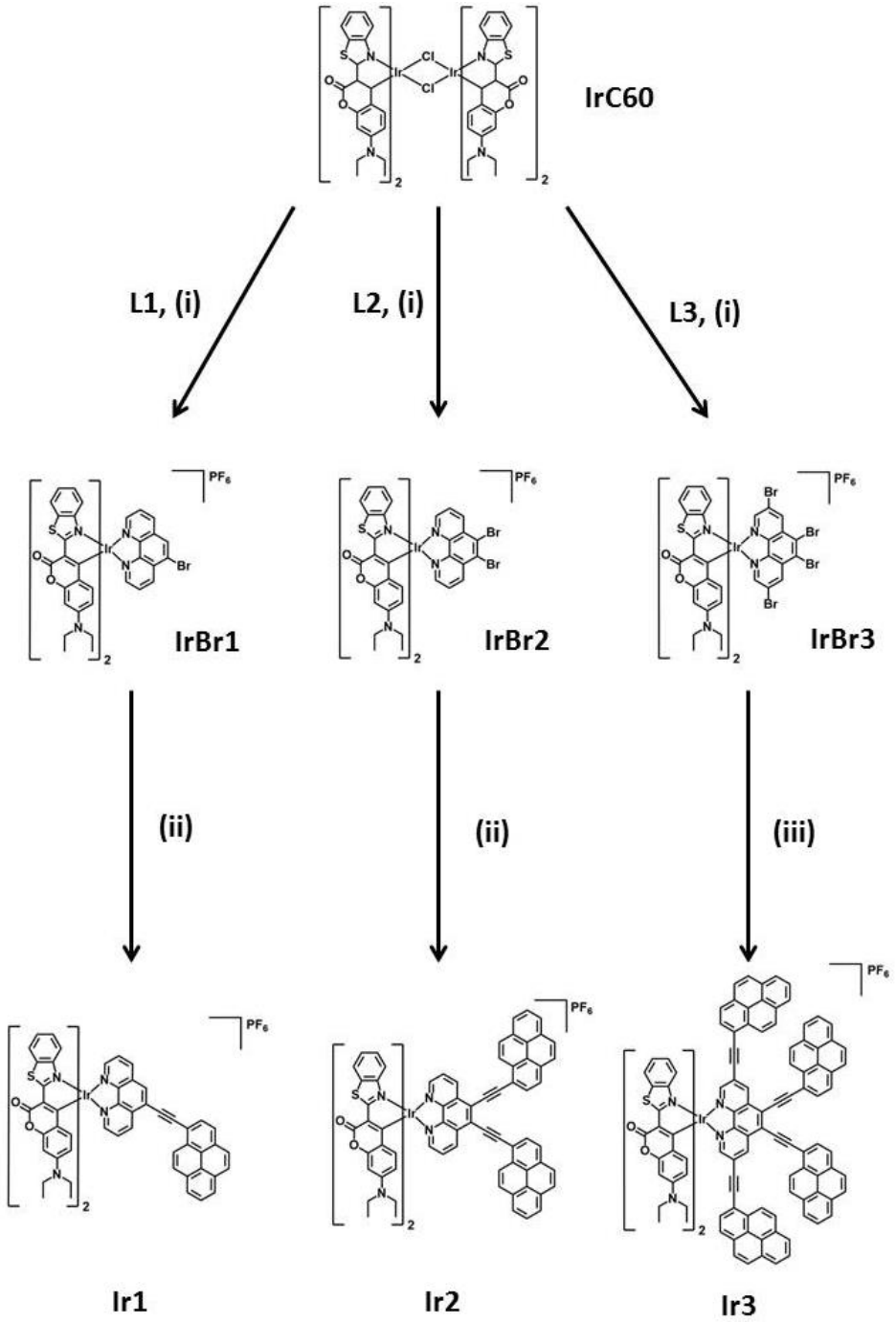

***Scheme 2.3**: The synthetic routes leading to **Ir1**, **Ir2** and **Ir3**. (i) CH_2Cl_2:MeOH (40:1, v/v), 50°C, 4 hrs, yield: **IrBr1** (69 %), **IrBr2** (86 %), **IrBr3** (83 %); (ii) 1-ethynylpyrene, $Pd(PPh_3)_2Cl_2$, PPh_3, CuI, MeCN:Et_3N (5:2, v/v), 80°C, 24 hrs, yield: **Ir1** (29 %), **Ir2** (21 %); (iii) 1-ethynylpyrene, $Pd(PPh_3)_2Cl_2$, PPh_3, CuI, MeCN:Et_3N (5:2, v/v), 80°C, 48 hrs, yield: < 1 %*

Each reaction was carried out in a mixed solvent system of H_2O:2-ethoxyethanol (1:3, v/v) with a slight excess of the ligand in order to avoid wasting the precious iridium. The resulting mixture was filtered directly, and washed with EtOH/diethyl ether. A simple purification process was achieved for both using a small silica plug, with a CH_2Cl_2 mobile phase.

The coordination of the brominated phen ligands to the Ir(III) centres was carried out in refluxing CH_2Cl_2, with several drops of MeOH added to increase solubility.[28] Upon cooling, a saturated solution of KPF_6 in MeOH was added to precipitate the product. The product was redissolved in CH_2Cl_2, and precipitated again using hexanes and then filtered. In some cases, the resulting solid was purified by column chromatography (CH_2Cl_2:MeOH, 100:1, v/v).

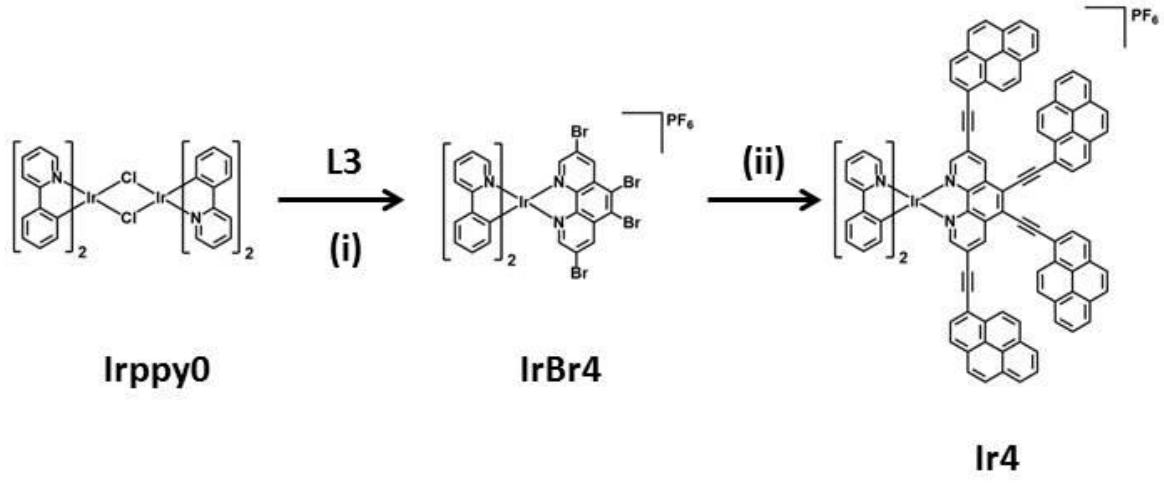

***Scheme 2.4**: The synthetic routes leading to **Ir4**. (i) CH_2Cl_2:MeOH (40:1, v/v), 50°C, 4 hrs, yield: 88 %; (ii) 1-ethynylpyrene, $Pd(PPh_3)_2Cl_2$, PPh_3, CuI, MeCN:Et_3N (5:2, v/v), 80°C, 48 hrs, yield: 41 %*

2.1.3 Sonogashira Cross-Coupling Reactions of IrBr1 – IrBr4 with 1-Ethynylpyrene

Each of the Sonogashira cross-coupling reactions to produce **Ir1** – **Ir4** was carried out in a mixed solvent system of dry Et_3N:CH_3CN (2:5, v/v), which was thoroughly degassed with N_2 before reaction, with the commercially available EP. For each brominated position to be coupled, three equivalents of EP were used. With the starting compounds **IrBr1**, **IrBr2** (Scheme 2.3) and **IrBr4** (Scheme 2.4), the reactions were successful and the resulting solutions were purified first by column chromatography (CH_2Cl_2:EtOAc, 100:5, v/v), and then further purified by preparative thin layer chromatography, using the same mobile phase. However, with the starting compounds of **IrBr1** and **IrBr2**, which utilise C6 as the ancillary ligands, the heat sensitivity of the C6 ligand appeared to generate numerous decomposition impurities, greatly affecting both purification of the product, and product yield.

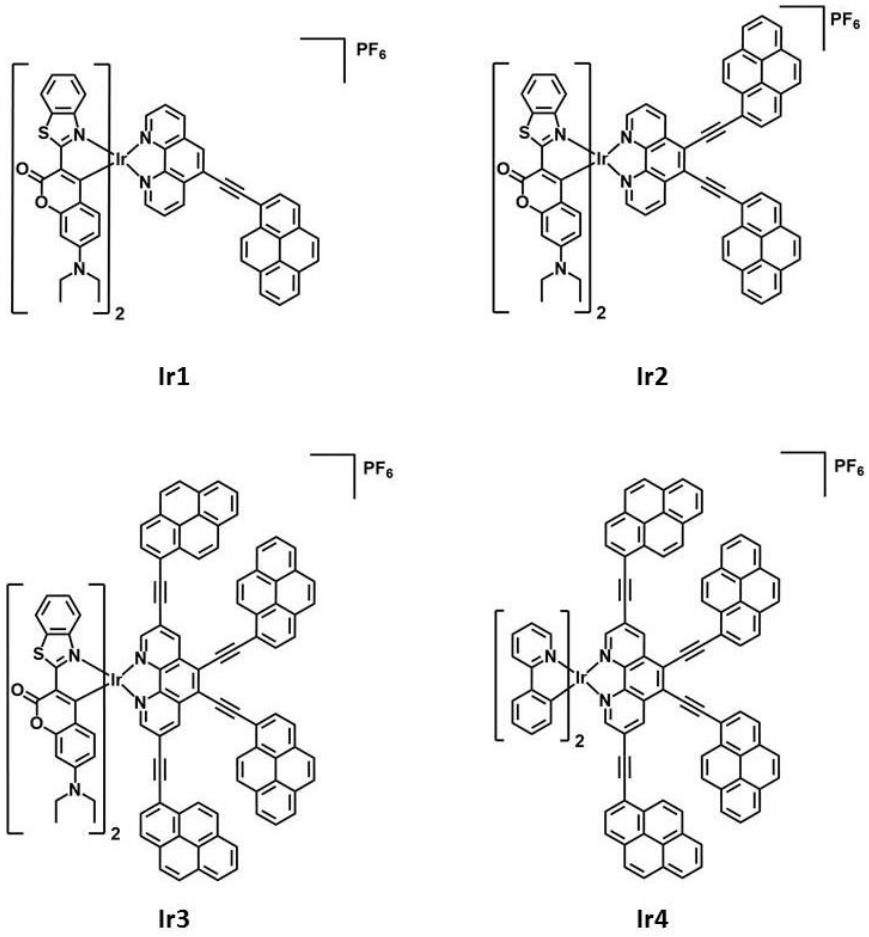

***Figure 2.1**: The structures of **Ir1**, **Ir2**, **Ir3** and **Ir4**.*

With the starting compound **IrBr3**, purification attempts were so hampered by the decomposition of the C6 ligand, that only ~1 mg of the EP product, **Ir3**, could be collected. Whilst that amount was sufficient to obtain a ^{1}H NMR spectrum, and a high resolution mass spectrum, there was an insufficient amount to obtain reliable photophysical measurements. As a result, several attempts were made to obtain **Ir3** *via* alternative routes.

Firstly, the off-complex synthesis of the ligand 3,5,6,8-tetrakis(pyren-1-ylethynyl)-1,10-phenanthroline (**L4**) was attempted using tetrakis(triphenylphosphine)palladium(0), ($Pd(PPh_3)_4$), as the Sonogashira coupling catalyst (Scheme 2.5). This catalyst does not require the use of the CuI co-catalyst, which can often coordinate to the bidentate phen-nitrogen heteroatoms, preventing further use. The solvent system was altered to replace dry MeCN with dry dimethylformamide (DMF). Two attempts of this reaction, a microwave-assisted reaction and a conventional setup, were unsuccessful.

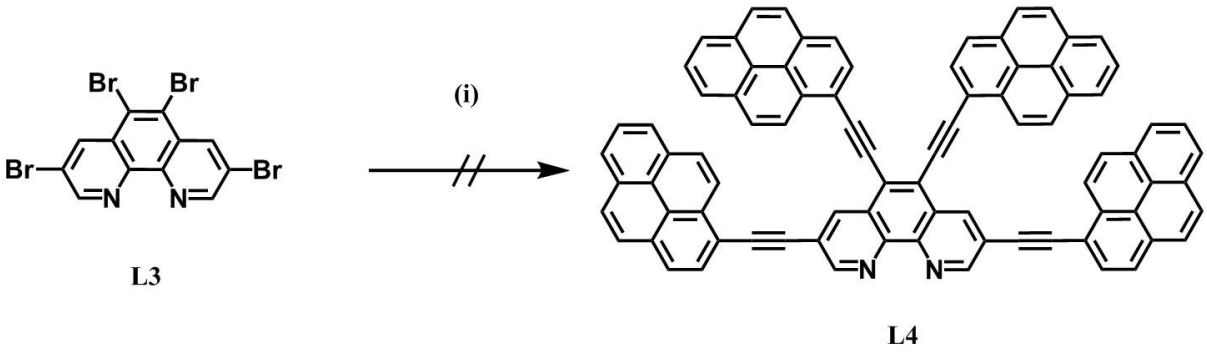

Scheme 2.5*: The attempted synthetic scheme of* ***L4****. (i) 1-ethynylpyrene, $Pd(PPh_3)_2$, PPh_3, DMF:Et_3N (5:2, v/v), 80°C, 48 hrs.*

After this, several attempts were made to carry out a Sonogashira cross-coupling reaction between trimethylsilylacetylene (TMSA), and the tetra-brominated precursor (**L3**). Successful generation of the tetra-ethynyl ligand (**L5,** Scheme 2.6) could then be used for a further Sonogashira coupling reaction with 1-bromopyrene (**L6**) to synthesis the desired tetra-EP ligand (**L4**). However, attempts to synthesis the tetra-ethynyl ligand (**L5**), both on- and off-complex, using TMSA were unsuccessful.

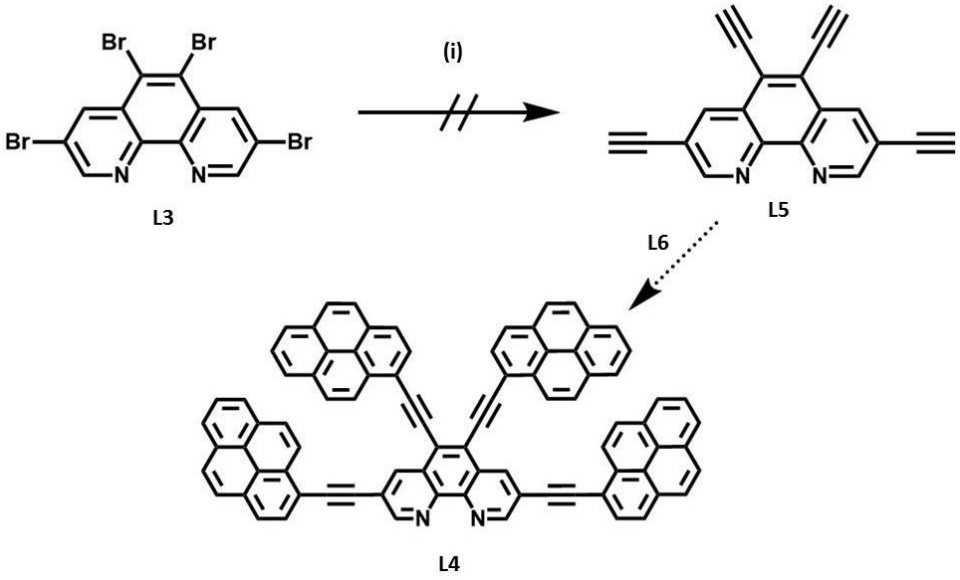

Scheme 2.6*: The attempted synthetic scheme of* ***L5****. (i) TMSA, $Pd(PPh_3)_4$, PPh_3, DMF:Et_3N (5:2, v/v), 80°C, 24 hrs.*

Despite the failure of the reaction attempts to synthesise **L4** off-complex, it was further postulated that the steric bulk of the bis-C6 auxiliary ligands may play a role in the unsuccessful attempts of the on-complex synthesis. The steric interaction between the EP moieties with the C6 ligands, and each respective EP moiety with another EP moiety, may have prevented the successful generation of **Ir3**. In Fig. 2.2, the optimised

geometries of both **Ir3** and **Ir4** are displayed (1) perpendicular to the planar phen moiety, and (2) in-plane with respect to the phen moiety. In **Ir3**, the acetylene moieties in the 3- and 8-positions of phen are forced out of their regular planar geometry, with all of the EP moieties twisted due to the steric bulk of the C6 auxiliary ligands. In the case of **Ir4**, this steric interference is absent through the use of the significantly smaller ppy ligands. The 3- and 8-position EP moieties are able to adapt the same coplanar orientation to the phen as those EP moieties in the 5- and 6-positions.

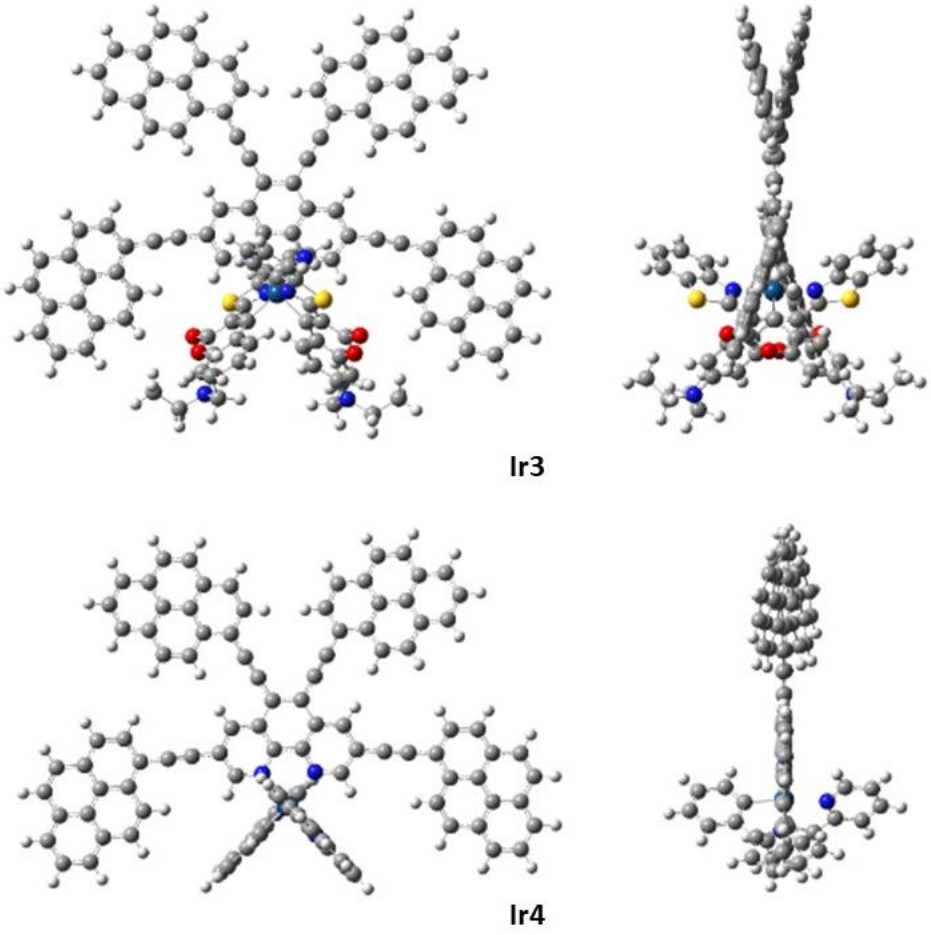

***Figure 2.2**: The optimised geometries of **Ir3** and **Ir4**, shown "face-on" on the left and "side-on" on the right. The calculations were performed at B3LYP/GENECP/LanL2DZ level with Gaussian 09W.*

The increased steric bulk of the C6 auxiliary ligands is likely to be a significant factor in the inability to generate **Ir3** in moderate yields. In order to further confirm this phenomenon, obtaining crystallographic data for **Ir4** will provide the "true" geometry of the EP moieties of **Ir3** (albeit limited to the solid state).

2.2 Structural Characterisation of Ir1 – Ir4

Each complex was assigned by a variety of NMR spectroscopy experiments as well as high-resolution mass spectrometry. The molecular mass of each complex was first confirmed by MALDI-TOF analysis. The mass spectrometry results are listed in Table 2.1, and a sample spectrum of **Ir1** is provided in the appendix. (Figure A.12).

Table 2.1*: MALDI-TOF results of the complexes* ***Ir1*** *–* ***Ir4****.*

Complex	Calculated Exact Mass (m/z)	Detected Mass (m/z)
Ir1	1295.2964	1295.2908
Ir2	1519.3590	1519.3618
Ir3	1967.4842	1967.4772
Ir4	1577.4134	1577.4209

The ^{1}H NMR spectra are presented in figure 2.4. The majority of the proton peaks are located in the range 6.0 – 9.5 ppm, with the noted exceptions of the methylene (~3.3 ppm) and methyl (~1.1 ppm) protons of the coumarin-6 ligands.

The spectrum obtained for **Ir1** is more complex than that of **Ir2**, **Ir3** or **Ir4** due to the asymmetric nature of the participating ligand. The low solubility of the samples in the available deuterated solvents also gave rise to challenging assignments and the need for repeated experiments. Therefore, nuclei are only given specific assignment where the assignment can be assured, and otherwise the assignment given is of the spin system or fragment in question. The assignment of **Ir1** is detailed here as a demonstration of the systematic approach used.

The ^{1}H-^{1}H COSY spectrum of **Ir1** was invaluable in its assignment, and is shown in figure 2.3 with spin systems highlighted. **Ir1** contains one 4-spin system, three 3-spin systems, four 2-spin systems and a 1-spin system. However, within the C6 ligand, the 2-spin and 1-spin systems which exist on the same ring interact on the ^{1}H-^{1}H COSY to appear as a 3-spin system. The methylene and methyl protons of the C6 are assigned easily in the aliphatic region.

Using the ^{1}H-^{1}H COSY, and by useful comparison to previously assigned, similar complexes[25, 28] the spin systems of the C6 ligand are quickly identified. The only 4-spin system displayed is assigned as that of C6, while comparison to the previously published work allows the *pseudo*-3-spin system to be quickly identified. This *pseudo*-3-spin system is confirmed by the weak coupling of its first and third proton signals. Furthermore, the individual protons of one of the 3-spin systems of the phen-fragment were assigned by use of both the ^{1}H-^{1}H COSY and HSQC spectra as their coupling appears weak on the ^{1}H-^{1}H COSY. The other 3-spin system was identified, but will require higher resolution scanning to be able to identify the individual protons. The singlet peak of the 6-position proton of the phen was also located within a multiplet.

The protons of the pyrene moiety were also challenging to assign. Without higher resolution HSQC and HMBC spectra, these cannot be individually assigned. However, the 2-spin system closes to the ethynyl linkage could be separated from the mass as it is the most deshielded pair of proton signals in the pyrene.

This method of multinuclear and varied NMR experimental spectra, coupled with comparison to previously published compounds, was used to assign all of the complexes in this chapter. However, to be able to fully assign each atom in each complex it will be necessary to carry out further experiments on the samples and potentially identify solvents in which the solubility of **Ir3** and **Ir4** is markedly better. The assignment was aided by an array of 2-dimensional NMR spectra, including COSYs, TOCSYs and DEPT experiments. The most relevant 2D spectra of **Ir1 – Ir4** are included in the annex. (Figures A.1 – A.7)

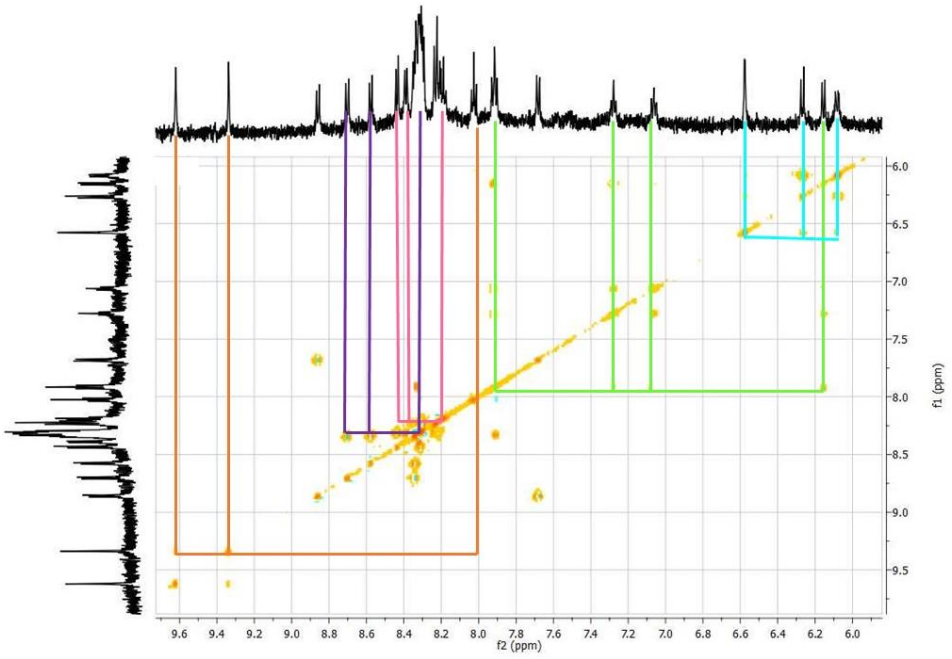

***Figure 2.3**: The ^{1}H-^{1}H COSY of **Ir1**, including the assignment of each spin system.*

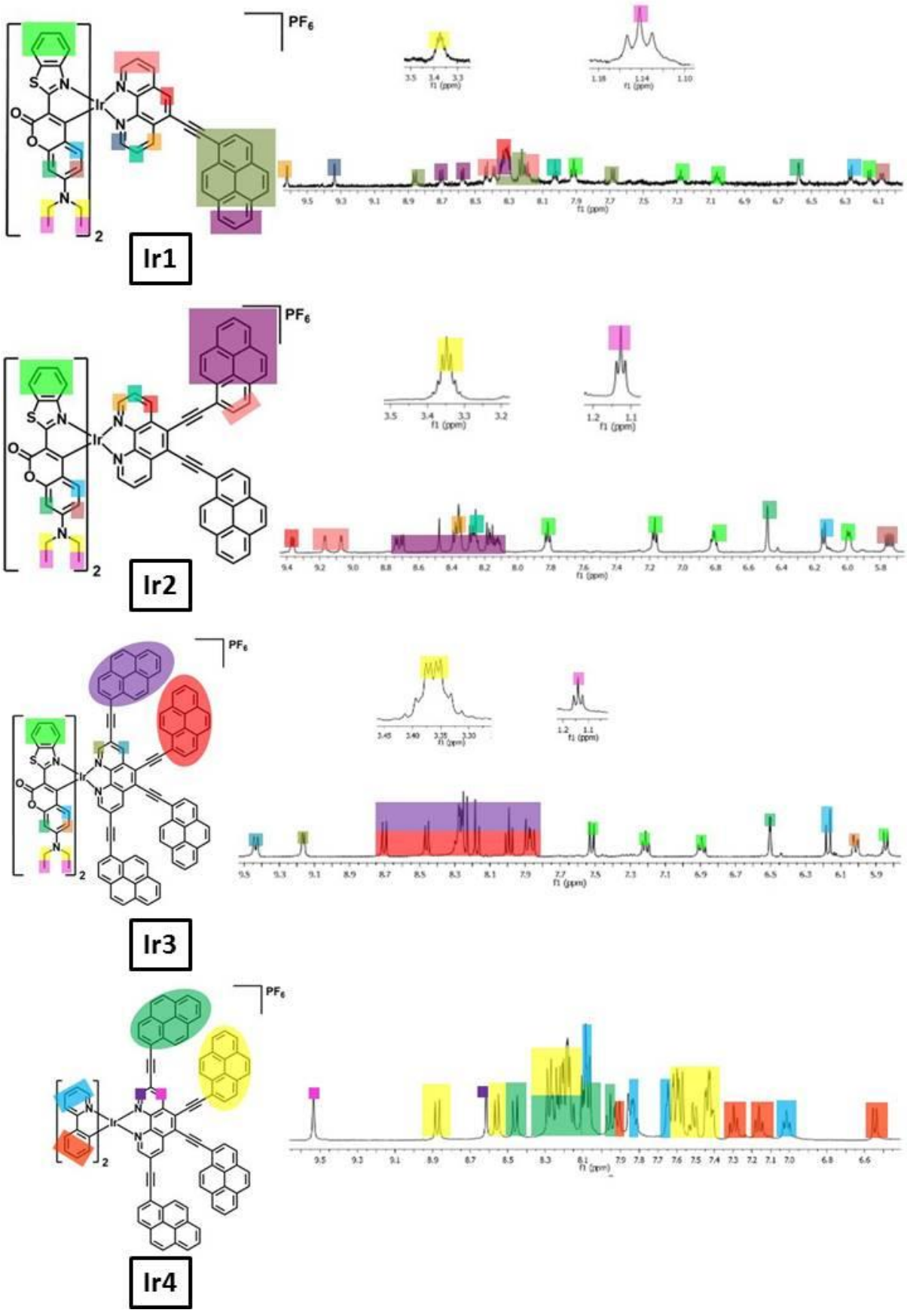

***Figure 2.4**: The assigned ^{1}H NMR spectra of **Ir1** – **Ir4**.*

2.3 Synthesis of Ir5 and Ir6

2.3.1 Bromination of 1,10-phenanthroline

A near-identical route was used to generate both **Ir5** and **Ir6**, the exception being the selective bromination of 1,10-phenanthroline (phen, **L0**). The bromination reactions carried out are detailed in Scheme 2.7. For the synthesis of 3-bromo-1,10-phenanthroline (**L7**, Scheme 2.7), 1-chlorobutane was used as the solvent according to literature.[99] Pyridine and sulphur monochloride (S_2Cl_2) were used in catalytic amounts, and added dropwise. The solution was reacted at reflux for 10 hours. The reaction time was limited to 10 hours in an attempt to avoid over-bromination of **L0** and to limit production of 3,8-dibromo-1,10-phenanthroline (**L8**, Scheme 2.7). This was successful and after work-up and purification by column chromatography (mobile phase CH_2Cl_2:MeOH, 100:1, v/v) yielded **L7** at 14 %, and **L8** at 17 %. The low yields were also due to the short reaction time. The 5-bromo-1,10-phenanthroline (**L1**) was previously prepared, as shown in Section 2.1.1.

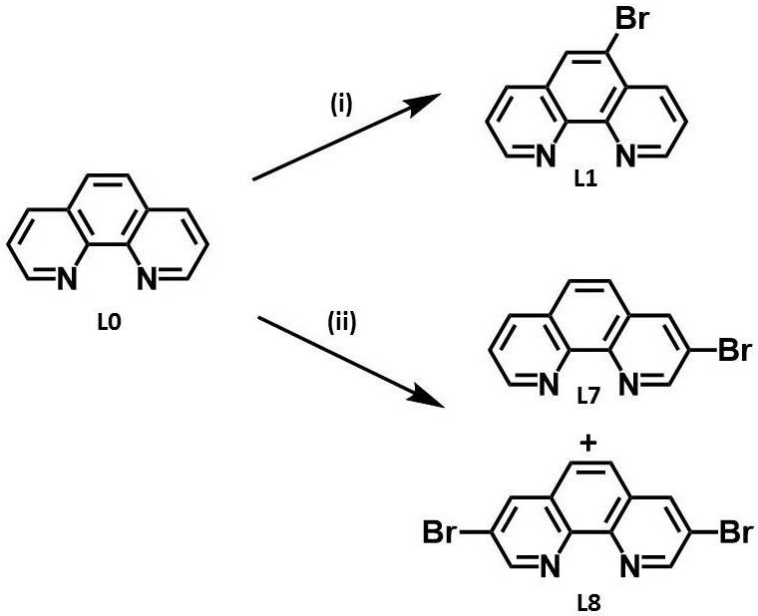

Scheme 2.7*: The synthesis of 5-bromo-1,10-phenanthroline (**L1**), 3-bromo-1,10-phenanthroline (**L7**) and 3,8-dibromo-1,10-phenanthroline (**L8**). (i) $H_2SO_4.SO_3$ (30 %), Br_2, 135°C, high pressure, 23 hrs, yield: 12 %; (ii) 1-chlorobutane, pyridine, S_2Cl_2, Br_2, 110°C, 10 hrs, yield: **L7** (14 %), **L8** (17 %).*

2.3.2 Coordination of Brominated 1,10-Phenanthroline to Ir(III) Metal Centres

The iridium dimer starting material $Ir(ppy)_2(\mu\text{-}Cl)]_2$ (Irppy0, Scheme 2.8) was also previously prepared (Section 2.1.2) and was coordinated to the purified ligands **L1** and **L7**. As before, the coordination reaction was carried out in CH_2Cl_2 at reflux, with several drops of MeOH added to aid solubility.[25] Upon cooling, a saturated solution of KPF_6 in MeOH was added. This counterion allowed the product to be precipitated from CH_2Cl_2 using hexanes, and then filtered. The solid orange products (Scheme 2.8) were purified by column chromatography (CH_2Cl_2:MeOH, 100:1, v/v) to yield **IrBr5** (78 %) and **IrBr6** (91 %).

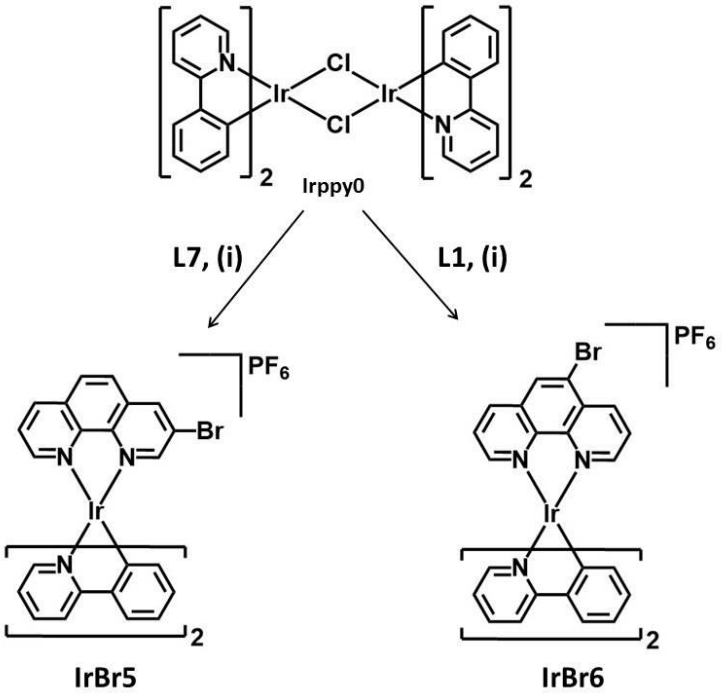

Scheme 2.8*: The synthesis of* ***IrBr5*** *and* ***IrBr6****. (i) CH_2Cl_2:MeOH (40:1, v/v), 50°C, 4 hrs, yield:* ***IrBr5*** *(78 %),* ***IrBr6*** *(91 %).*

2.3.3 Sonogashira Cross-Coupling Reactions of IrBr5 and IrBr6 to 1,6-Diethynylpyrene

The core ligand of the dinuclear complexes **Ir5** and **Ir6**, 1,6-diethynylpyrene (DEP, **L9**, Scheme 2.9) was synthesised *via* Sonogashira cross-coupling reaction between 2-methylbut-3-yn-2-ol and 1,6-dibromopyrene (**L10**). The product of this reaction, 4,4'-(pyrene-1,6-diyl)bis(2-methylbut-3-yn-2-ol) (**L11**), was deprotected by boiling in a solution of NaOH (1 eq.) in toluene (25 ml) overnight. The resulting product was purified by column chromatography (Petroleum ether:EtOAc, 70:30, v/v) and identified by ^1H NMR spectroscopy.

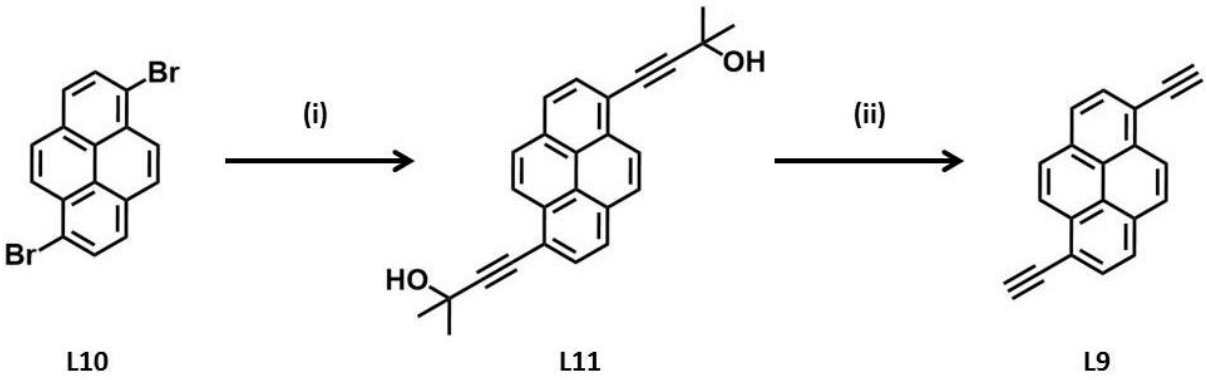

Scheme 2.9*: The synthesis of* ***L9****. (i) DMF:Et_3N (5:2, v/v), $Pd(PPh_3)_2Cl_2$, PPh_3, CuI, 2-methylbut-3-yn-2-ol, 80°C, 24 hrs; (ii) NaOH, toluene, 120°C, 12 hrs, yield: 59 %.*

Ir5 and **Ir6** were generated *via* further Sonogashira cross-coupling (Scheme 2.10) between **L9** and two equivalents of the respective precursor, **IrBr5** or **IrBr6**.

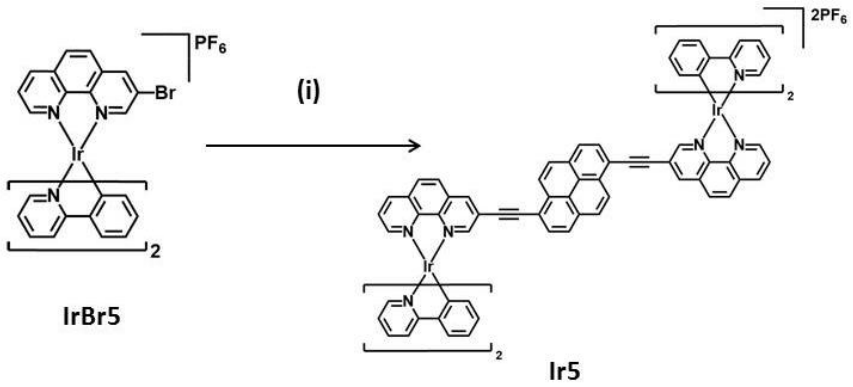

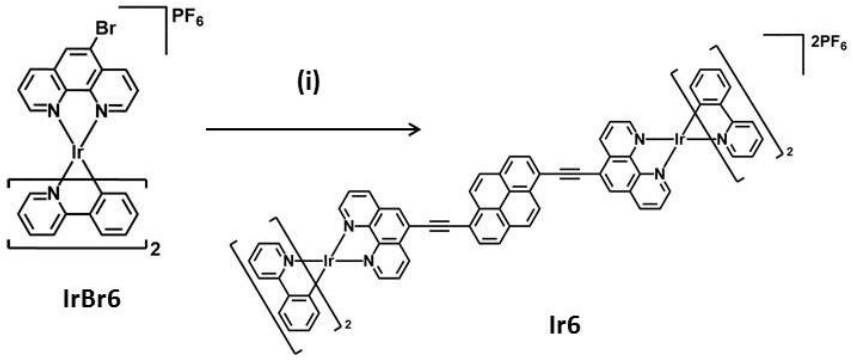

Scheme 2.10*: The Sonogashira cross-coupling reactions used to generate* ***Ir5*** *and* ***Ir6****. (i) 1,6-diethynylpyrene, $Pd(PPh_3)_2Cl_2$, PPh_3, CuI, MeCN:Et_3N (5:2, v/v), 80°C, 24 hrs, yield: Ir5 (19 %), Ir6 (24 %).*

Each reaction was carried out in a mixed solvent system of dry MeCN and distilled triethylamine (MeCN:Et_3N, 5:2, v/v). The solvent and reagents were degassed with N_2

before reaction. The reactions were successful and the products of each were purified first with column chromatography (CH_2Cl_2:MeOH, 100:1, v/v), and then by preparative TLC plate (CH_2Cl_2:EtOAc, 95:5, v/v), to yield the bright orange solids of **Ir5** (19 %) and **Ir6** (24 %).

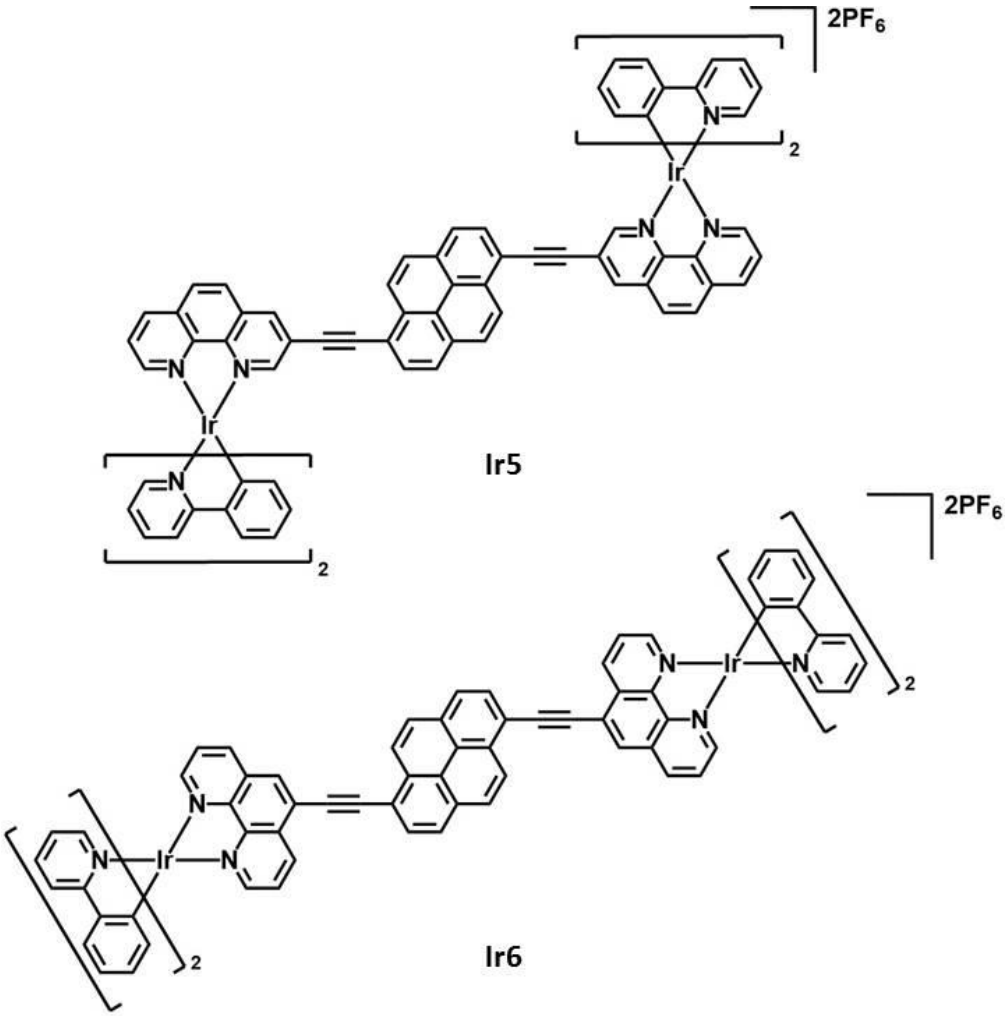

Figure 2.5*: The structures of* ***Ir5*** *and* ***Ir6****.*

2.4 Structural Characterisation of Ir5 and Ir6

Ir5 and **Ir6** were both assigned by multinuclear NMR spectroscopy, as well as by high-resolution mass spectrometry. The molecular mass of each complex was first confirmed by MALDI-TOF analysis. The mass spectrometry results are listed in Table 2.2. Both dinuclear species were observed with a single counterion detected in coordination.

***Table 2.2**: MALDI-TOF results of the complexes **Ir5** and **Ir6**.*

Complex	Calculated Exact Mass (m/z)	Detected Mass (m/z)
Ir5	1753.3372	1753.3339
Ir6	1753.3372	1753.3306

Figure 2.6 shows the ^{1}H NMR spectra of **Ir5** and **Ir6** with labelled assignments. The two species, being very similar in structure, give very similar spectra. However, one key difference is the differentiation of ppy ligands. For **Ir5**, the two ppy ligands on a single Ir-centre give clear, non-overlapping signals. These are labelled easily by using the ppy diagram on either side of the molecular diagram in Figure 3.2, but describe the two different ppy ligands on one single metal centre. In **Ir6**, the ppy ligands on the same metal centre have different but overlapping signals which cannot be identified separately and so all phenyl rings are labelled using the same colour, as are the pyridyl rings.

The chief difference in the assignment of these compounds, as opposed to those of **Ir1** – **Ir4**, was the symmetry of the dinuclear complexes, and the use of ppy ligands. The ppy ligands were easily identified in ^{1}H-^{1}H COSY spectra as relatively deshielded 4-spin systems, and the phen and pyrene proton signals were identified by a combination of proton and carbon experiments. One difficulty in obtaining a clear spectrum was the low solubility of both **Ir5** and **Ir6**.

The assignment was aided by an array of 2-dimensional NMR spectra, including COSYs, TOCSYs and DEPT experiments. The most relevant 2D spectra of **Ir5** and **Ir6** are included in the annex. (Figures A.8 – A.11)

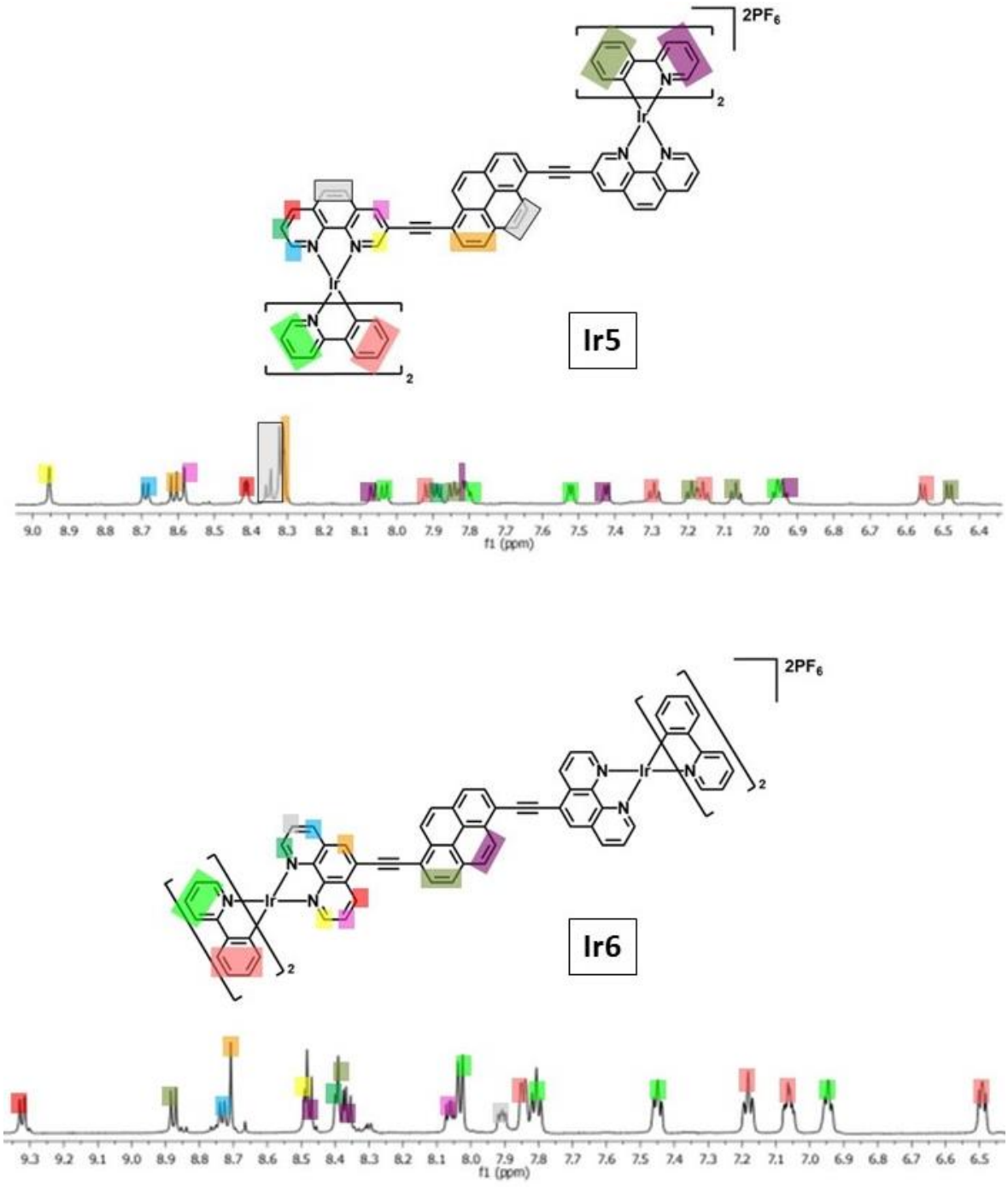

***Figure 2.6**: The assigned ^{1}H NMR spectra of **Ir5** and **Ir6** (ppm).*

Chapter 3

Photophysical Measurements of Coumarin-6- and Phenylpyridine-based Ir(III) Complexes for Triplet-Triplet Annihilation Upconversion

3.1 Photophysical Studies of Ir1 – Ir4

A number of photophysical measurements of the complexes were collected; UV-vis absorption spectra, emission spectra, and phosphorescence lifetimes. Emission spectra were collected in air and degassed in Ar, low temperature emission spectra (77 K) were also taken for comparison to those collected at RT. Analysis of all of the data obtained from these measurements can be used to confirm the character of the most significant excited states of each complex, giving an indication as to their suitability for use as triplet photosensitisers in TTA-UC processes.

There are three main types of photophysical transition involved across the range of photophysical measurements described here: a vertical intraligand (IL) transition, a ligand-to-ligand charge transfer (L'LCT) and an intraligand charge transfer (ILCT). Where the ligand in question is the ancillary ligand, L' is used to denote it, whereas L is used to denote the respective phen-pyrene fragment of each product. As the metal-centred (MC) excited states are too high in iridium to access due to high ligand field splitting,[51] any metal involvement is in the form of a ligand-to-metal charge transfer (LMCT) or a metal-to-ligand charge transfer (MLCT).

3.1.1 Steady-State UV-Vis Absorption Spectra of Ir1 – Ir4

The room temperature UV-vis absorption spectra of **Ir1** – **Ir4** were measured in five solvents of increasing polarity (toluene, CH_2Cl_2, MeCN, EtOH, and MeOH), and are presented in Figure 3.1.

There were minimal changes in the wavelength of maximum absorption (λ_{max}) with changing of the solvent polarity. This indicated that the ground state of each complex was unaffected by solvent polarity, and thus the photophysical properties of each complex are hereafter compared in MeCN only. A solution of 1 x 10^{-5} M was used for each photophysical measurement.

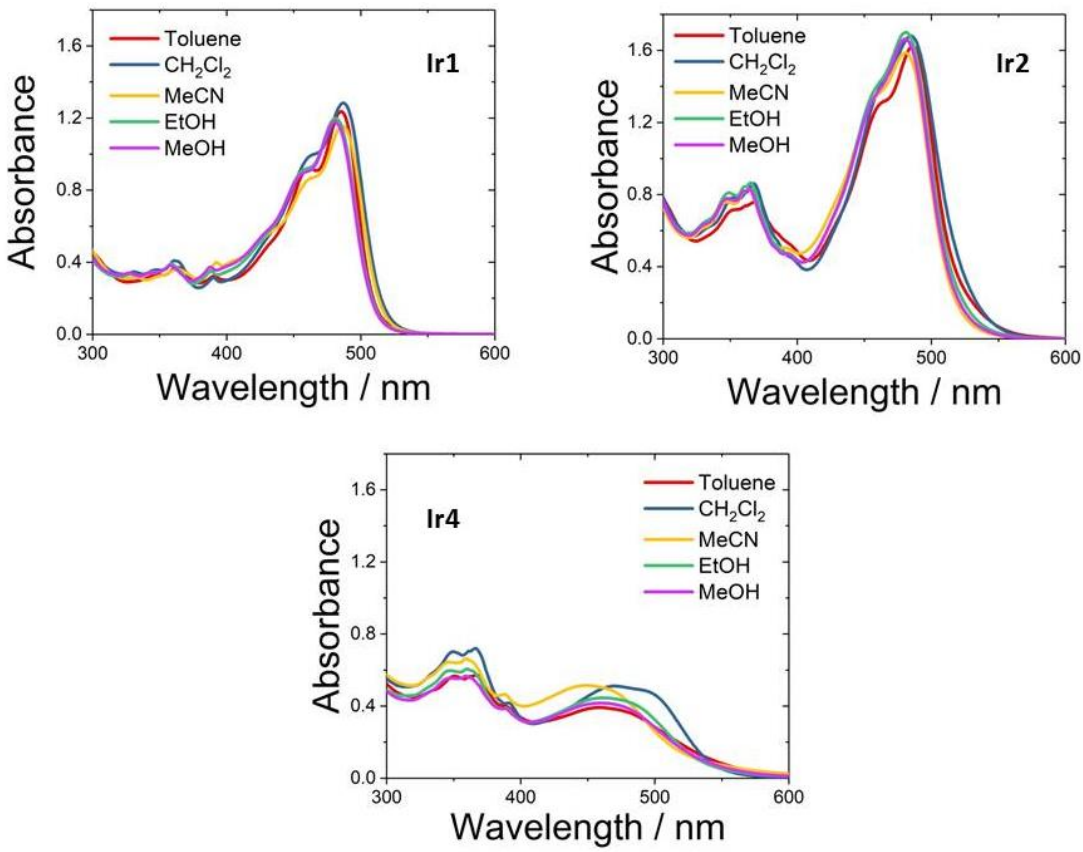

***Figure 3.1**: Absorption spectra of **Ir1** – **Ir4** in five different solvents (toluene, CH_2Cl_2, MeCN, EtOH, MeOH), c = 1 x 10^{-5} M, RT.*

The absorption profiles of **Ir1** and **Ir2** are nearly identical in their structure but differ as expected in their intensity. The characteristic peaks of ethynylpyrene are seen around λ_{abs} = 360 nm, while the two main peaks in the region 450 – 500 nm are due to C6-based transitions[28] (^{1}IL', ^{1}L'LCT), however the presence of the pyrene ligands (^{1}IL, ^{1}ILCT) contributes to the molar absorptivity. These peaks cause the greater intensity in **Ir2** (ε_{485} = 1.59 x 10^5 M^{-1} cm^{-1}, ε_{460} = 1.35 x 10^5 M^{-1} cm^{-1}) due to the presence of a second EP moiety compared to **Ir1** (ε_{480} = 1.28 x 10^5 M^{-1} cm^{-1}, ε_{460} = 9.20 x 10^4 M^{-1} cm^{-1}). The peak centred at approximately 485 nm is due to a red-shifted absorption of the C6 ligands (λ_{abs} = 457 nm, ε = 5.4 x 10^4 M^{-1} cm^{-1} in EtOH), which is due to the coupling of the C6 to the Ir(III) complex. These absorptions are assigned as being a combination of two spin-allowed absorption transitions – a ^{1}IL transition on the C6 ligands, and a C6-to-phen ^{1}L'LCT transition. The contributions of the pyrene (^{1}IL, ^{1}ILCT) are assumed to be solely to the intensity and do not appear to affect the C6-derived structure, as previously reported.[28]

As expected, the use of C6 ligands in place of the more commonly used auxiliary ligands of ppy, causes a significant increase in the intensity of the visible region absorption of the metal complex. This has been previously reported in the literature.[28]

In the case of **Ir4**, the absorption intensity is markedly weaker than that of the C6-bearing complexes. However, the absorption of the EP ligands is noticeable broader in the visible region on coupling to the Ir(III) complex than solely in 1-ethynylpyrene. On closer inspection, the main, broad absorption band (~450 – 500 nm) appears to be a combination of bands though they cannot be distinguished as they are not sharp enough. The transition is tentatively assigned as an ILCT transition from the pyrene to the phen fragments. It is also significantly red-shifted compared to the 1-ethynylpyrene ligand on its own. The higher energy peaks around 350 nm in the spectrum of Ir4, which also appear to be characteristic peaks of EP moieties,[28] remain sharp and appear more intense as a result. There are again minimal solvatochromic effects on **Ir4**, however main peak at roughly λ_{abs} = 460 nm is slightly blue-shifted in MeCN to 450 nm, and slightly red-shifted in CH_2Cl_2 to 470 nm. This is again significantly red-shifted from the absorption of 1-ethynylpyrene as would be expected on complexation to an Ir(III) centre.

3.1.2 Emission Spectra of Ir1 – Ir4

The emission spectra of **Ir1** – **Ir4** were collected and studied as solutions in air and degassed with Ar in MeCN (1×10^{-5} M). The emission profiles of each complex are very different between the air and degassed solution, confirming the phosphorescent character of their emission as they are quenched by triplet oxygen. The spectra are presented in Fig. 3.2.

For **Ir1**, the most significant peak appears at 680 nm, and is fully quenched in air. A phosphorescence lifetime measurement was obtained for **Ir1**. The lifetime of the emission at 680 nm was measured using an excitation of 440 nm. In this case, the triplet lifetime (τ_T) was recorded as 262.6 μs, significantly longer than that of the corresponding complex substituted with the EP moiety in the 3-position of the phen (X1, Figure 3.4), previously reported as 172.8 μs.[28] Due to the structured, triplet emission profile, in conjunction with the TDDFT-generated triplet excited state map (Figure 2.14) and in line with previously reported measurements,[28] the emission here is tentatively assigned as ^{3}IL' (i.e. based on

the C6 ligand). The structured emission and long-lived triplet lifetime is indicative of a ^{3}IL' state, rather than a ^{3}ML'CT which is generally much shorter lived than ^{3}IL'.[28]

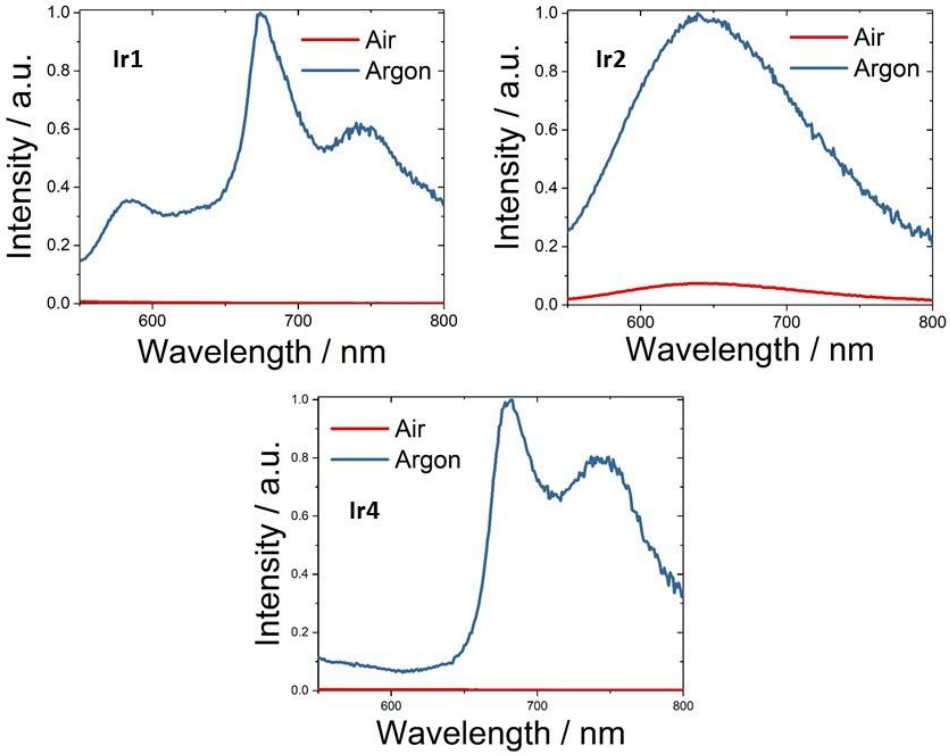

***Figure 3.2**: The normalised emission spectra of **Ir1** – **Ir4** measured in air and under Ar, in MeCN, λ_{ex} = 440 nm.*

The emission of **Ir2** is again mostly quenched in air. As opposed to **Ir1**, the emission band (λ_{em} = 640 nm) of **Ir2** does not show a detailed structure. This suggests that while the emission originates from a triplet state, it is not generated by the same transitions as **Ir1**. Therefore, based on the TDDFT-derived T_1 state map of **Ir2** which shows the triplet state to be located over the pyrene-phen ligand, and comparison to similar complexes,[25, 28] the emission here is tentatively assigned as a ^{3}ILCT process centred on the pyrene-phen fragment.

The emission of **Ir4** is also quenched in air. This again suggests that this emission profile is generated by a triplet excited state. The triplet excited state is tentatively assigned as being ^{3}ILCT in nature and located across the phen-pyrene ligand, similar to previously published structures,[25] without the strong C6 chromophores present. This assignment is reinforced by the results of the TDDFT-generated triplet excited state map of **Ir4** (figure 3.14). The presence of two bands here may be due to two competing ^{3}ILCT processes –

one from the 3- and 8-position EP moieties into the phen, and one from the 5- and 6-position EP moieties.

***Table 3.1**: The photophysical data of complexes **Ir1** – **Ir4**.*

	λ_{abs} / nm	ε / M^{-1} cm^{-1}	λ_{em} / nm	τ_p / µs (RT)
Ir1	480, 460	1.28×10^5, 9.2×10^4	680	262.64
Ir2	485, 460	1.59×10^5, 1.35×10^5	640	-
Ir4	460	5.1×10^4	680	-

Figure 3.3 shows the normalised emission spectra of **Ir1** – **Ir4**, both at RT and at 77K under Ar. The major bands of **Ir1** and **Ir4** show very small shifts in wavelength. Such small Stokes shifts generally suggest a ^{3}IL emissive state rather than a ^{3}MLCT state,[50, 100] and these low-temperature emission spectra appear to support the assertion that the emission spectra originate in ^{3}IL' and ^{3}ILCT bands, respectively. The emission of **Ir2** shows a small red-shift of $\Delta\lambda_{max}$ = 39 nm. The structures emission profile at 77 K, coupled with the small shift in band maximum, again supports the assertion that the emission of **Ir2** originates in a ^{3}ILCT.

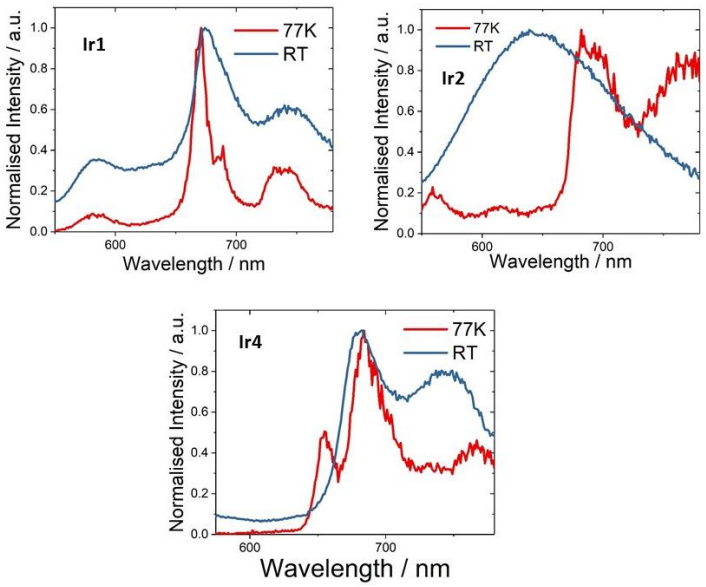

***Figure 3.3**: The emission spectra of **Ir1** – **Ir4** measured at 77 K, and at RT under Ar, in MeCN, λ_{ex} = 440 nm.*

3.1.3 Further Photophysical Characteristics of Ir1 – Ir4

Each of these products can be further evaluated for their use in singlet oxygen sensitisation studies, transient absorption studies, triplet quenching studies, and their upconversion quantum yields. There was an opportunity to test **Ir1** towards these studies, however the remaining compounds generated are awaiting the opportunity to be tested in Dalian University of Technology China, beyond the date of submission of this report.

The properties of **Ir1** will be compared to the published[25, 28] properties of three complexes with structures similar to **Ir1** (Fig. 3.4): **X1** as it currently has the highest upconversion yield for an Ir-coumarin-6 triplet photosensitiser (Φ_{UC} = 27.5%); **X2** as it is the analogous complex to Ir1 where the C6 ancillary ligands are replaced with ppy ligands; and **X3**, which currently has one of the highest TTA-UC quantum yields for an iridium triplet photosensitiser (Φ_{UC} = 30.2 %). Also used for comparison are **X4** and **X5,**[101] which are iridium-ppy based photosensitisers which have phen-based participating ligands which incorporate coumarin-like moieties.

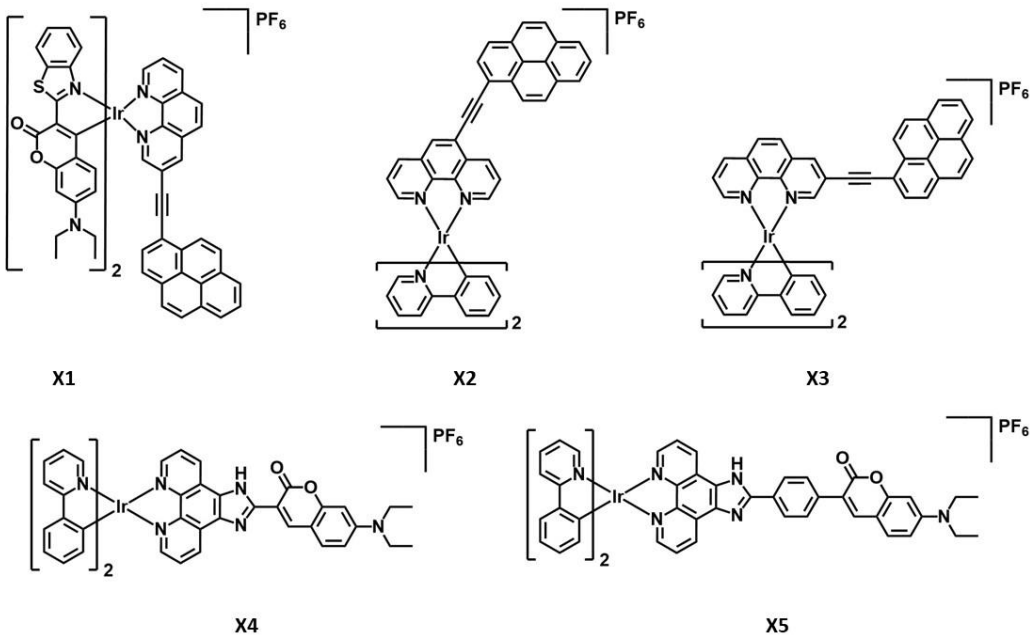

***Figure 3.4**: The structure of **X1**, **X2** and **X3**, the previously reported analogues to **Ir1**, and **X4** and **X5**.*

In order to gauge the ability of **Ir1** to undergo a TTET process with another triplet molecule, as this is a key step in the TTA-UC photophysical pathway, its singlet oxygen sensitisation quantum yield will be measured. The measurement was carried out by irradiation with monochromatic light of a solution of **Ir1** and 1,3-diphenylisobenzofuran (DPBF). DPBF is strongly coloured and absorbing, and its absorption at 415 nm is characteristic. Reaction with singlet oxygen results in the formation of colourless 1,2-dibenzoylbenzene. On irradiation with monochromatic light, the excitation of **Ir1** results in an excited triplet state which can then react with ground-state triplet oxygen to form reactive singlet oxygen. This can then react with DPBF, and the rate of the decrease in absorption of DPBF in solution can be directly related to the rate of singlet oxygen generation. The results are presented in Fig. 3.5. The absorption contribution of **Ir-1** does not interfere with that of the DPBF as their peak maxima do not overlap and the decrease in the molar absorptivity is consistent with DPBF alone.

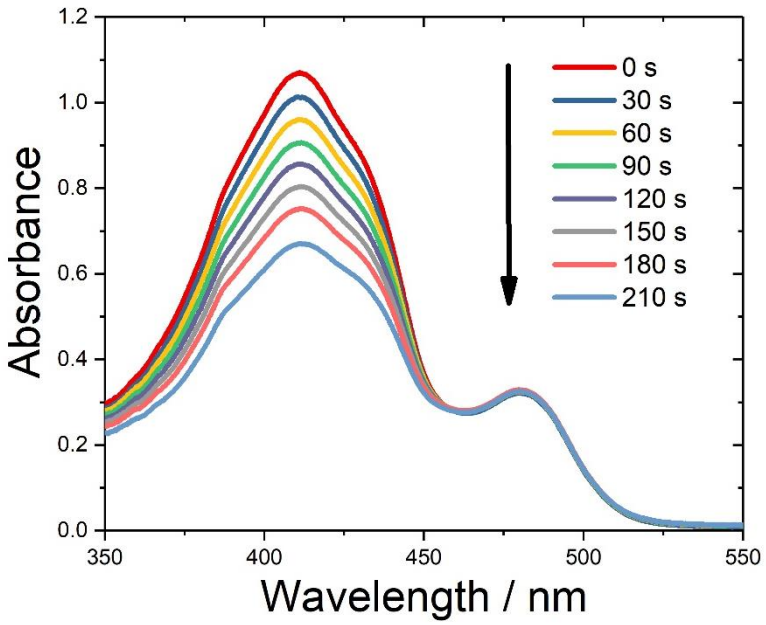

***Figure 3.5**: The absorption change of DPBF in the presence of **Ir1** after each irradiation, λ_{ex} = 461 nm.*

The quantum yield of singlet oxygen (Φ_Δ) of **Ir1** was determined by comparison to that of $[Ru(bpy)_3][2PF_6]$, and gave a value of Φ_Δ = 76.6 %. This high value is a good indication that **Ir1** may be applicable as a commercial triplet photosensitiser. In comparison, **X1** had a measured singlet oxygen sensitivity of Φ_Δ = 81.5 %. The singlet oxygen sensitivity of **X2** – **X5** were not published.

Next, the nanosecond time-resolved transient absorption of **Ir1** was measured in order to further investigate the nature of the first excited state of the complex. The results are graphed in Figure 3.6.

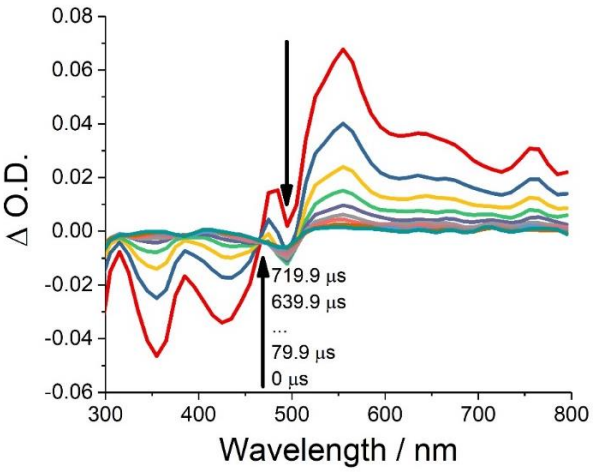

***Figure 3.6**: The nanosecond time-resolved transient difference absorption spectrum of **Ir1**, λ_{ex} = 440 nm, in CH_2Cl_2 under N_2, RT.*

The ground-state bleaching seen between 300 – 460 nm is due to the absorption at those wavelengths of the ground-state of **Ir1**. However, there is significant transient absorption seen above 460 nm, with a small peak centred at 480 nm and further red-shifted absorption (large peak at 550 nm). This data confirms the existence of a long-lived triplet excited state, with a sufficient lifetime on excitation necessary for the transient absorption to occur. The long lifetime agrees with the initial assignment of the excited state of **Ir1** as a ^{3}IL state. The transient absorption is similar to that seen in **X1** – **X5,**[101] all of which show transient absorption bands above 460 nm.

The triplet quenching ability of **Ir1** was also measured in order to get a more accurate indication of its TTET ability. The data was generated by measuring the triplet lifetime of the complex in the presence of increasing concentrations of 9,10-diphenylanthracene (DPA), which causes a decrease in the lifetime of the solution by increasingly quenching the triplet state. The Stern-Volmer plot of the data obtained is shown in Figure 3.7. The value of the Stern-Volmer constant, K_{SV}, and the bimolecular quenching constant, k_q, are calculated by fitting the data to the Stern-Volmer equation:

$$\frac{I_0}{I} = \frac{\tau_0}{\tau} = 1 + K_{SV}[Q], K_{SV} = k_q * \tau_0$$

where I_0 and τ_0 represent the phosphorescence intensity and triplet lifetime of the photosensitiser respectively in the absence of the quencher (DPA), I and τ represent these values in the presence of the quencher, and [Q] is the concentration of the quencher.

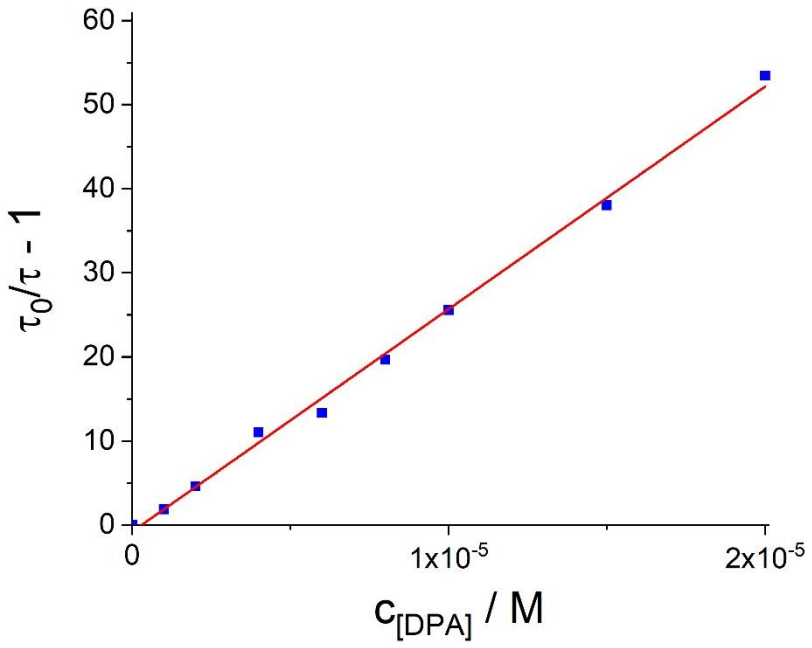

***Figure 3.7**: The Stern-Volmer plot generated from the quenching lifetime of **Ir1** (λ_{ex} = 440 nm), measured as a function of DPA (triplet quencher) concentration in CH_2Cl_2, RT. R^2 = 0.9968.*

The K_{SV} of **Ir1** is calculated from the plot as 2.65 x 10^6 M^{-1}. This is a very high value, but this was expected due to the long lifetime of **Ir1**. In comparison, the K_{sv} values of **X1**, **X2 and X3** are 3.88 x 10^5 M^{-1}, 6.30 x 10^5 M^{-1} and 8.47 x 10^5 M^{-1} respectively. **X4** and **X5** also show[101] high K_{SV} values of 5.51 x 10^5 M^{-1} and 3.18 x 10^5 M^{-1}. In most cases, these values are in the range of 10^2 – 10^4 times higher than the brominated precursor of the respected complex, or the analogue of the respective complex without its key chromophore.

Finally, the upconversion quantum yield (Φ_{UC}) was measured by the emission of DPA in the presence of **Ir1** using a 473 nm laser light source (Figure 3.8). The measurement is represented in Figure 2.11, showing the emission of DPA in the presence and absence of **Ir1**. The small peak marked with an asterisk (*) is the peak of the laser source; its contribution to the emission is deducted during the calculation of the quantum yield. The calculation of the quantum yield is carried out by reference to a standard using the following equation:

$$\Phi_{UC} = 2\Phi_{std} * \left(\frac{1-10^{-A_{std}}}{1-10^{-A_{sam}}}\right) * \left(\frac{I_{sam}}{I_{std}}\right) * \left(\frac{\eta_{sam}}{\eta_{std}}\right)^2$$

Equation 2.1.

Where the subscripts "sam" and "std" refer to the photosensitiser being tested and the standard being compared against, respectively, and Φ, A, I and η refer to the quantum yield, absorbance, integrated photoluminescence intensity and the refractive index of the solvents used respectively.

In this case, the Φ_{UC} value of **Ir1** is found to be 23.9 %. This is a high value though when compared again to **X1**, which has a value of Φ_{UC} = 27.5 %,[28] it becomes apparent that it is not the most convenient nor efficient complex available. X4 and X5 had reported upconversion yields of Φ_{UC} = 21.3 % and Φ_{UC} = 23.4 %, respectively.

In the cases of **X2** and **X3**, Φ_{UC} values of 20.9 % and 30.2 % were reported. This, alongside comparison to **X1**, suggests that substitution in the 3-position results in a more favourable upconversion yield than substitution in the 5-position. As the synthesis of 3-bromo-1,10-phenanthroline (**L7**, Fig. 2.7) is far more convenient, safe and high-yielding than that of 5-bromo-1,10-phenanthroline (**L1**, Fig. 2.1) it is proposed that future work should focus on such 3-substituted complexes.

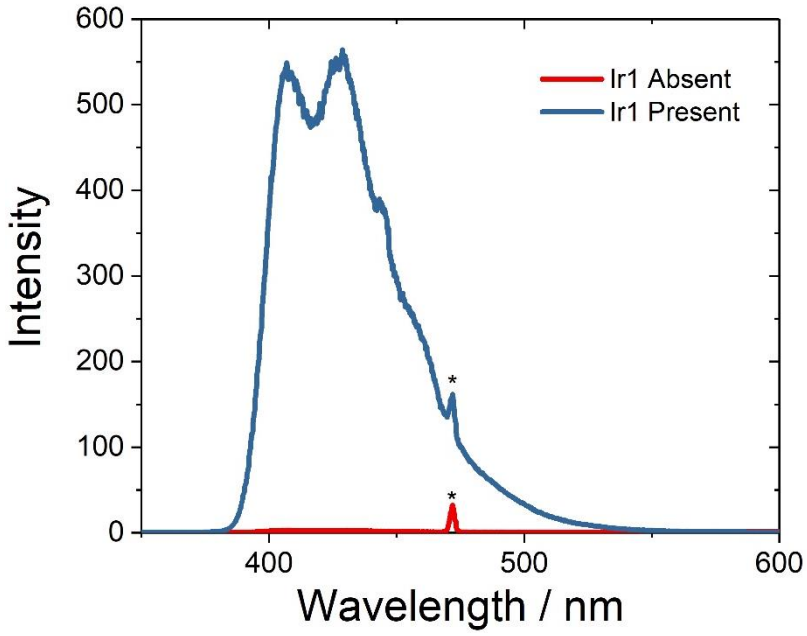

***Figure 3.8**: The upconversion spectrum of **Ir1** as a triplet photosensitiser in the presence of DPA (blue), and the emission spectrum of **Ir1** in the absence of DPA (red).*

3.2 Cyclic Voltammetry Studies of Ir1 – Ir4

Cyclic voltammetry (CV) studies were carried out on 1 x 10^{-4} solutions of **Ir1** – **Ir4** in CH_2Cl_2 (with 0.1 M nBu_4NPF_6). The cyclic voltammograms were recorded using a glassy carbon working electrode, a Ag/AgCl reference electrode, and a Pt wire counter electrode.

The oxidation wave of each sample appears beyond the solvent window of CH_2Cl_2. This is not always the case,[102] however in this case it may be due to the low-lying nature of the HOMO states in each complex. As well as that, it appeared that the reduction of **Ir4** was outside the solvent window. However, the reductive processes of **Ir1** and **Ir2** were obtained and are shown below. Each voltammogram was initially run between 0 and -2.5 V, followed by a narrower window (-2 V) in order to avoid issues with solvent reduction processes that may occur close to the window edge. Table 2.3 shows the values of the reduction voltammograms of **Ir1** and **Ir2**.

Figure 3.9 is the reduction of **Ir1**.

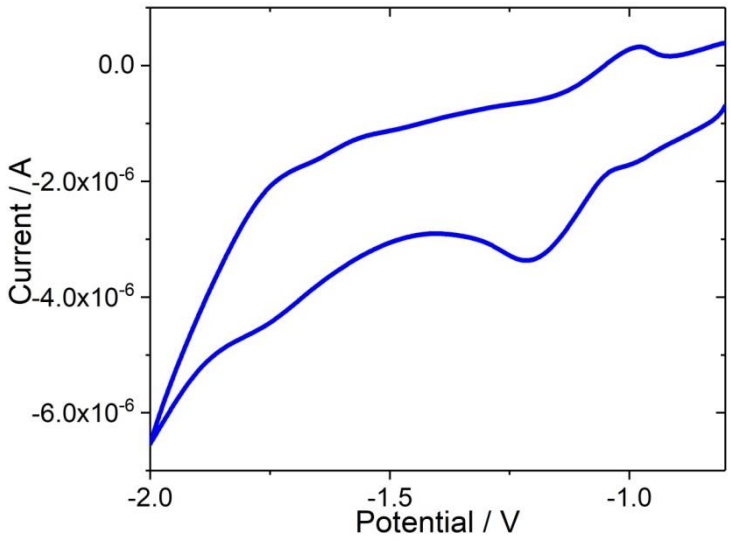

***Figure 3.9**: The reductive cyclic voltammogram of **Ir1**. (CH_2Cl_2, 0.1 M $TBAPF_6$, scan rate = 0.1 V/s)*

There is a clear reduction visible with a peak height of E_{pc} = -1.22 V, which is not reversible. It is postulated that this is the reduction of the extended phen-pyrene ligand,

and this is confirmed by the TDDFT results which indicate that the LUMO of **Ir1** is located on the participating ligand (Fig. 3.15).

Figure 3.10 is the reduction of **Ir2**.

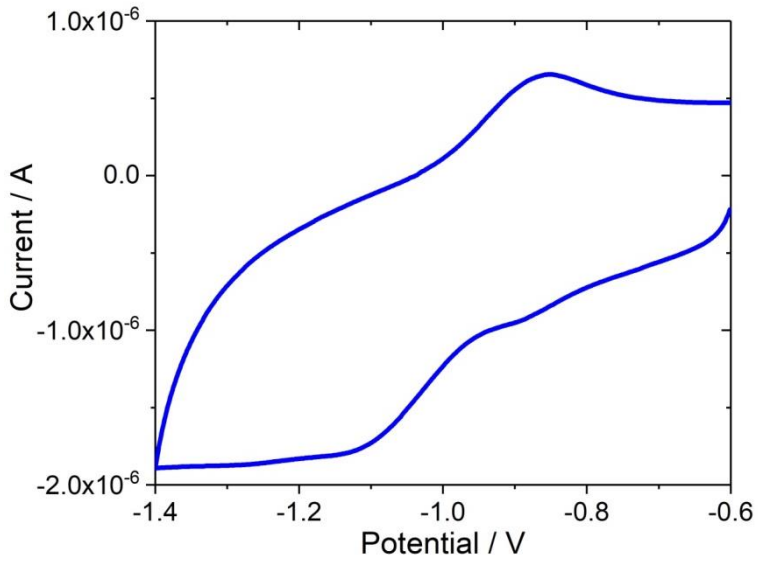

***Figure 3.10**: The reductive cyclic voltammogram of **Ir2**. (CH_2Cl_2, 0.1 M $TBAPF_6$, scan rate = 0.1 V/s)*

Again there is a clearly visible reduction peak at E_{pc} = -1.10 V, which is also irreversible. Again, this is postulated as the reduction of the phen-pyrene fragment, which is once more confirmed using TDDFT, which shows this is where the LUMO orbital of **Ir2** is located (Fig. 3.16).

***Table 3.2**: The cyclic voltammetry results of **Ir1** and **Ir2**.*

Complex	Reduction (E_{pc}/V)
Ir1	-1.22
Ir2	-1.10

3.3 Density Functional Theory Calculations of Ir1 – Ir4

Time-dependent density functional theory (TDDFT) calculations were carried out in Dalian University of Technology in order to further understand the nature of the excited states of the Ir(III) complexes.

The ground-state geometry of each complex was first determined. These geometries represent the lowest-energy arrangements possible, and are used to calculate the energy of each orbital. In each case the coupled ethynylpyrene moieties take a distorted coplanar position with respect to the phenanthroline moiety coordinated to the Ir(III) centre. Each complex was calculated *via* TDDFT/B3LYP/GENECP/LanL2DZ, using CH_2Cl_2 as the solvent, and working from the optimised ground state geometries.

Again, there are three main types of photophysical transition involved across the range of photophysical measurements described here: a vertical intraligand (IL) transition, a ligand-to-ligand charge transfer (L'LCT) and an intraligand charge transfer (ILCT). Where the ligand in question is the ancillary ligand, L is used to denote it, whereas L is used to denote the respective phen-pyrene fragment of each product. As the metal-centred (MC) excited states are too high in iridium to access, any metal involvement is in the form of a ligand-to-metal charge transfer (LMCT) or a metal-to-ligand charge transfer (MLCT).

The spin density surfaces of **Ir1** – **Ir4** were first calculated. These show the location of the T_1 state of each product by calculating the location of the unpaired spin within the molecule. The T_1 state of **Ir1** (Figure 3.11) is located mostly over one of the C6 auxiliary ligands, with only small contributions from the Ir(III) centre and the phenanthroline participating ligand. Given that the majority of the HOMO of this complex is also located on this C6 moiety (Figure 3.15) with some involvement of the pyrene moiety, the triplet excited state of **Ir1** is proposed to be ^{3}IL' in character. This is in agreement with the photophysical analysis of this compound (See discussion of figures 3.1 – 3.3).

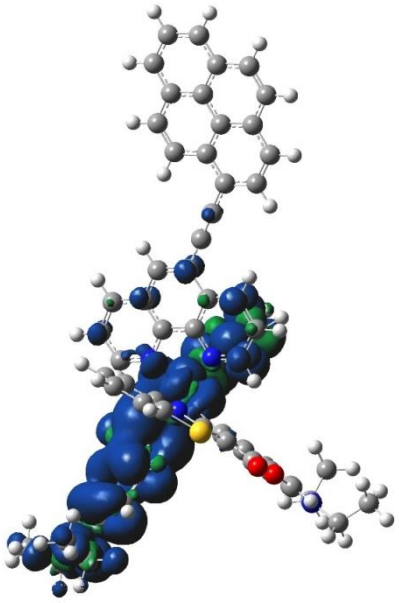

***Figure 3.11**: The isosurface of spin density of **Ir1** at the optimised triplet-state geometry.*

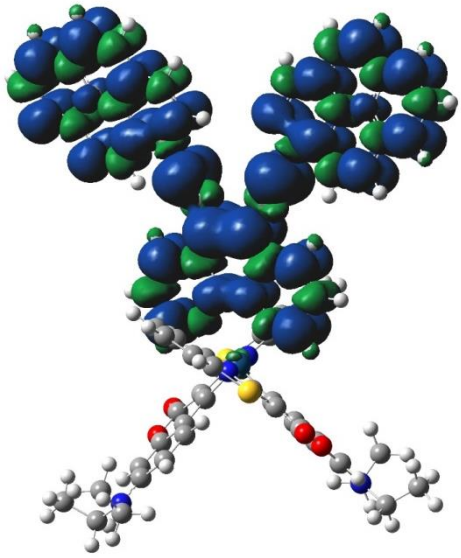

***Figure 3.12**: The isosurface of spin density of **Ir2** at the optimised triplet-state geometry.*

The T_1 states of **Ir2**, **Ir3** and **Ir4** are shown in Figures 3.11, 3.12 and 3.13 respectively. In each case, the triplet state is centred on the ethynylpyrene and phenanthroline moieties of the complex. The HOMO of each of these complexes (Figures 3.16, 3.17 and 3.18, respectively) is located around the same components of the compound, and so these states can be assigned ^{3}IL character. As the metal centre contribution to these T_1 states is very low, it can be expected that long triplet lifetimes may be measured for each of **Ir2** – **Ir4**.

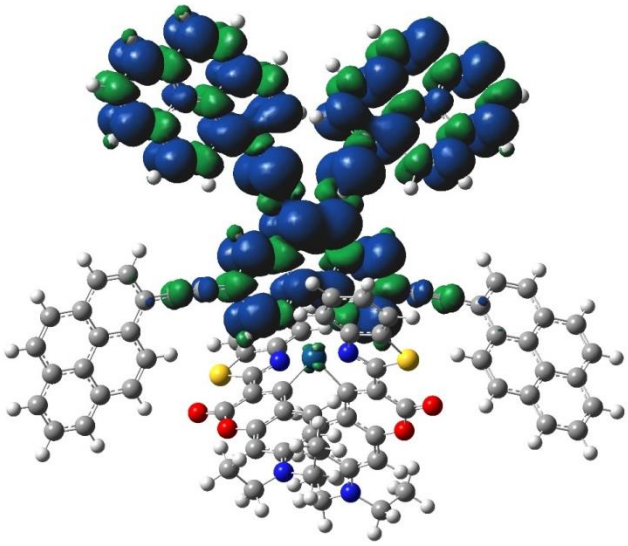

***Figure 3.13**: The isosurface of spin density of **Ir3** at the optimised triplet-state geometry.*

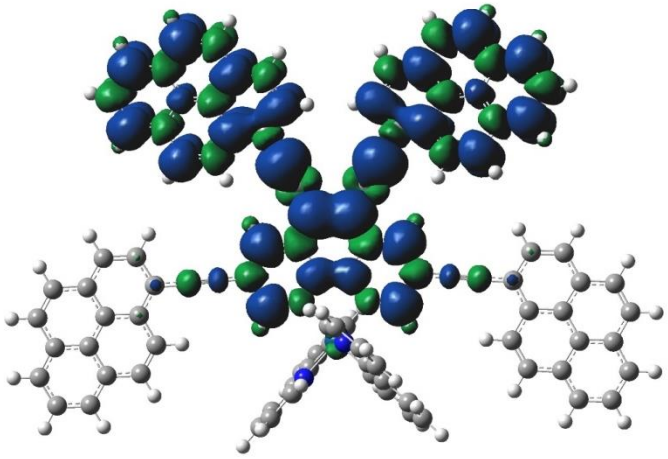

***Figure 3.14**: The isosurface of spin density of **Ir4** at the optimised triplet-state geometry.*

The TDDFT-derived data for compounds **Ir1** – **Ir4** given Tables 2.4 to 2.10 and Figures 3.15 to 3.18.

Table 3.3 shows the most significant calculation results of **Ir1**. The HOMO (Figure 3.15) of **Ir1** is mostly located on the C6 ligands and partly on the pyrene moiety, while the LUMO (Figure 3.15) is located entirely on the phen-pyrene fragment. The energy of the vertical excitation $S_0 \rightarrow S_1$ is 528 nm, however the oscillator strength (*f*) of this transition is very small ($f = 0.0405$). The main absorption bands of **Ir1** are in the region 430 nm to 485 nm, and the experimental absorption bands appear to align with the calculated values closely, as shown in Table 3.3. One of these absorptions appears to correlate to a faint shoulder seen in the experimental spectrum at approximately 430 nm. These absorptions are therefore assigned as before, as a C6-based IL' transition and a C6 to phen L'LCT.

***Table 3.3**: Comparison of the experimental and computational absorption values of **Ir1**.*

Experimental Value	Computational Value
485 nm, 2.556 eV	517.9 nm, 2.394 eV
460 nm, 2.695 eV	439.56 nm, 2.8206 eV
430 nm, 2.880 eV	435.53 nm, 2.8467 eV

***Table 3.4**: TDDFT calculation results for **Ir1**. Electronic excitation energies (eV), corresponding oscillator strengths (f), main configuration, and CI coefficients of the low-lying electronically excited states of **Ir1**.*

	Electronic Transition[a]	TDDFT//B3LYP/GENECP/LanL2DZ				
		Energy	f[b]	Composition[c]	CI[d]	Character
Singlet	$S_0 \rightarrow S_1$	2.3468 eV	0.0405	H-2 → L	0.22387	L'LCT
		528.32 nm		H-1 → L	0.61041	L'LCT
				H-1 → L+1	0.20993	L'LCT
				H → L	0.10789	L'LCT, IL
	$S_0 \rightarrow S_3$	2.394 eV	0.504	H-2 → L	0.60718	L'LCT
		517.9 nm		H-1 → L	0.26383	L'LCT
				H → L+1	0.19665	L'LCT, ILCT
	$S_0 \rightarrow S_9$	2.8206 eV	0.5875	H-3 → L+3	0.11018	IL'
		439.56 nm		H-2 → L+3	0.36394	LL'CT, IL'
				H-1 → L+2	0.318	IL', LL'CT
				H-1 → L+3	0.30357	IL', LL'CT
				H → L+2	0.31488	LL'CT, IL'
				H → L+3	0.21708	LL'CT, IL'
	$S_0 \rightarrow S_{10}$	2.8467 eV	1.2311	H-2 → L+2	0.27824	LL'CT, IL'
		435.53 nm		H-2 → L+3	0.1042	LL'CT, IL'
				H-1 → L+2	0.30674	IL', LL'CT
				H-1 → L+3	0.25324	IL', LL'CT
				H → L+2	0.13691	LL'CT, IL'
				H→ L+3	0.46529	LL'CT, IL'
Triplet	$S_0 \rightarrow T_1$	1.7053 eV	0	H-2 → L	0.40693	L'LCT
		727.07 nm		H-2 → L+3	0.11194	LL'CT, IL'
				H-2 → L+4	0.21741	IL, L'LCT

			H-1 → L	0.29694	L'LCT
			H-1 → L+4	0.15789	L'LCT, IL
			H → L	0.27183	L'LCT, IL
			H → L+4	0.14063	L'LCT, IL
$S_0 \rightarrow T_2$	2.1135 eV	0	H-2 → L	0.13904	L'LCT, IL
	586.64 nm		H-2 → L+2	0.26068	LL'CT, IL'
			H-2 → L+3	0.21584	LL'CT, IL'
			H-1 → L+2	0.12364	IL', LL'CT
			H → L	0.25576	L'LCT, IL
			H → L+2	0.27054	LL'CT, IL'
			H → L+3	0.42321	LL'CT, IL'
$S_0 \rightarrow T_3$	2.1189 eV	0	H-2 → L	0.11902	L'LCT
	585.13 nm		H-2 → L+2	0.15316	LL'CT, IL'
			H-2 → L+3	0.21631	LL'CT, IL'
			H-1 → L	0.15466	L'LCT
			H-1 → L+1	0.17618	L'LCT
			H-1 → L+2	0.42752	IL', LL'CT
			H-1 → L+3	0.30166	IL', LL'CT
			H → L+2	0.23318	LL'CT, IL'

[a] *Only selected significant excited states were considered.* [b] *Oscillator strength.* [c] *H stands for HOMO, L stands for LUMO, and only the main configurations are presented here.* [d] *The coefficient of the wavefunction for each excitation, given in absolute values.*

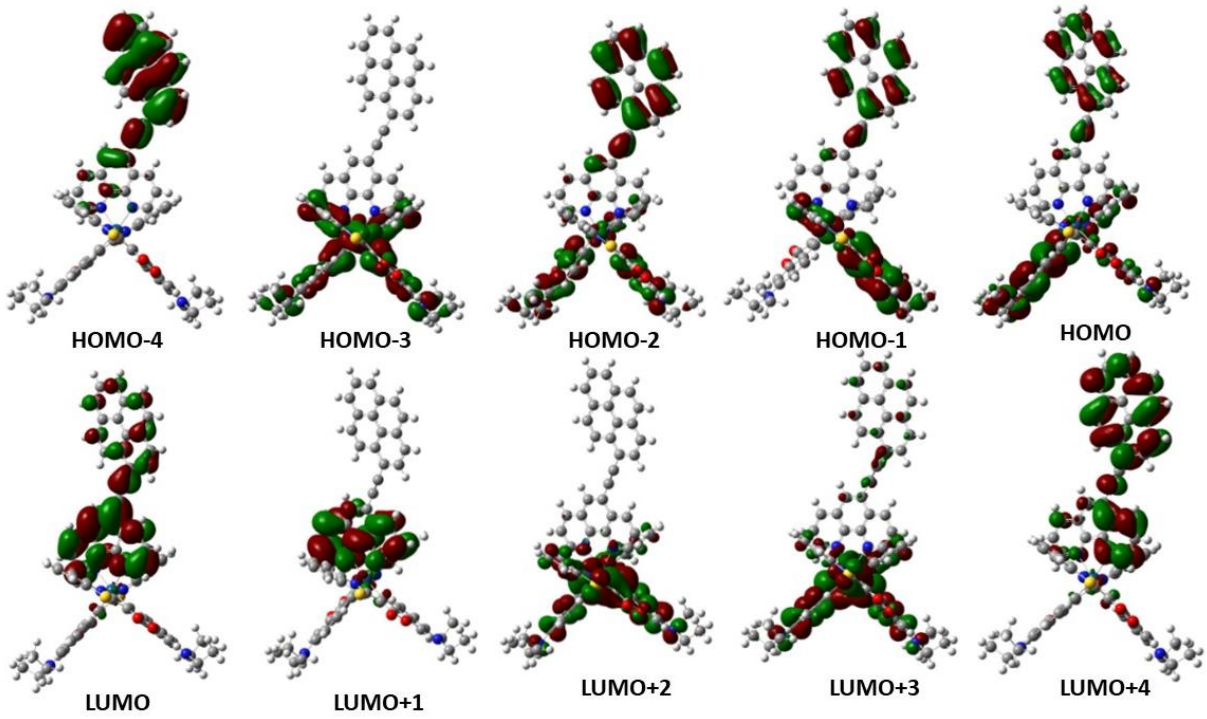

Figure 3.15*: The frontier molecular orbitals of note of* ***Ir1****.*

In the case of **Ir2**, the calculated and experimental values for the absorption bands of the complex are in close agreement, as shown in Table 3.5.

Table 3.5*: Comparison of the experimental and computational absorption values of* ***Ir2****.*

Experimental Value	Computational Value
480 nm, 2.583 eV	526.19 nm, 2.3563 eV
460 nm, 2.695 eV	441.31 nm, 2.8094 eV
430 nm, 2.880 eV	436.67 nm, 2.8393 eV

The energy of the vertical $S_0 \rightarrow S_1$ transition is 602 nm, larger than that of **Ir1** (Table 2.5, Figure 3.16), and in this case the oscillator strength is much higher (f = 0.7183). This however does not appear to correspond to an experimental absorption band, and may correspond to another band within the body of the main absorption band. In the literature, it states that TDDFT calculations frequently generate energies for excited states with relatively systematic errors, ranging in the region of 0.2 – 0.4 eV. Therefore, while it is

unfortunate that the calculations are not more accurate, it is not particularly concerning that this absorption band is not in the calculated region.[103]

***Table 3.6**: TDDFT calculation results for **Ir2**. Electronic excitation energies (eV), corresponding oscillator strengths (f), main configuration and CI coefficients of the low-lying electronically excited states of **Ir2**.*

	Electronic	**TDDFT//B3LYP/GENECP/LanL2DZ**				
	Transition[a]	Energy	*f*[b]	Composition[c]	CI[d]	Character
		2.0582 eV				
Singlet	$S_0 \rightarrow S_1$	602.4 nm	0.7183	H → L	0.70408	ILCT
		2.3563 eV				
	$S_0 \rightarrow S_5$	526.19 nm	0.2671	H-3 → L	0.1619	ILCT
				H → L+1	0.1635	ILCT
	$S_0 \rightarrow S_{11}$	2.8094 eV	0.7412	H-4 → L+3	0.11129	IL
		441.31 nm		H-2 → L+3	0.48472	IL
				H-1 → L+2	0.47978	IL
	$S_0 \rightarrow S_{14}$	2.8393 eV	1.1888	H-2 → L+2	0.44639	IL
		436.67 nm		H-1 → L+3	0.48986	IL
				H → L+3	0.2109	LL'CT
						ILCT,
Triplet	$S_0 \rightarrow T_1$	1.4889 eV	0	H-10 → L	0.1024	L'LCT
		832.7 nm		H-5 → L	0.13806	ILCT
				H-3 → L+4	0.1806	IL
				H → L	0.63252	ILCT
				H → L+5	0.12055	IL, ILCT
	$S_0 \rightarrow T_2$	1.8175 eV	0	H-3 → L	0.49442	ILCT
		682.17 nm		H-3 → L+5	0.24645	IL, ILCT
				H → L+4	0.38686	IL
		2.0582 eV				
	$S_0 \rightarrow T_3$	602.4 nm	0	H → L	0.70409	ILCT

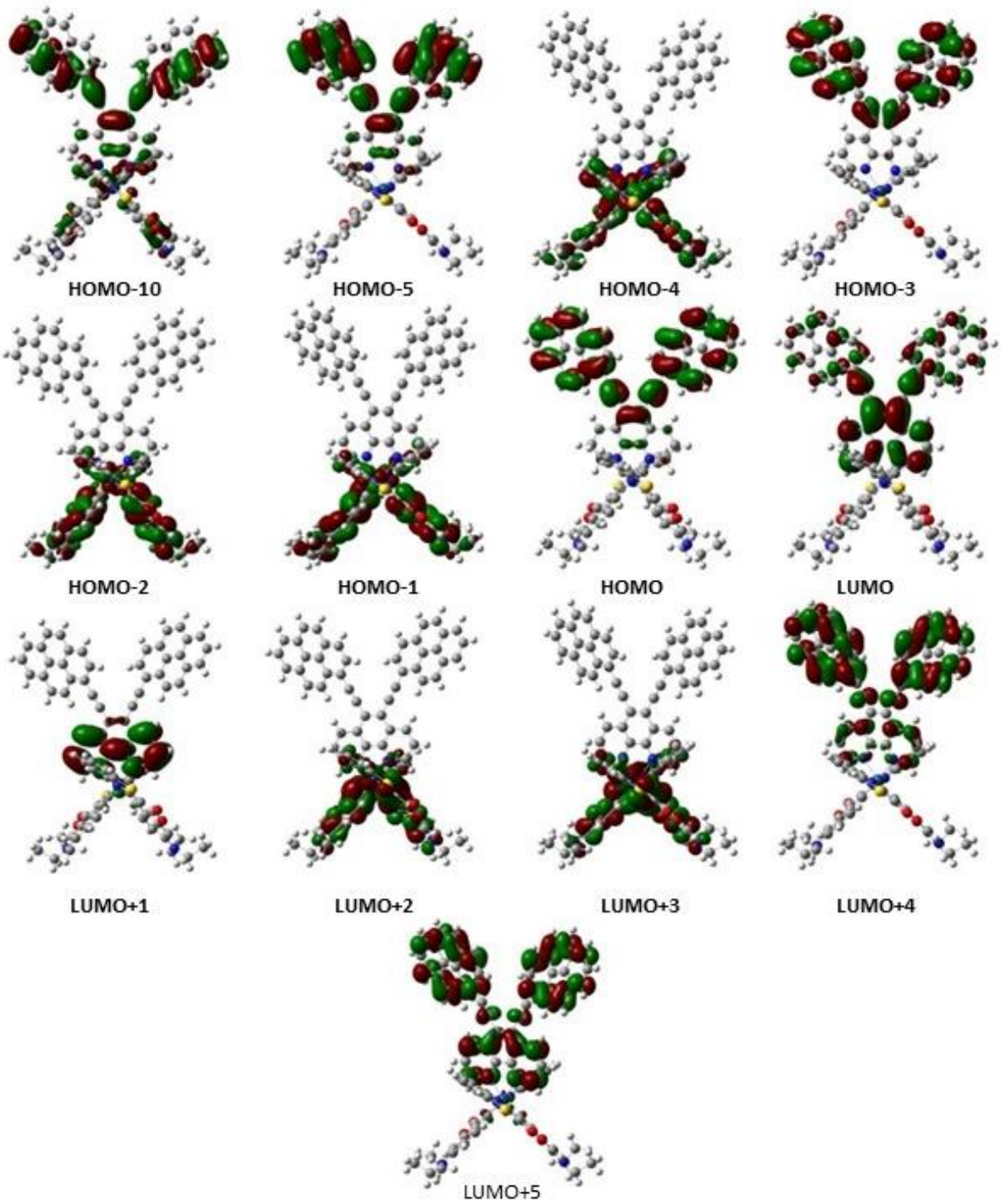

***Figure 3.16**: The frontier molecular orbitals of note of **Ir2**.*

As there are no experimental values for **Ir3**, its computational data is presented here without empirical comparison (Figure 3.17). The calculated $S_0 \rightarrow S_1$ transition has a particularly small *f* value of 0.0775, and the absorption profile appears to be dominated by two particularly strong transitions, shown in Table 3.7. **Ir3** cannot be accurately compared to **Ir4** as, while the participating ligand is the same in each, the vast difference

in absorption properties between C6 and ppy auxiliary ligands means that **Ir3** will be expected to have a vastly higher absorption intensity.

***Table 3.7**: TDDFT calculation results for **Ir3**. Electronic excitation energies (eV), corresponding oscillator strengths (f), main configuration and CI coefficients of the low-lying electronically excited states of **Ir3**.*

	Electronic	**TDDFT//B3LYP/GENECP/LanL2DZ**				
	Transition[a]	Energy	f[b]	Composition[c]	CI[d]	Character
		1.9895 eV				
Singlet	$S_0 \rightarrow S_1$	623.21 nm	0.0775	H → L	0.69976	ILCT
	$S_0 \rightarrow S_3$	2.0909 eV	1.5	H-3 → L	0.17218	L'LCT
		592.96 nm		H-1 → L	0.63834	ILCT
				H → L+1	0.22931	ILCT
	$S_0 \rightarrow S_{20}$	2.8316 eV	1.0754	H-6 → L	0.14279	L'LCT
		437.86 nm		H-3 → L+2	0.46059	IL
				H-3 → L+3	0.12197	IL
				H-2 → L+3	0.46224	IL
						ILCT,
Triplet	$S_1 \rightarrow T_1$	1.4709 eV	0	H-14 → L+1	0.10084	L'LCT
		842.91 nm		H-7 → L+1	0.13745	ILCT
				H-5 → L+5	0.15122	IL
				H-1 → L	0.14559	ILCT
				H → L+1	0.60834	ILCT
				H → L+6	0.10079	IL
	$S_0 \rightarrow T_2$	1.6643 eV	0	H-4 → L+4	0.26244	IL
		744.98 nm		H-1 → L	0.55877	ILCT
				H-1 → L+7	0.16992	IL, ILCT
				H → L+1	0.15226	ILCT
	$S_0 \rightarrow T_3$	1.7563 eV	0	H-4 → L	0.46098	ILCT
		705.92 nm		H-4 → L+7	0.2142	IL, ILCT
				H-1 → L+3	0.10053	LL'CT
				H-1 → L+4	0.34942	IL
				H → L	0.2375	ILCT

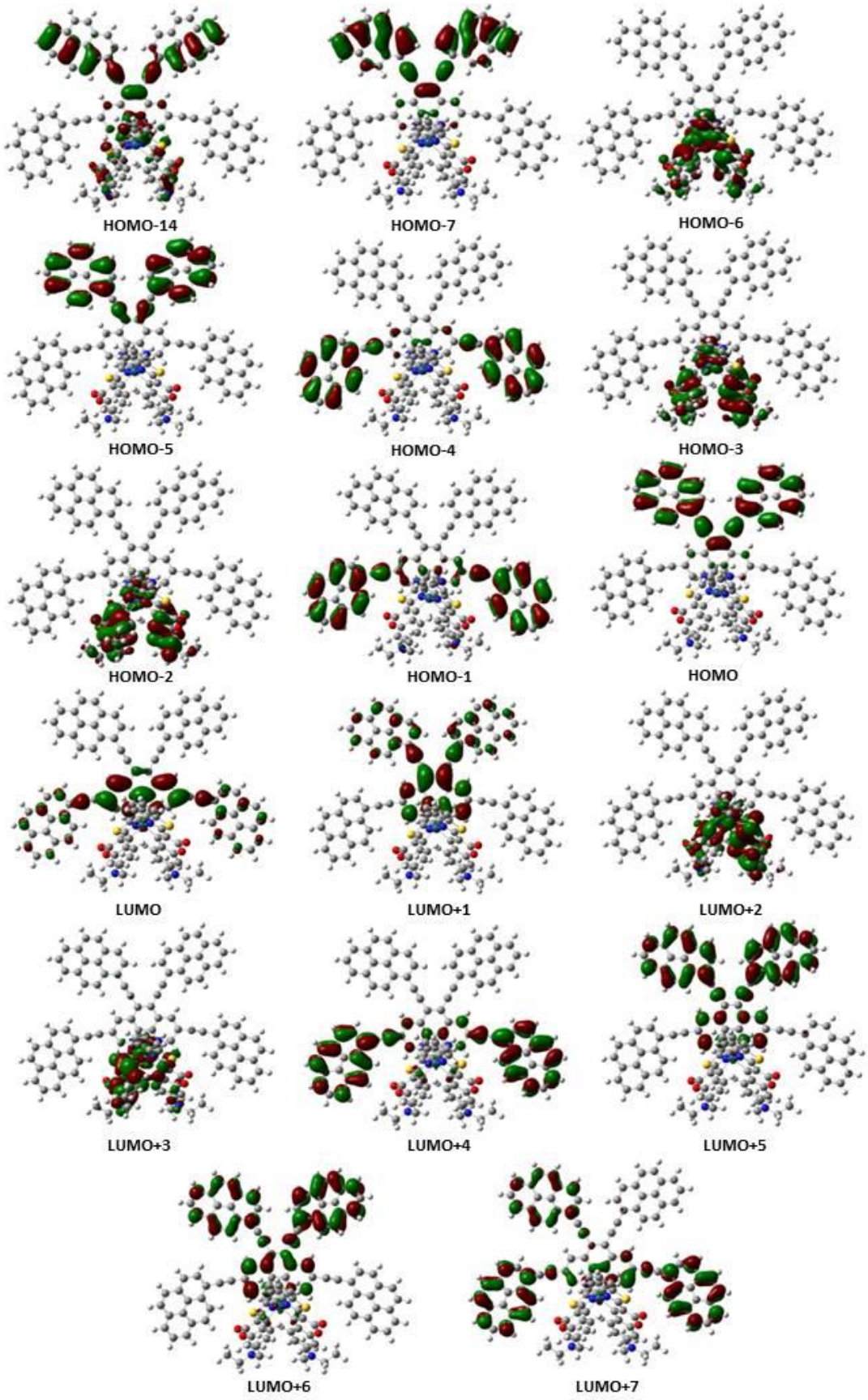

***Figure 3.17**: The frontier molecular orbitals of note of **Ir3**.*

The TDDFT results of **Ir4** are presented here (Table 3.9, Figure 3.18). The centre of the broad emission of **Ir4** in MeCN is 450 nm in the UV-visible spectrum, which corresponds to 2.755 eV (Table 3.8). As **Ir4** appears to be slightly affected by solvatochromism, in CH_2Cl_2 there are two shoulders which make up the peak, at 470 nm (2.638 eV) and 495 nm (2.50 eV). In the other three solvents, the broad peak is centred at 460 nm (2.695 eV). Due to the broadness of the peak, all of these values may correspond, within the margin of error,[103] to the calculated values given by the TDDFT calculations.

***Table 3.8**: Comparison of the experimental and computational absorption values of **Ir4**.*

Experimental Value	**Computational Value**
450 nm, 2.755 eV	577.63 nm, 2.1464 eV
	529.23 nm, 2.3427 eV

***Table 3.9**: TDDFT calculation results for **Ir4**. Electronic excitation energies (eV), corresponding oscillator strengths (f), main configuration and CI coefficients of the low-lying electronically excited states of **Ir4**.*

	Electronic	**TDDFT//B3LYP/GENECP/LanL2DZ**				
	Transition[a]	Energy	*f*[b]	Composition[c]	CI[d]	Character
		2.0245 eV				
Singlet	$S_0 \rightarrow S_1$	612.43 nm	0.08	H → L	0.69903	ILCT
	$S_0 \rightarrow S_3$	2.1464 eV	2.0823	H-1 → L	0.66447	ILCT
		577.63 nm		H → L+1	0.20807	IL, ILCT
	$S_0 \rightarrow S_6$	2.3427 eV	0.2576	H-4 → L	0.11397	ILCT
		529.23 nm		H-3 → L+1	0.34976	ILCT
				H-2 → L	0.57003	ILCT
				H-1 → L+1	0.16349	ILCT
Triplet	$S_0 \rightarrow T_1$	1.4803 eV	0	H-6 → L+1	0.13767	IL, ILCT
		837.57 nm		H-3 → L+3	0.1599	IL
				H-1 → L	0.17326	ILCT
				H → L+1	0.6042	IL, ILCT
				H → L+4	0.10599	IL
	$S_0 \rightarrow T_2$	1.6621 eV	0	H-2 → L+2	0.27746	IL

	745.95 nm		H-1 → L	0.5562	ILCT
			H-1 → L+5	0.16799	IL, ILCT
			H → L+1	0.17921	IL, ILCT
$S_0 \rightarrow T_3$	1.7622 eV	0	H-2 → L	0.45971	ILCT
	703.59 nm		H-2 → L+5	0.21854	IL, ILCT
			H-1 → L+2	0.38259	IL
			H → L	0.21966	ILCT

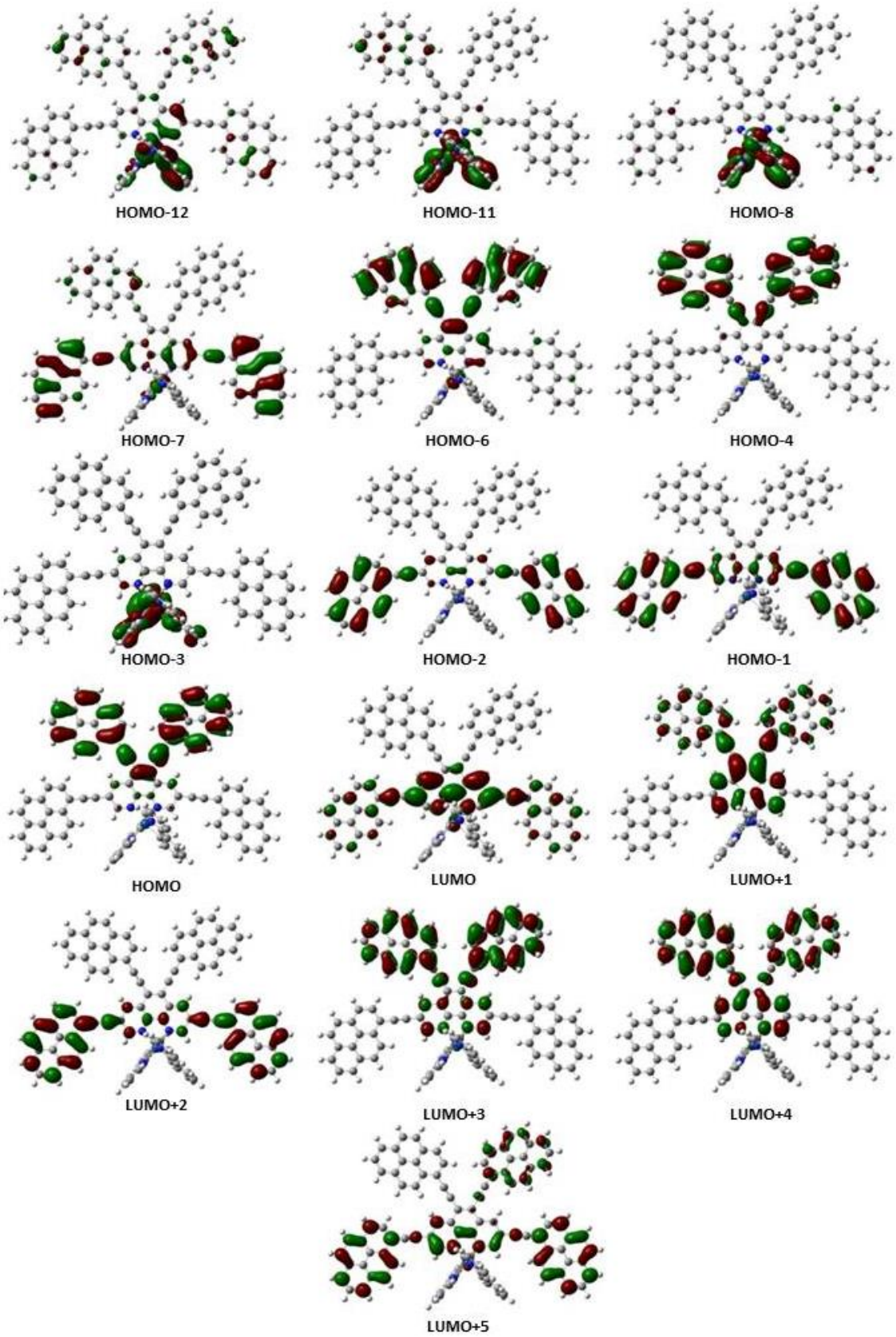

Figure 3.18*: The frontier molecular orbitals of note of* ***Ir4****.*

3.4 Conclusions

A series of cyclometalated Ir(III) complexes with coumarin-6 (**Ir1**, **Ir2** and **Ir3**) and ppy (**Ir4**) ancillary ligands were successfully synthesised and investigated. **Ir3** was found to be unstable – possibly photosensitive - and only minute amounts could be synthesised in high purity. The complexes were found to have strong visible-region absorption, particularly those utilising the coumarin-6 ligands. Meanwhile, they were found to have maintained their high triplet energy levels as their triplet-based emission bands were in the region 650 – 680 nm. The triplet character of these emission spectra was confirmed with low-temperature emission, which also confirmed the ^{3}IL and ^{3}ILCT nature of the emissions.

In the case of **Ir1**, further photophysical measurements were carried out. The transient absorption spectrum of **Ir1** again confirmed the long-lived triplet nature of the excited state. The phosphorescence lifetime (262.6 μs), singlet oxygen sensitisation quantum yield (Φ_Δ = 76.6 %), triplet quenching constant (K_{SV} = 2.65 x 10^6 M^{-1}), and upconversion quantum yield (Φ_{UC} = 23.9 %) were calculated and found to be promisingly high for TTA-UC uses, and even comparable to those of analogous complexes previously published.[25, 28] However, it is concluded that an analogous complex, **X1**, is both simpler to synthesise and higher yielding, as well as showing stronger upconversion properties.

Further photophysical study of the remaining complexes, **Ir2** and **Ir4**, should be carried out in the immediate future.

Chapter 4

Photophysical Investigations into Dinuclear Ir(III) Triplet Photosensitising Molecules

4.1 Photophysical Studies of Ir5 and Ir6

Various photophysical measurements were carried out for **Ir5** and **Ir6**. These included UV-vis absorption spectroscopy, emission spectroscopy (under air and Ar), and emission spectra (RT and 77 K). The analysis of the data obtained from these tests can be used to give preliminary assignments of the most significant excited states of each complex. This will be done in order to give an indication for their usefulness as triplet photosensitisers, and the priority with which further photophysical measurements should be carried out.

The complexes in this chapter will be directly compared to their mononuclear analogues, **X2** and **X3** (Figure 4.1).

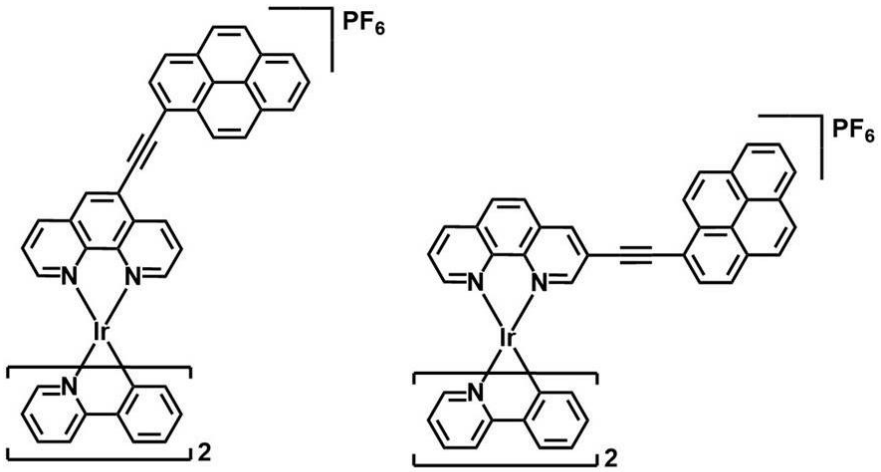

X2 **X3**

***Figure 4.1**: The structures of the mononuclear analogues to **Ir5** (**X3**) and **Ir6** (**X2**).*

There are three main types of photophysical transition involved across the range of photophysical measurements described here. The first is an intraligand (IL) transition (which is sometimes referred to as ligand-centred (LC)) which is a vertical transition on one moiety or area; the second is an intraligand charge transfer (ILCT) which involves the transfer of charge from one area of a ligand to another area of the same ligand; the third is a ligand-to-ligand charge transfer (L'LCT). Where the ligand in question is the ancillary ligand, L' is used to denote it, whereas L is used to denote the respective phen-pyrene fragment of each product. As the metal-centred (MC) excited states are too high in

iridium to access due to the usually very high ligand field splitting,[51] any metal involvement would be in the form of a ligand-to-metal charge transfer (LMCT) or a metal-to-ligand charge transfer (MLCT).

4.1.1 Steady-State UV-Vis Absorption Spectra of Ir5 and Ir6

The room temperature UV-vis absorption spectra of **Ir5** and **Ir6** were measured in five solvents of increasing polarity (toluene, CH_2Cl_2, MeCN, EtOH, and MeOH), and are presented in Figure 4.2.

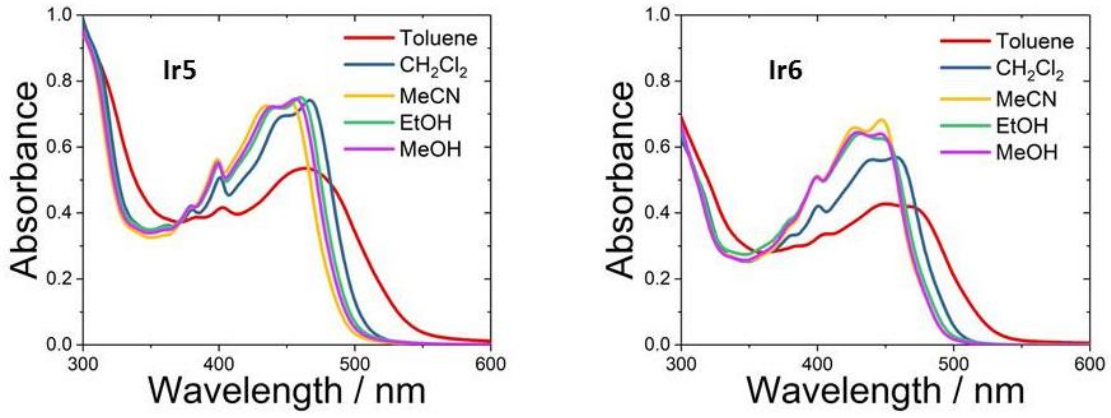

***Figure 4.2**: Absorption spectra of **Ir5** and **Ir6** in five different solvents (toluene, CH_2Cl_2, MeCN, EtOH, MeOH), c = 1 x 10^{-5} M, RT.*

The structure of the absorption profiles of **Ir5** and **Ir6** are very similar. Both complexes show lower-intensity and red-shifted absorption in some solvents, particularly toluene. The lower intensity is ascribed to the lower solubility of the complexes in low-polarity solvents, but the red-shift of the peak maxima indicates that the ground state of each complex may be mildly stabilised by solvent polarity. The main absorption bands in the visible region, between 400 – 500 nm (Table 4.1), are largely the result of ^{1}IL and ^{1}ILCT absorptions, within the core fragment itself. These transitions will be further explored *via* TDDFT results.

In comparison to their mononuclear analogues, **Ir5** and **Ir6** have significantly higher molar absorption coefficients than **X3** or **X2**,[25] respectively. **Ir5** has a value of ε = 7.35 x 10^{-4} at 455 nm, while its counterpart **X3** has just ε = 3.07 x 10^{-4} at 440 nm. Similarly, **Ir6** has a value of ε = 6.82 x 10^{-4} at 448 nm, whereas **X2** has a value of only ε = 2.86 x 10^{-4} at 434 nm. The absorption increase – more than double in each case – is as a direct result of the inclusion of the second metal centre which increases the number of transitions available within the phen-pyrene core. However, there appears to have been only a minor

red-shift of the absorption bands in each case, meaning that this appears to be an inefficient method by which to tune the absorption wavelength.

***Table 4.1**: The wavelength (λ_{max}) and molar absorptivity coefficient (ε) values of **Ir5** and **Ir6** in MeCN.*

Ir5		**Ir6**	
λ_{max} (nm)	***ε (M^{-1} cm^{-1})***	***λ_{max} (nm)***	***ε (M^{-1} cm^{-1})***
455	7.35×10^{-4}	448	6.82×10^{-4}
435	7.24×10^{-4}	426	6.57×10^{-4}
400	5.53×10^{-4}	400	5.09×10^{-4}

4.1.2 Emission Spectra of Ir5 and Ir6

The emission spectra of **Ir5** and **Ir6** were studied as solutions in air and degassed under Ar in MeCN (1×10^{-5} M, Figure 4.3). In each case, the emission is completely quenched in air, confirming the expected phosphorescent character of the emission. The emission of each sample consists of one large emission band, with a peak of λ_{em} = 725 nm in **Ir5** and λ_{em} = 730 nm in **Ir6**. There is no significant emission outside this low-energy band, and the shoulder exhibited by both complexes, clear in **Ir5** at 747 nm. The two complexes show a similarly structured emission, and TDDFT results (Fig. 3.9 and Fig. 3.10) show that both complexes have their first triplet excited state, T_1, located on the central pyrene moiety and the adjacent phen moieties. As the HOMO of **Ir5** and **Ir6** is located on the central phen-pyrene fragment (Figs. 4.9 and 4.10, respectively), the emission here is tentatively assigned as being ^{3}IL in nature.

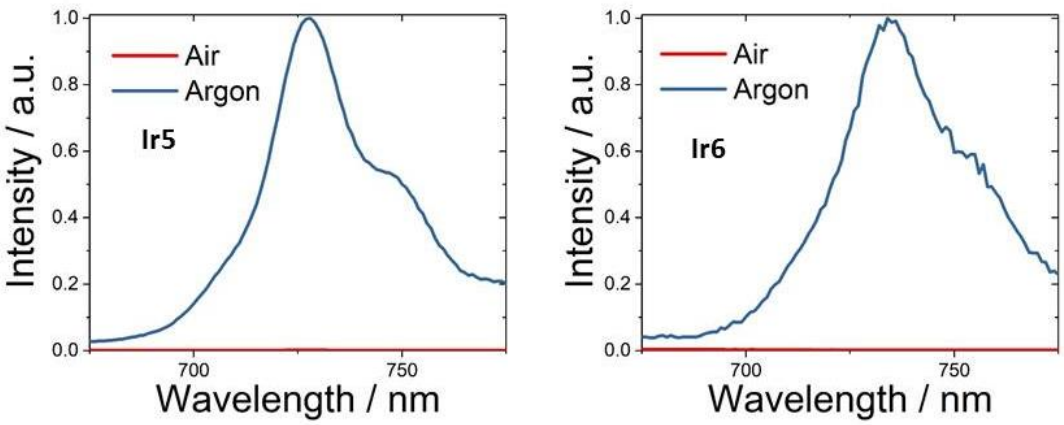

***Figure 4.3**: Emission spectra of **Ir5** and **Ir6** measured in air and under Ar, in MeCN, λ_{ex} = 440 nm.*

In comparison, the emission spectra[25] of **X3** and **X2** have a broadly similar structure, but **Ir5** and **Ir6** have peak maxima which are significantly red-shifted in comparison to their mononuclear analogues. Comparing **Ir5** to **X3**, the peak maxima are at 725 nm and 672 nm respectively. For **Ir6** and **X2**, the peak maxima are located at 730 nm and 678 nm, respectively. This shows that in the dinuclear complexes, the energy of the T_1 level has been only slightly reduced.

Figure 4.4 shows the normalised emission spectra of **Ir5** and **Ir6** at both RT under Ar, and at 77K. In the cases of both **Ir5** and **Ir6**, there is no significant difference in the maximum λ_{em} between RT and 77K. The lack of a significant Stokes shift at low temperature again strongly supports the assignment of the emissive state in both complexes as ^{3}IL.[50, 100] These spectra are again similar to their mononuclear analogues, **X2** and **X3**, which also showed small blue-shifts at low temperature and were determined to have ^{3}IL excited states.[25]

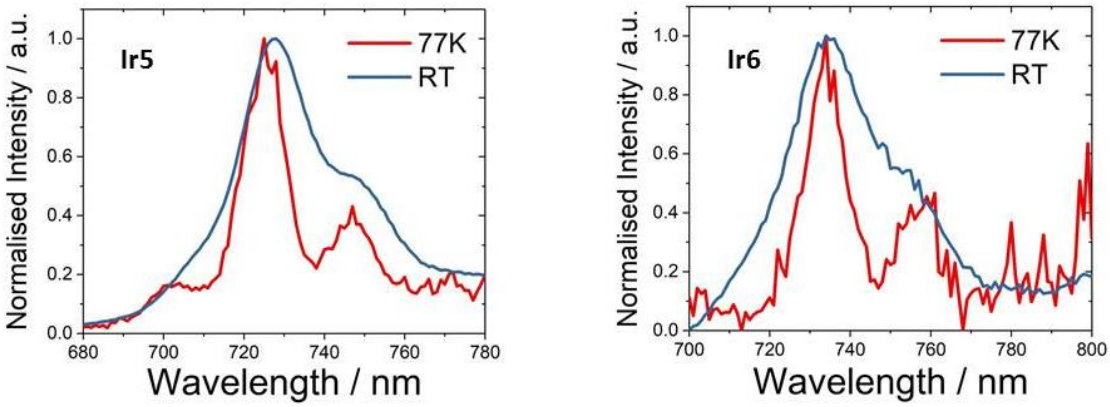

***Figure 4.4**: Emission spectra of **Ir5** and **Ir6** measured at 77K and at room temperature (under Ar), λ_{ex} = 440 nm.*

These assignments will be further tested by the measurement of properties such as triplet phosphorescence lifetimes, TDDFT calculations, and transient absorption studies.

4.2 Cyclic Voltammetry Studies of Ir5 and Ir6

Cyclic voltammetry (CV) studies were carried out on 1 x 10^{-4} solutions of **Ir5** and **Ir6** in CH_2Cl_2 (with 0.1 M nBu_4NPF_6). The cyclic voltammograms were recorded using a glassy carbon working electrode, a Ag/AgCl reference electrode, and a Pt wire counter electrode.

As in Chapter 3, the oxidative wave of each sample appears to be outside the solvent window of CH_2Cl_2. This is not standard for mononuclear or multinuclear iridium complexes.[60, 102] However, the reduction of **Ir5** and **Ir6** generated voltammograms. Each voltammogram was initially run between 0 and -2.5 V, followed by a narrower window (-2 V) in order to avoid issues with solvent reduction processes that may occur close to the window edge. Table 4.2 shows the values of the reduction voltammograms of **Ir5** and **Ir6**.

The reduction voltammogram of **Ir5** is shown in Figure 4.5. There is one clearly identifiable reduction peak at E_{pc} = -1.15 V, which is found to be irreversible. This is tentatively assigned as the reduction of the phen-pyrene fragment as this is where the LUMO of **Ir5** is located according to TDDFT results (Figure 4.9).

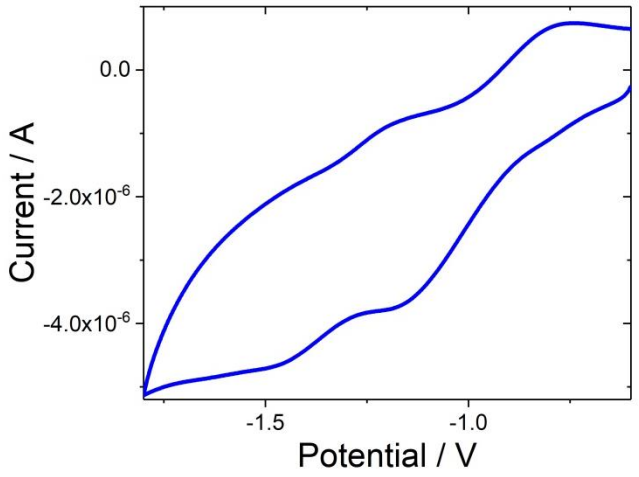

***Figure 4.5**: The reductive cyclic voltammogram of **Ir5**. (CH_2Cl_2, 0.1 M $TBAPF_6$, scan rate = 0.1 V/s)*

Figure 4.6 in turn shows the reduction voltammogram of **Ir6**. The reduction peak at E_{pc} = -1.21 V is again calculated as irreversible, and is also tentatively assigned as being the reduction of the extended phen-pyrene fragment as this is where the LUMO of **Ir6** is located (Figure 4.10).

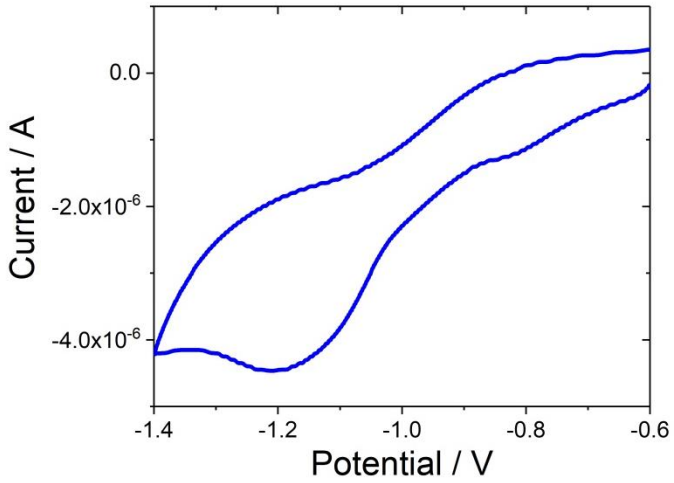

***Figure 4.6**: The reductive cyclic voltammogram of **Ir6**. (CH_2Cl_2, 0.1 M $TBAPF_6$, scan rate = 0.1 V/s)*

***Table 4.2**: The cyclic voltammetry results of **Ir5** and **Ir6**.*

Complex	Reduction (E_{pc}/V)
Ir5	-1.15
Ir6	-1.21

4.3 Density Functional Theory Calculations of Ir5 and Ir6

Time-dependent density functional theory (TDDFT) calculations were carried out in Dalian University of Technology in order to further understand the nature of the excited states of the iridium products.

The ground-state geometry of each complex was first determined. These geometries represent the lowest-energy arrangements possible, and are used to calculate the energy of each orbital. In each case the central pyrene fragment takes a coplanar orientation to that of the phen fragments, creating a large, extended aromatic framework. The ppy ligands on the Ir(III) centres form a standard octahedral geometry. Each complex was calculated *via* TDDFT/B3LYP/GENECP/LanL2DZ, using CH_2Cl_2 as the solvent, and working from the optimised ground state geometries.

The spin density surfaces of **Ir5** and **Ir6** were first calculated. These show the location of the T_1 state of each product. The T_1 state of **Ir5** (Figure 4.7) is located mostly over the extended phen-pyrene-phen fragment. There are only minute contributions from the Ir(III) centres. As the HOMO of **Ir5** is located almost entirely on the pyrene moiety (Fig. 4.9), the T_1 state is proposed to be mostly due to a vertical ^{3}IL transition, with some ^{3}ILCT character as well. This is in agreement with the initial photophysical analysis of this compound.

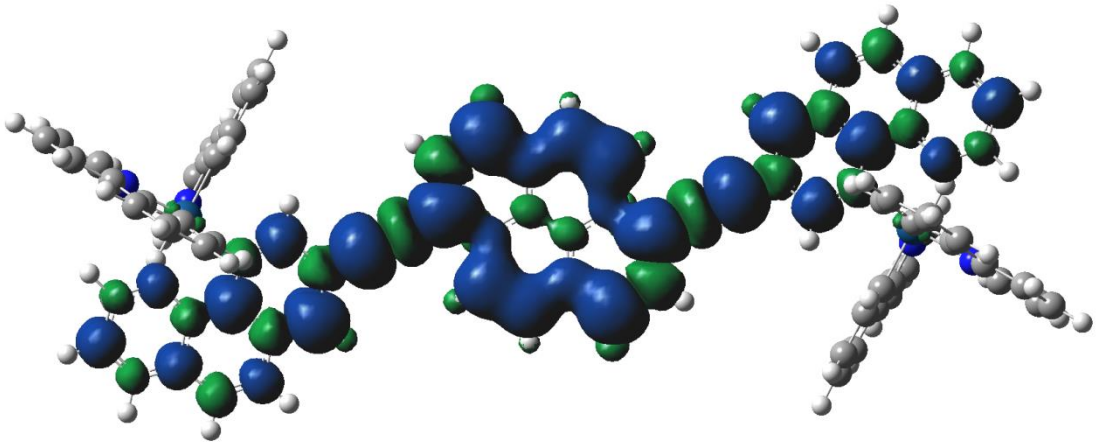

Figure 4.7*: The isosurface of spin density of* ***Ir5*** *at the optimised triplet-state geometry.*

The T_1 state of **Ir6** (Figure 4.8) is also located mostly over the extended phen-pyrene-phen fragment, and is almost identical to that of **Ir5**. There are again only minute contributions from the Ir(III) centres. The HOMO of **Ir6** is located almost entirely on the

pyrene moiety (Fig. 4.10), and so again the T_1 state is proposed to be mostly ^{3}IL in character, with a minority ^{3}ILCT character. This is also in agreement with the photophysical analysis of this compound.

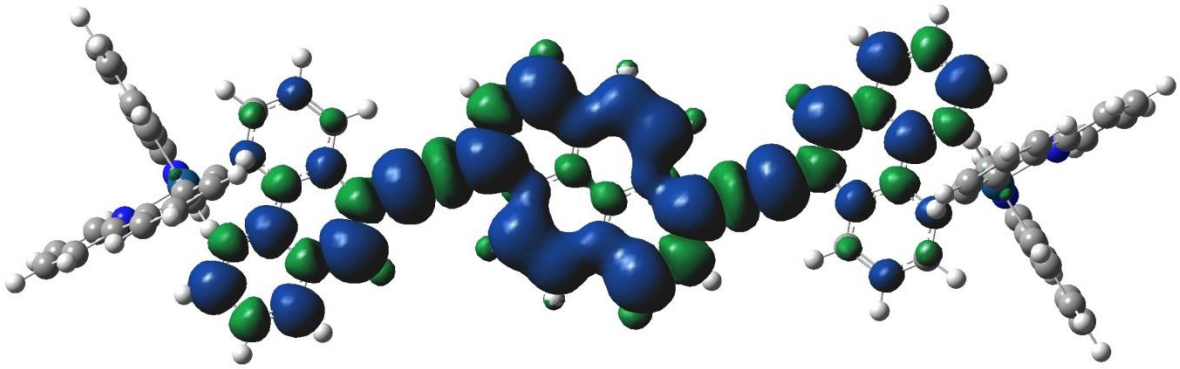

***Figure 4.8**: The isosurface of spin density of **Ir6** at the optimised triplet-state geometry.*

The TDDFT results of **Ir5** and **Ir6** are laid out in Tables 4.3 – 4.6, and the frontier molecular orbital diagrams (Figures 4.9 and 4.10).

Table 4.3 compares the TDDFT-calculated absorption bands of **Ir5** to those experimentally recorded. The HOMO is mostly located on the pyrene fragment, while the LUMO exists largely on the phen fragments but also occupies significant space on the pyrene. The energy of the vertical excitation $S_0 \rightarrow S_1$ is calculated as 577.26 nm (2.1478 eV), with an oscillator strength of f = 0.6369. This indicates that this transition should be visible on the UV-vis spectrum, however there is only a small intensity of absorption in this region. It may be that the $S_0 \rightarrow S_1$ and $S_0 \rightarrow S_3$ transitions may have higher-energy absorption bands slightly outside the common error range (0.2 to 0.4 eV[103]), and they may in fact make up the bulk of the broad absorption observed for **Ir5**. The calculations indicate that the contributions to the absorption bands are split between ^{1}IL and ^{1}ILCT transitions. The experimental contributions of the L'LCT transitions are negligible due to the lack of significant visible light absorption of ppy ligands. Further photophysical measurements may elucidate the cause for the discrepancy between the calculated and observed absorption values.

***Table 4.3**: Comparison of the experimental and computational absorption values of **Ir5**.*

Experimental Value	Computational Value
455 nm, 2.7249 eV	577.26 nm, 2.1478 eV

435 nm, 2.8502 eV	570.26 nm, 2.1738 eV
400 nm, 3.0996 eV	470.48 nm, 2.6352 eV
	468.73 nm, 2.6451 eV

***Table 4.4**: TDDFT calculation results for **Ir5**. Electronic excitation energies (eV), corresponding oscillator strengths (f), main configuration and CI coefficients of the low-lying electronically excited states of **Ir5**.*

	Electronic Transition[a]	**TDDFT//B3LYP/GENECP/LanL2DZ**				
		Energy	f[b]	Composition[c]	CI[d]	Character
Singlet	$S_0 \rightarrow S_1$	2.1478 eV	0.6369	H-2 → L	0.42667	L'LCT
		577.26 nm		H-1 → L+1	0.31402	L'LCT, L'MCT
				H → L	0.455	ILCT, IL
	$S_0 \rightarrow S_3$	2.1738 eV	1.0746	H-2 → L	0.38778	L'LCT
		570.37 nm		H-1 → L+1	0.22652	L'LCT, L'MCT
				H → L	0.52952	ILCT, IL
	$S_0 \rightarrow S_9$	2.6352 eV	0.0223	H-2 → L	0.30762	L'LCT
		470.48 nm		H-1 → L+1	0.43231	L'LCT, L'MCT
				H → L+2	0.44795	ILCT
	$S_0 \rightarrow S_{11}$	2.6451 eV	0.0302	H-2 → L	0.23935	L'LCT
		468.73 nm		H-2 → L+2	0.21170	L'LCT
				H-1 → L+1	0.34866	L'LCT, L'MCT
				H-1 → L+3	0.18647	L'LCT
				H → L+2	0.47997	ILCT

Triplet	$S_0 \rightarrow T_1$	1.5286 eV 811.10 nm	0	H → L	0.61597	ILCT, IL
				H → L+4	0.29177	IL, ILCT
	$S_0 \rightarrow T_2$	2.0370 eV 608.65 nm	0	H-12 → L	0.13403	ILCT, IL
				H-10 → L	0.20716	IL, L'LCT
				H-2 → L+1	0.11429	L'LCT, L'MCT
				H-1 → L	0.21679	L'LCT
				H → L+1	0.56067	ILCT, LMCT
	$S_0 \rightarrow T_3$	2.1116 eV 587.16 nm	0	H-2 → L	0.5468	L'LCT
				H-2 → L+4	0.10129	L'LCT
				H-1 → L+1	0.40027	L'LCT, L'MCT

[a] Only selected significant excited states were considered. [b] Oscillator strength. [c] H stands for HOMO, L stands for LUMO, and only the main configurations are presented here. [d] The coefficient of the wavefunction for each excitation, given in absolute values.

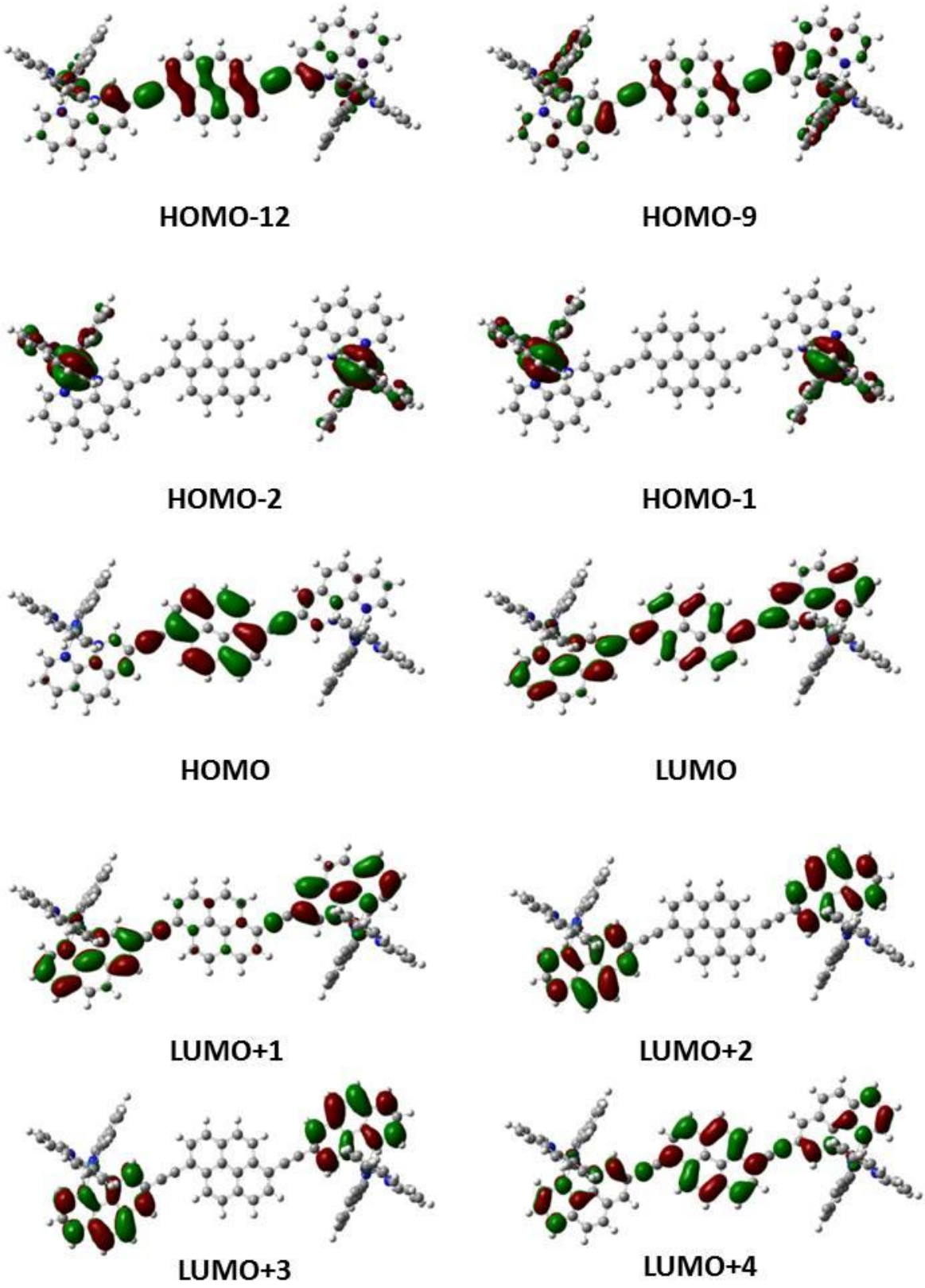

Figure 4.9*: The frontier molecular orbitals of note of* ***Ir5****.*

Table 4.5 compares the experimentally observed absorption bands and the TDDFT-derived absorption bands of **Ir6**. There is a discrepancy too between the computed and experimentally observed absorption band values. Again, the most significant transitions are IL and ILCT in nature as the ppy ligands do not contribute significantly to L'LCT transitions in empirical measurements.

Table 4.5*: Comparison of the experimental and computational absorption values of* ***Ir6****.*

Experimental Value	**Computational Value**
448 nm, 2.7675 eV	554.87 nm, 2.2345 eV
426 nm, 2.9104 eV	550.81 nm, 2.2510 eV
400 nm, 3.0996 eV	497.63 nm, 2.4915 eV

Table 4.6*: TDDFT calculation results for* ***Ir6****. Electronic excitation energies (eV), corresponding oscillator strengths (f), main configuration and CI coefficients of the low-lying electronically excited states of* ***Ir6****.*

	Electronic Transition[a]	**TDDFT//B3LYP/GENECP/LanL2DZ**				
		Energy	*f*[b]	Composition[c]	CI[d]	Character
Singlet	$S_0 \rightarrow S_1$	2.2345 eV 554.87 nm	0.8556	H-2 → L	0.29893	L'LCT
				H-2 → L+2	0.2534	L'LCT, L'MCT
				H-1 → L+1	0.29784	L'LCT, L'MCT
				H-1 → L+3	0.12831	L'LCT
				H → L	0.46331	IL, ILCT
	$S_0 \rightarrow S_3$	2.2510 eV 550.81 nm	0.8667	H-2 → L	0.39672	L'LCT
				H-2 → L+2	0.10449	L'LCT, L'MCT
				H-1 → L+1	0.25733	L'LCT,

						L'MCT
				H → L	0.49033	IL, ILCT
	$S_0 \rightarrow S_9$	2.4915 eV 497.63 nm	0.0645	H → L+2	0.68215	ILCT, LMCT
Triplet	$S_0 \rightarrow T_1$	1.5069 eV 822.8 nm	0	H → L	0.62908	IL, ILCT
				H → L+4	0.24643	IL, ILCT
	$S_0 \rightarrow T_2$	2.0025 eV 619.15 nm	0	H-12 → L	0.18187	IL, L'LCT
				H-9 → L	0.27033	IL, L'LCT
				H → L+1	0.43932	ILCT
				H → L+3	0.3215	ILCT, LMCT
	$S_0 \rightarrow T_3$	2.1976 eV 564.17 nm	0	H-2 → L	0.1883	L'LCT
				H-2 → L+3	0.43143	L'LCT, L'MCT
				H-1 → L	0.33478	L'LCT
				H-1 → L+3	0.30983	L'LCT

[a] Only selected significant excited states were considered. [b] Oscillator strength. [c] H stands for HOMO, L stands for LUMO, and only the main configurations are presented here. [d] The coefficient of the wavefunction for each excitation, given in absolute values.

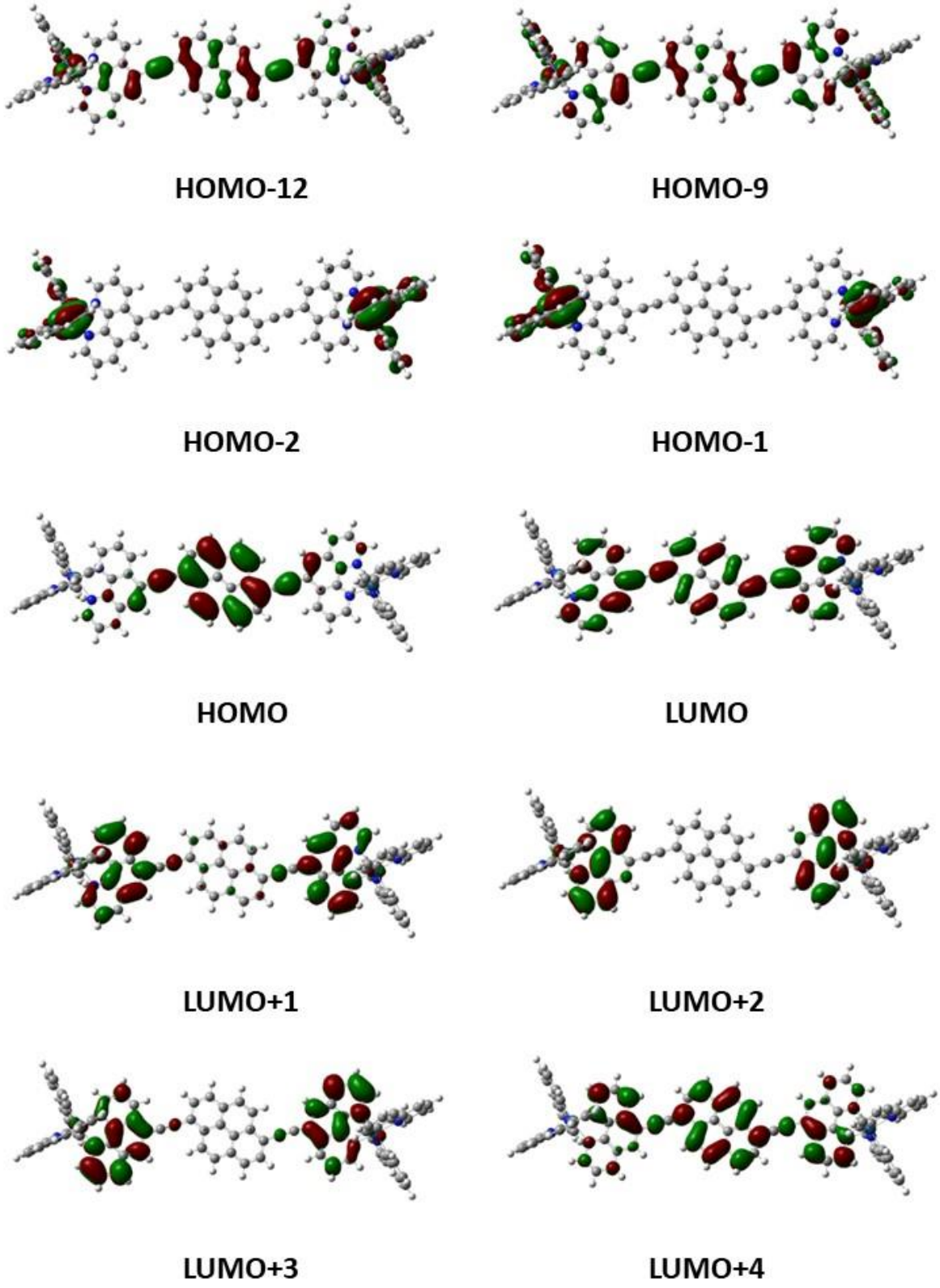

***Figure 4.10**: The frontier molecular orbitals of note of **Ir6**.*

4.4 Conclusions

In conclusion, two dinuclear Ir(III) complexes based on 1,10-phenantholine functionalised with diethynylpyrene, **Ir5** and **Ir6**, were successfully synthesised and investigated. In comparison to their mononuclear analogues, both **Ir5** and **Ir6** showed slightly red-shifted absorption bands with far higher molar absorption coefficients. In each case the absorption intensity was more than double that of its mononuclear analogue. **Ir5** and **Ir6** both show structured emission from a ^{3}IL state in the red region, confirmed by low-temperature emission, with slightly lower T_1 states than those of their mononuclear analogues. The development of triplet photosensitisers with, in comparison to their mononuclear analogues, significantly higher absorption intensity and marginally lower T_1 energy, is promising for future investigation.

As the data collected on these complexes is so far promising, there will be further photophysical analysis, including transient absorption, phosphorescence lifetime measurement, singlet oxygen sensitisation quantum yield, triplet quenching, and TTA-UC quantum yield measurements, carried out shortly.

4.5 Future Work

This work has continued work previously published by the Draper group.[25, 28] The results of both chapters have been promising, and so further research is now merited. **Ir2**, **Ir4**, **Ir5** and **Ir6** will all be investigated for their transient absorption, singlet oxygen sensitisation, triplet state quenching, and TTA-UC properties. It may be that one or more of them proves to be a significantly more efficient PS molecule with properties suited to TTA-UC. After these measurements, including **Ir1**, will be tested for their PDT properties if they are deemed viable.

While the results so far of the mononuclear complexes **Ir1** – **Ir4** are promising, the dinuclear complexes **Ir5** and **Ir6** are more novel and potentially more interesting for future investigation. Synthesis of dinuclear complexes in the style of **Ir5** and **Ir6**, replacing the ancillary ppy ligands with a strongly absorbing chromophore such as coumarin-6 (figure 3.13), should be investigated in order to ascertain whether such complexes could increase their absorption intensity without the loss of triplet state energy.

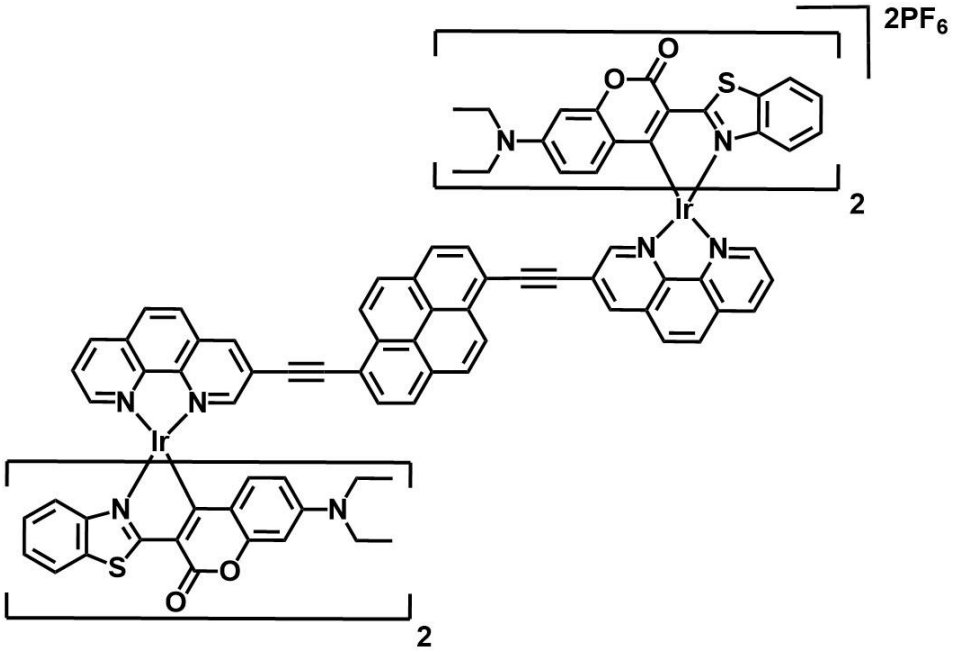

***Figure 3.13**: A hypothetical complex analogous to **Ir5**, utilising C6 as the ancillary ligand.*

Other chromophores could be investigated as the participating ligand in either a mono- or di-nuclear capacity. These could replace either the pyrene or phen moieties, for example in Figure 3.14 where *N*-heterobenzocoronene (NHSB) is used in place of the phen moieties in another complex analogous to **Ir5**. Such a complex would be arduous to synthesise but could result in vastly different electrochemical and photophysical properties.

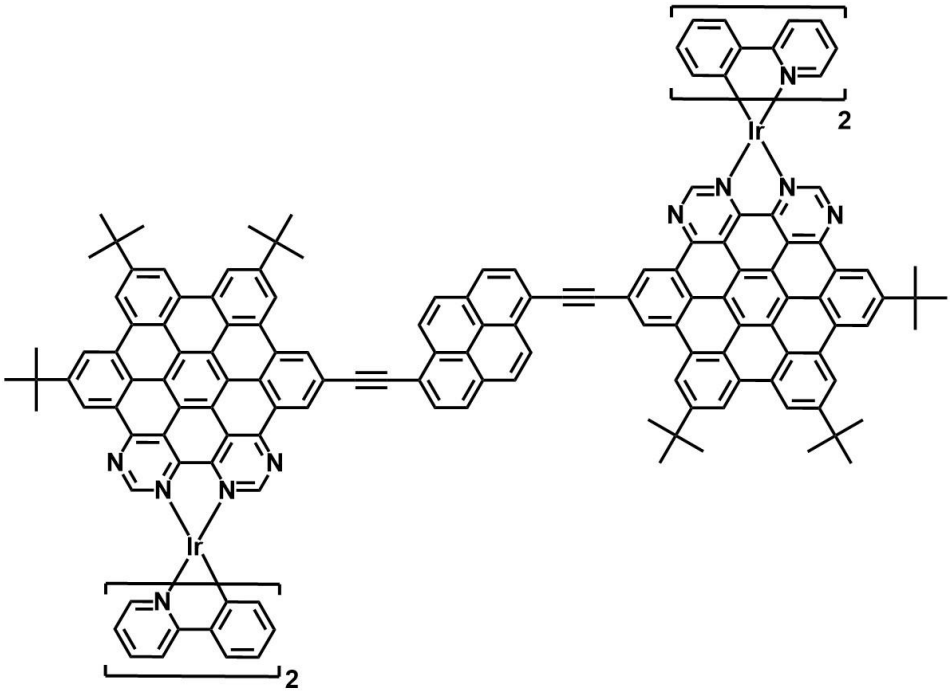

***Figure 3.14**: A hypothetical complex analogous to **Ir5**, utilising NHSB in place of the phen moieties.*

Chapter 5

Experimental

5.1 General Information

All reactions which are described as air sensitive were carried out under an inert atmosphere of either N_2 or Ar gas using a standard Schlenk line with a three-necked round-bottomed flask. Solvents were dried using a purification system made by Innovation Technology Inc. Triethylamine was distilled over sodium under a nitrogen atmosphere before use. Starting materials 1,10-phenanthroline, bromine, S_2Cl_2, pyridine, 1-chlorobutane, NaOH, $MgSO_4$, $H_2SO_4 \cdot SO_3$, $SOCl_2$, NH_3, coumarin-6, 2-phenylpyridine, 1-ethynylpyrene, 1,6-dibromopyrene, PPh_3, CuI, $Pd(PPh_3)_2Cl_2$ and $Pd(PPh_3)_4$ were used without further purification. $IrCl_3 \cdot H_2O$ was purchased from Alfa Aesar. Flash chromatography was performed using silica gel (VWR) as the stationary phase and the known compounds were synthesised according to literature procedures.

Mass Spectrometry: A Micromass-LCT spectrometer was used for all electrospray mass spectra. A Waters MALDI-Q-TOF Premier spectrometer with an α-cyano-4-hydroxycinnamic matrix was used to record all MALDI-TOF mass spectra. Accurate mass spectra were referenced against Leucine enkephalin (555.6 g mol^{-1}) or [Gluel]-Fibrinopeptide B (1570.6 g mol^{-1}), and were reported to within 5 ppm in each case. The solvents used to dissolve the samples were acetonitrile and dichloromethane.

NMR Spectroscopy: Nuclear magnetic resonance spectra were recorded in deuterated chloroform, acetonitrile and dimethyl sulfoxide on a (i) Bruker AV-400 MHz spectrometer, operating at 400.13 MHz for ^{1}H, and 100.6 MHz for ^{13}C, or (ii) a Bruker AV-600 MHz spectrometer (operating at 600.13 MHz for ^{1}H, 150.6 MHz for ^{13}C). ^{13}C spectra were proton decoupled. Chemical shifts (*d*) are reported in ppm and coupling constants (*J*) in Hertz.

Cyclic Voltammetry: Data were collected using a Shanghai Huachen CHI610D in a nitrogen atmosphere.

Photophysical Measurements: Most photophysical measurements were carried out with solutions contained in 1×1 cm^2 quartz cuvettes in HPLC grade solvents, except the low temperature emission measurements which were carried out in quartz tubes. All the measurements were carried out at least three times to maximise accuracy. Average values were calculated and presented in the thesis. UV-visible absorption spectra were recorded on a Shimadzu UV-2450 spectrophotometer. Emission spectra were obtained on a FluoroMax-4P Phosphorimeter. The phosphorescence lifetime was measured on OB920 and FLS 920 (Edinburgh Photonics) machines which were equipped with 405 nm, 445 nm, 473 nm picosecond lasers (series: EPL) and a microsecond Xe lamp (μF920H). The nanosecond time-resolved difference transient absorption spectra were detected by laser flash photolysis spectrometer (LP920, Edinburgh Instruments) and recorded on a Tektronix TDS 3012B oscilloscope. The laser source used is a nanosecond-pulsed Q-Switched Nd:YAG laser coupled to an Optical Parametric Oscillator (OPO) to create tunability over a wide range of wavelengths. A gated intensified CCD is used to capture the whole spectrum in the presence and absence of the pump laser pulse. The lifetime values (by monitoring the decay trace of the transients) were obtained with the LP920 software. The emission spectra at low temperature (77 K) were measured with a quartz tube in a Dewar filled with liquid nitrogen on a FluoroMax-4P Phosphorimeter in a glassed solvent system. Time-resolved emission spectra were recorded on an OB920 (Edinburgh Instruments). Luminescence quantum yields of the complexes were measured with different standard as reference (depending on their absorption and emission properties). The femtosecond time-resolved difference transient absorption spectra were measured by optical femtosecond pump-probe spectroscopy. The output of a mode-locked Ti-sapphire amplified laser system (Spitfire Ace, Spectra-Physics) with

wavelength 800 nm, pulse-width 35 fs, repetition rate 1 kHz, average power 4 W was split into two beams (10:1). The strong radiation was converted into UV-VIS-IR in the range of 240-2400 nm by use of Optical Parametric Amplifier (TOPAS, Light Conversion) and used as a pump beam. The weaker beam after passing a variable delay line (up to 6 ns) was focused in a 3 mm thickness rotated CaF_2 plate to produce a white light continuum (WLC), which was used as a probe beam. Home-built pump-probe setup was used for obtaining transient absorption spectra and kinetics. The entire setup was controlled by a PC through LabView software (National Instruments). All femtosecond measurements were performed at room temperature under aerated conditions.

IR spectroscopy: IR spectra were recorded on a PerkinElmer Spectrum 100 FTIR spectrometer fitted with a Universal ATR accessory in a solid form.

TTA Upconversion: A diode-pumped solid-state laser (473 nm, continuous wave (CW)) was used for the upconversion measurements. For the upconversion experiments, the mixed solution of the photosensitisers and triplet acceptor (DPA or perylene) was degassed in the solution for at least 15 min with N_2, and the gas flow was kept constant during the measurement. The solution was excited with the laser. Then the upconverted fluorescence was recorded with a spectrofluorometer. The upconversion quantum yields were determined with the prompt fluorescence of reference compound as the standard using the following equation:

$$\Phi_{UC} = 2 * \Phi_{STD} * \left(\frac{1-10^{-A_{STD}}}{1-10^{-A_{SAM}}}\right) * \frac{I_{SAM}}{I_{STD}} * \left(\frac{\eta_{SAM}}{\eta_{STD}}\right)^2$$

The subscripts "sam" and "std" refer to the photosensitiser and the reference compound (standard), respectively. Φ, A, I, and η represent the quantum yield, absorbance, integrated photoluminescence intensity, and the refractive index of the solvents used for the standard and the samples, respectively. The equation is multiplied by a factor of 2 in order to make the maximum quantum yield to be unity.

5.2 Synthetic Details

Synthesis of 5-bromo-1,10-phenanthroline (L1)

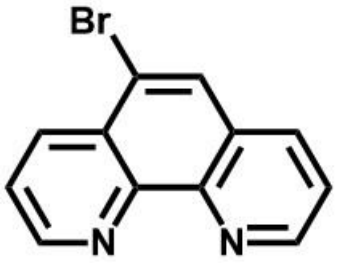

5-bromo-1,10-phenanthroline

1,10-phenanthroline (3.60 g, 20 mmol) and $H_2SO_4 \cdot SO_3$ (30%, 12 ml) were added to a pressure tube. Bromine (0.6 ml, 11.6 mmol) was added to the tube and the tube was sealed using Teflon tape. The vessel was slowly heated to 135°C and the reaction carried out for 23 hours, then allowed to cool to room temperature. The solution was washed with chloroform, before the organic solvent was removed to give a pink solid. This was purified by column chromatography on silica gel (CH_2Cl_2:MeOH, 100:1, v/v) to give a white solid. Yield: 0.61 g, 12 %.

^{1}H NMR (400 MHz, $CDCl_3$, 298 K, δ in ppm) 9.25 (td, 2H, J = 8, 4 Hz), 8.71 (dd, 1H, J = 8, 4 Hz), 8.22 (dd, 1H, J = 8, 4 Hz), 8.19 (s, 1H), 7.73 (dq, 2H, J = 36, 4 Hz).

Synthesis of 5,6-dibromo-1,10-phenanthroline (L2)

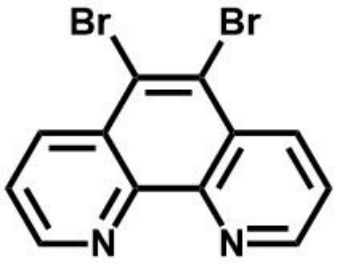

5,6-dibromo-1,10-phenanthroline

1,10-phenanthroline (10 g, 55.49 mmol) was dissolved in $H_2SO_4 \cdot SO_3$ (30%, 80 ml) and bromine (7.8 ml, 151.44 mmol) was added dropwise *via* syringe with stirring. The solution was heated to 150°C and reacted for 72 hours. The solution was allowed to cool to room temperature and neutralised with ammonium hydroxide over ice water. The solution was left to allow the organic products to crystallise. The crude solids were filtered and purified by column chromatography with silica gel (CH_2Cl_2:MeOH, 100:1,

v/v), before being dissolved in acetone and forcibly crashed out with hexane to give a white solid. Yield: 1.14 g, 6%.

^{1}H NMR (400 MHz, $CDCl_3$, 298 K, δ in ppm) 9.23 (dd, 2H, J = 4 Hz), 8.28 (dd, 2H, J = 8 Hz), 7.67 (q, 2H, J = 4 Hz).

Synthesis of 3,5,6,8-tetrabromo-1,10-phenanthroline (L3)

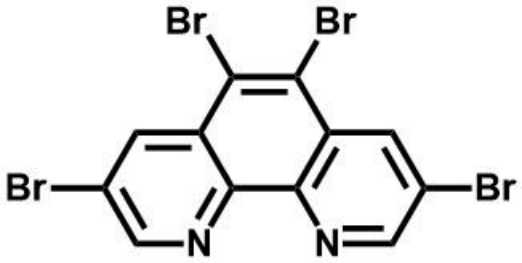

3,5,6,8-tetrabromo-1,10-phenanthroline

1,10-phenanthroline (4 g, 22.2 mmol) was dissolved in $SOCl_2$ (200 ml). Bromine (19.39 g, 121.35 mmol) was added over 1 hour *via* syringe pump. The solution was heated to 85°C and reacted at reflux for 44 hours before being allowed to cool to room temperature. The precipitate was filtered using a dry fritted glass funnel, and washed with a 2N aqueous solution of NH_3 until the washing liquid was colourless. The white product was dissolved in chloroform, washed with brine and dried over $MgSO_4$. Removal of the solvent gave an impure white solid. This was then recrystallized from toluene to give pure white crystals. Yield: 4.2 g, 38 %.

^{1}H NMR (400 MHz, $CDCl_3$, 298 K, δ in ppm) δ = 9.22 (d, 2H, *J* = 2.1 Hz), 8.95 (d, 2H, *J* = 2.1 Hz)

Synthesis of [Ir(5-bromo-1,10-phenanthroline)(coumarin-6)$_2$][PF_6] (IrBr1)

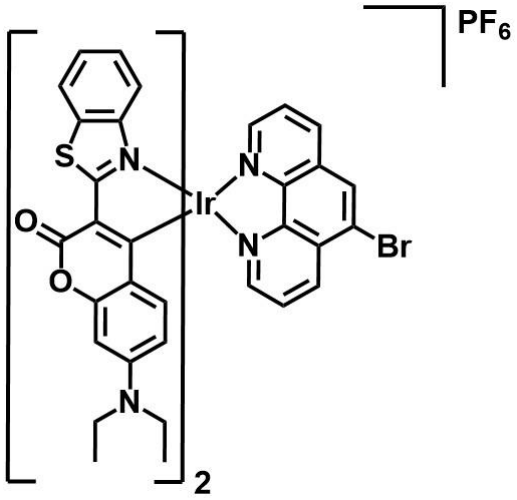

[Ir(5-bromo-1,10-phenanthroline)(coumarin-6)$_2$][PF$_6$]

[Ir(coumarin-6)$_2$(μ-Cl)]$_2$ (150.5 mg, 0.08 mmol) and 5-bromo-1,10-phenanthroline (42.5 mg, 0.16 mmol) were dissolved in CH_2Cl_2 (50 ml) with 5 drops of MeOH added. The solution was heated at reflux (50°C) overnight and cooled to room temperature. A solution of PF_6 in MeOH was added to the reaction solution, and the solvent removed under vacuum. The solid was dissolved in DCM and forced to crash out using toluene to give an orange precipitate which was filtered off. The solid was purified by column chromatography (CH_2Cl_2:MeOH, 100:1, v/v) to give an orange solid product. Yield: 143.6 mg, 69%

^{1}H NMR (400 MHz, MeCN, 298 K, δ in ppm) 9.22 (d, 1H, J = 4 Hz), 9.18 (d, 1H, J = 4 Hz), 8.96 (d, 1H, J = 8 Hz), 8.66 (d, 1H, J = 8 Hz), 8.47 (s, 1H), 8.17 (dd, 1H, J = 8 Hz), 9.07 (dd, 1H, J = 6 Hz), 7.85 (d, 2H, J = 6 Hz), 7.13 (t, 2H, J = 8 Hz), 6.75 (m, 2H), 6.49 (*pseudo*-t, 2H), 6.16 (d, 1H, J = 4 Hz), 6.13 (d, 1H, J = 4 Hz), 6.06 (dt, 2H, J = 12 Hz), 5.70 (d, 2H, J = 8 Hz), 3.34 (dd, 8H, J = 8 Hz), 1.05 (t, 12H, J = 8 Hz).

MALDI-TOF-MS: Calc. for ($[C_{52}H_{41}BrIrN_6O_4S_2]^+$) *m/z* = 1149.1443, found *m/z* = 1149.1423.

Synthesis of [Ir(5-(1-ethynylpyrene)-1,10-phenanthroline)(coumarin-6)$_2$][PF$_6$] (Ir1)

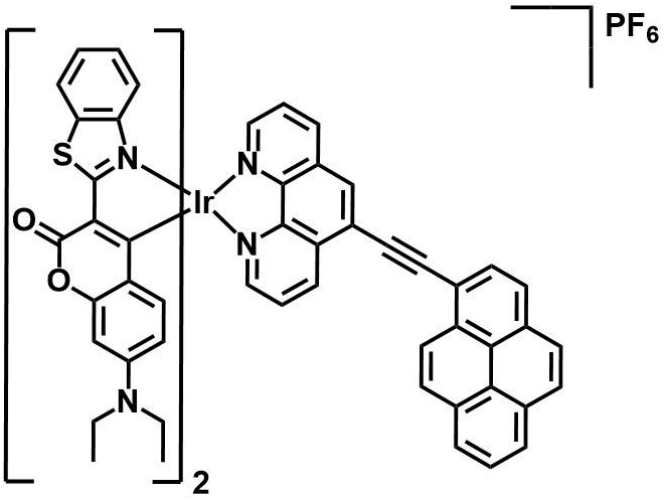

[Ir(5-(1-ethynylpyrene)-1,10-phenanthroline)(coumarin-6)$_2$][PF$_6$]

[Ir(5-bromo-1,10-phenanthroline)(coumarin-6)$_2$][PF$_6$] (100 mg, 0.08 mmol), 1-ethynylpyrene (61.7 mg, 0.27 mmol), CuI (2.3 mg, 0.01 mmol), PPh_3 (3.1 mg, 0.005 mmol) and $Pd(PPh_3)_2Cl_2$ (3.4 mg, 0.005 mmol) were added to a round-bottomed flask before it was flushed with argon. A solvent mix of Et_3N:DMF (2:5) was degassed under argon and 25 ml of this was transferred, under argon, to the degassed round-bottomed flask. The solution was refluxed at 60°C under argon for 24 hours. The solution was purified by column chromatography on silica gel (first with CH_2Cl_2:MeOH, 100:1, v/v; next with CH_2Cl_2:ethyl acetate, 95:5, v/v) to give a red-orange product. Yield: 32.1 mg, 29 %. M.p. > 300 °C.

^{1}H NMR (600 MHz, CH_2Cl_2, 298 K, δ in ppm) 9.62 (*pseudo*-d, 1H), 9.34 (*pseudo*-d, 1H), 8.86 (d, 1H, J = 8 Hz), 8.71 (d, 1H, J = 6 Hz), 8.58 (d, 1H, J = 4 Hz), 8.44 (d, 1H, J = 4 Hz), 8.39 (d, 1H, J = 6 Hz), 8.32 (m, 4H), 8.21 (m, 3H), 8.02 (t, 1H, J = 8 Hz), 7.91 (t, 2H, J = 8 Hz), 7.68 (d, 1H, J = 8 Hz), 7.28 (t, 2H, J = 6 Hz), 7.06 (t, 2H, J = 6 Hz), 6.58 (*pseudo*-d, 2H), 6.27 (d, 2H, J = 12 Hz), 6.16(d, 2H, J = 9 Hz), 6.09 (m, 2H), 3.38 (t, 4H, J = 6 Hz), 3.14 (m, 4H), 1.14 (t, 6H, J = 6 Hz), 1.07 (t, 6H, J = 6 Hz).
^{13}C NMR (600 MHz, CH_2Cl_2, 298 K, δ in ppm) 206.4, 191.1, 174.8, 167.0, 160.4, 157.7, 155.5, 153.0, 152.2, 150.5, 148.1, 144.5, 140.1, 136.4, 133.3, 133.0, 132.9, 132.3, 131.6, 131.5, 131.2, 131.1, 130.9, 130.8, 130.6, 130.5, 130.2, 129.9, 129.8, 129.7, 129.6, 127.8, 127.2, 126.8, 126.7, 126.6, 126.3, 124.9, 124.8, 124.5, 124.4, 124.0, 123.9, 123.7, 121.7, 115.5, 115.1, 114.5, 110.1, 96.8, 89.6, 72.1, 69.5, 58.9, 44.5, 13.7, 12.2.

MALDI-TOF-MS: Calc. for ($[C_{70}H_{50}IrN_6O_4S_2]^+$) *m/z* = 1295.2964, found *m/z* = 1295.2964.

IR (ν_{max} / cm^{-1}) 2980, 2200, 1687, 1601, 1441, 1412, 1140, 558.

Synthesis of [Ir(5,6-dibromo-1,10-phenanthroline)(coumarin-6)$_2$][PF_6] (IrBr2)

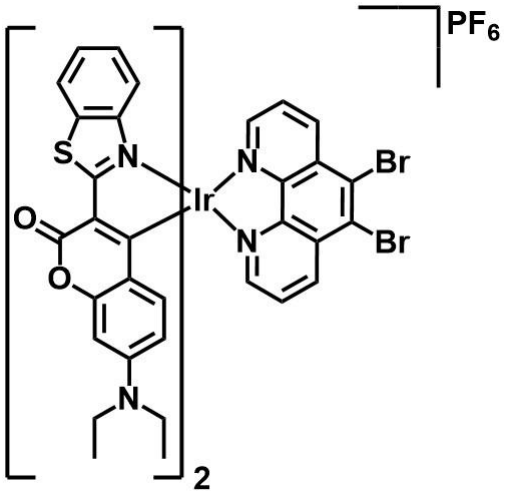

[Ir(5,6-dibromo-1,10-phenanthroline)(coumarin-6)$_2$][PF_6]

[Ir(coumarin-6)$_2$(μ-Cl)]$_2$ (109 mg, 0.06 mmol) and 5,6-dibromo-1,10-phenanthroline (42 mg, 0.12 mmol) were dissolved in CH_2Cl_2 (50 ml) with 5 drops of MeOH added. The solution was heated at reflux (50°C) overnight and cooled to room temperature. A solution of PF_6 in MeOH was added to the reaction solution, and the solvent removed under vacuum. The solid was dissolved in DCM and forced to crash out using hexane to give an orange precipitate which was filtered off. The solid was purified by column chromatography on silica gel (CH_2Cl_2:MeOH, 100:1, v/v) to give the solid red product. Yield: 138.2 mg, 86 %.

MALDI-TOF-MS: Calc. for ($[C_{52}H_{40}IrBr_2N_6O_4S_2]^+$) *m/z* = 1227.0549, found *m/z* = 1227.0571.

Synthesis of [Ir(5,6-di(1-ethynylpyrene)-1,10-phenanthroline)(coumarin-6)$_2$][PF_6] (Ir2)

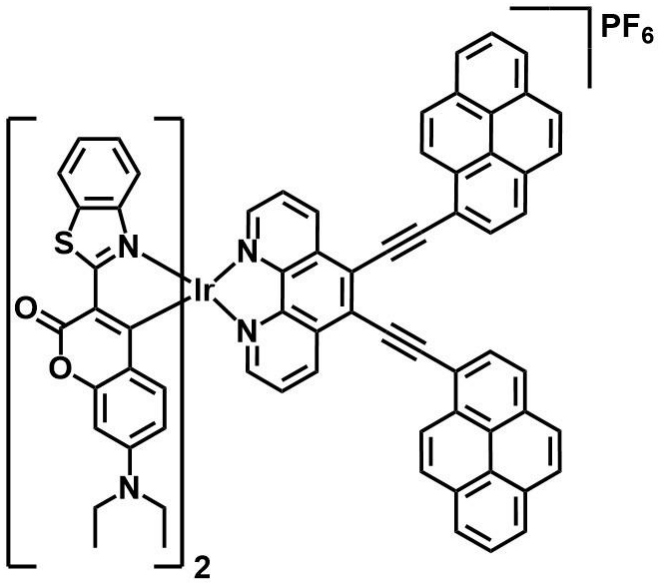

[Ir(5,6-di(1-ethynylpyrene)-1,10-phenanthroline)(coumarin-6)$_2$][PF_6]

[Ir(5,6-dibromo-1,10-phenanthroline)(coumarin-6)$_2$][PF_6] (100.1 mg, 0.07 mmol), 1-ethynylpyrene (95.3 mg, 0.4 mmol), CuI (1.9 mg, 0.01 mmol), PPh_3 (3.1 mg, 0.01 mmol) and $Pd(PPh_3)_2Cl_2$ (2.9 mg, 0.004 mmol) were added to a round-bottomed flask before it was flushed with argon. A solvent mix of Et_3N:CH_3CN (2:5) was degassed under argon and 25 ml of this was transferred, under argon, to the degassed round-bottomed flask. The solution was heated to 80°C under argon for 24 hours. The solution was purified by column chromatography on silica gel (first with CH_2Cl_2:MeOH, 100:1, v/v; next with CH_2Cl_2:ethyl acetate, 95:5, v/v) to give a red-orange product. Yield: 24.3 mg, 21 %. M.p. > 300 °C.

^{1}H NMR (600 MHz, CH_2Cl_2, 298 K, δ in ppm) 9.37 (d, 2H, J = 3 Hz), 9.17 (d, 2H, J = < 3 Hz), 9.07 (d, 2H, J = < 3 Hz), 8.72 (dd, 4H, J = 6 Hz), 8.48 (s, 2H), 8.37 (m, 3H), 8.27 (m, 3H), 8.15 (m, 2H), 7.82 (t, 2H, J = 9 Hz), 7.17 (t, 2H, J = 6 Hz), 6.81 (dd, 2H, J = 6 Hz), 6.49 (s, 2H), 6.15 (d, 2H, J = 3 Hz), 6.00 (m, 2H), 5.75 (q, 2H, J = 6 Hz), 3.35 (t, 6H, J = 6 Hz), 3.14 (t, 2H, J = 6 Hz), 1.13 (t, 9H, J = 6 Hz), 1.06 (t, 3H, J = 6 Hz).
^{13}C NMR (600 MHz, CH_2Cl_2, 298 K, δ in ppm) 206.4, 179.7, 179.4, 177.9, 177.9, 157.8, 155.3, 152.9, 151.1, 150.7, 148.1, 148.1, 148.0, 147.3, 146.6, 139.9, 139.2, 132.7, 132.4,

132.3, 132.3, 131.4, 131.3, 131.2, 131.1, 130.9, 130.1, 129.4, 129.4, 127.7, 127.6, 127.4, 127.2, 126.8, 126.5, 126.4, 124.8, 124.7, 124.7, 124.4, 124.0, 123.5, 123.5, 123.1, 121.8, 121.8, 118.7, 118.7, 115.2, 115.2, 110.0, 99.0, 96.7, 88.7, 58.8, 44.8, 13.2, 12.2.

MALDI-TOF-MS: Calc. for ($[C_{88}H_{58}IrN_6O_4S_2]^+$) *m/z* = 1519.3590, found *m/z* = 1519.3618.

IR (ν_{max} / cm^{-1}) 2918, 2858, 2185, 1700, 1446, 1413, 558.

Synthesis of [Ir(3,5,6,8-tetrabromo-1,10-phenanthroline)(coumarin-6)$_2$][PF_6] (IrBr3)

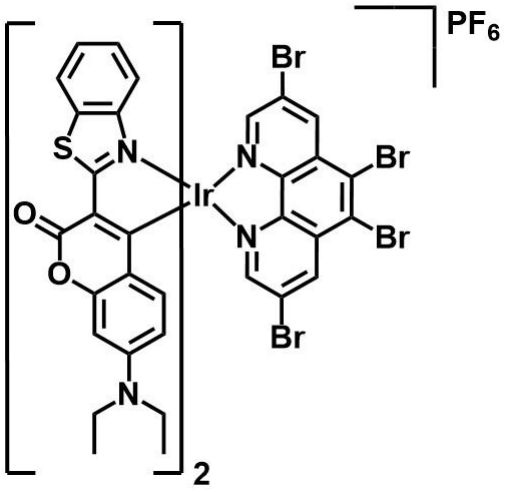

[Ir(3,5,6,8-tetrabromo-1,10-phenanthroline)(coumarin-6)$_2$][PF_6]

[Ir(coumarin-6)$_2$(μ-Cl)]$_2$ (102 mg, 0.06 mmol) and 3,5,6,8-tetrabromo-1,10-phenanthroline (54.6 mg, 0.11 mmol) were dissolved in CH_2Cl_2 (50 ml) with 5 drops of MeOH added. The solution was heated at reflux (50°C) for 5 hours and cooled to room temperature. A solution of PF_6 in MeOH was added to the reaction solution, and the solvent removed under vacuum. The solid was dissolved in DCM and forced to crash out using toluene to give a red precipitate which was filtered off. The solid was purified by column chromatography on silica gel (CH_2Cl_2:MeOH, 100:1, v/v) to give the red-orange solid product Yield: 126.22 mg, 83 %

^{1}H NMR (400 MHz, DMSO-d_6, 298 K, δ in ppm) 9.21 (d, 4H, J = 8Hz), 8.16 (m, 1H), 7.99 (d, 1H, J = 6 Hz), 7.41 (m, 2H), 7.16 (t, 2H, J = 4 Hz), 6.86 (t, 2H, J = 6 Hz), 6.45 (s, 1H), 6.29 (s, 1H), 5.90 (m, 4H), 3.28 (m, 8H), 1.19 (m, 12H).

MALDI-TOF-MS: Calc. for ($[C_{52}H_{38}IrBr_4N_6O_4S_2]^+$) *m/z* = 1382.8759, found *m/z* = 1382.8705.

Synthesis of [Ir(3,5,6,8-tetra(1-ethynylpyrene)-1,10-phenanthroline)(coumarin-6)$_2$][PF$_6$] (Ir3)

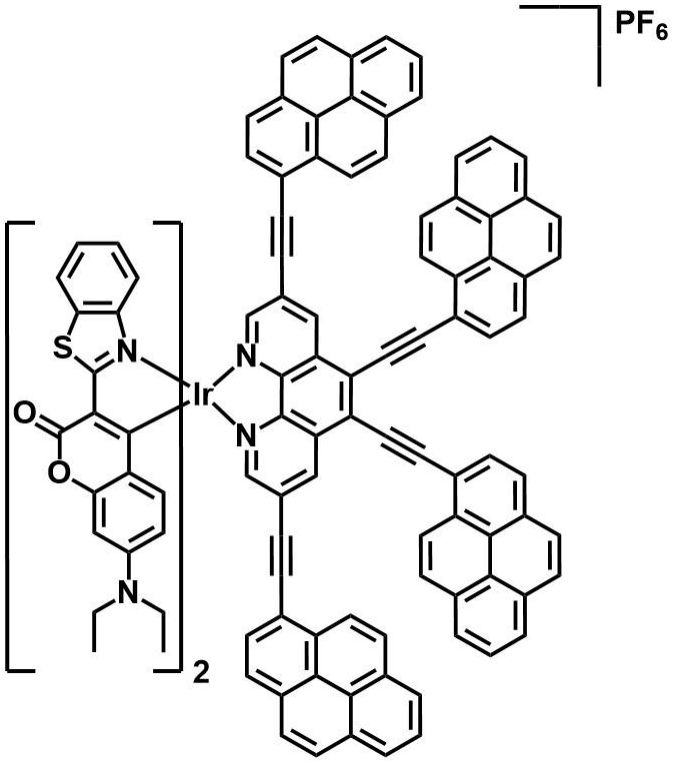

[Ir(3,5,6,8-tetra(1-ethynylpyrene)-1,10-phenanthroline)(coumarin-6)$_2$][PF$_6$]

[Ir(3,5,6,8-dibromo-1,10-phenanthroline)(coumarin-6)$_2$][PF$_6$] (90.1 mg, 0.06 mmol), 1-ethynylpyrene (141.3 mg, 0.6 mmol), CuI (2.3 mg, 0.01 mmol), PPh_3 (3.2 mg, 0.01 mmol) and $Pd(PPh_3)_4$ (3.8 mg, 0.003 mmol) were added to a round-bottomed flask before it was flushed with argon. A solvent mix of Et_3N:CH_3CN (2:5) was degassed under argon and 25 ml of this was transferred, under argon, to the degassed round-bottomed flask. The solution was heated to 80°C under argon for 27 hours. The solution was purified by column chromatography on silica gel (first with CH_2Cl_2:MeOH, 100:1, v/v; next with CH_2Cl_2:ethyl acetate, 95:5, v/v) followed by preparative TLC plate (CH_2Cl_2:EtOAc, 95:5, v/v) to give a dark red-purple product. Yield: 1.1 mg, <1 %

^{1}H NMR (400 MHz, CH_2Cl_2, 298 K, δ in ppm) 9.43 (d, 2H, J = 8 Hz), 9.17 (d, 2H, J = 8 Hz), 8.70 (d, 2H, J = 8 Hz), 8.46 (d, 2H, J = 8 Hz), 8.23 (m, 9H), 7.99 (t, 2H, J = 8 Hz), 7.88 (dd, 3H, J = 4 Hz), 7.52 (d, 2H, J = 8 Hz), 7.21 (t, 2H, J = 8 Hz), 6.89 (t, 2H, J = 8 Hz), 6.51 (d, 2H, J = 2 Hz), 6.17 (d, 2H, J = 6 Hz), 6.02 (dd, 2H, J = 4 Hz), 5.84 (d, 2H, J = 8 Hz), 3.37 (m, 8H), 1.14 (t, 12H, J = 8 Hz).

^{13}C NMR (100 MHz, CH_2Cl_2, 298 K, δ in ppm) 206.4, 179.6, 177.9, 157.8, 155.3, 152.9, 150.9, 148.1, 146.6, 139.2, 132.8, 132.7, 132.3, 131.4, 131.1, 131.0, 130.5, 130.5, 129.5, 129.3, 128.0, 127.5, 127.1, 126.6, 126.4, 126.2, 124.9, 124.8, 124.8, 124.7, 124.3, 123.8, 123.5, 121.8, 118.7, 115.2, 115.2, 110.0, 104.2, 96.7, 89.5, 44.9, 12.2.

MALDI-TOF-MS: Calc. for ($[C_{124}H_{74}IrN_6O_4S_2]^+$) *m/z* = 1967.4842, found *m/z* = 1967.4772.

Synthesis of [Ir(3,5,6,8-tetrabromo-1,10-phenanthroline)(ppy)$_2$][PF$_6$] (IrBr4)

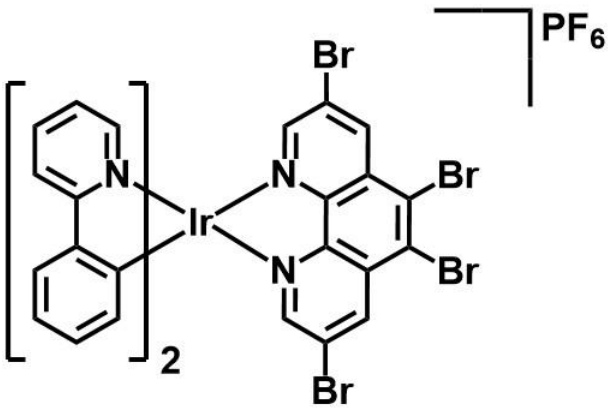

[Ir(3,5,6,8-tetrabromo-1,10-phenanthroline)(ppy)$_2$][PF$_6$]

$[Ir(ppy)_2(\mu\text{-}Cl)]_2$ (101 mg, 0.09 mmol) and 3,5,6,8-tetrabromo-1,10-phenanthroline (95.1 mg, 0.19 mmol) were dissolved in CH_2Cl_2 (50 ml) with 5 drops of MeOH added. The solution was heated at reflux (50°C) overnight and cooled to room temperature. A solution of PF_6 in MeOH was added to the reaction solution, and the solvent removed under vacuum. The solid was dissolved in DCM and forced to crash out using toluene to give a red precipitate which was filtered off to give the dark red solid product. Yield: 90.6 mg, 88 %

^{1}H NMR (400 MHz, MeCN, 298 K, δ in ppm) 9.18 (s, 2H), 8.26 (s, 2H), 8.10 (d, 2H, J = 3 Hz), 7.87 (t, 2H, J = 6 Hz), 7.51 (t, 2H, J = 4 Hz), 7.14 (t, 2H, J = 4 Hz), 7.02 (t, 2H, J = 4 Hz), 6.93 (t, 2H, J = 3 Hz), 6.35 (d, 2H, J = 6 Hz), 5.47 (s, 2H).
MALDI-TOF-MS: Calc. for ($[C_{34}H_{20}IrBr_4N_4]^+$) *m/z* = 992.8051, found *m/z* = 992.8054.

Synthesis of [Ir(3,5,6,8-tetra(1-ethynylpyrene)-1,10-phenanthroline)(ppy)$_2$][PF$_6$] (Ir4)

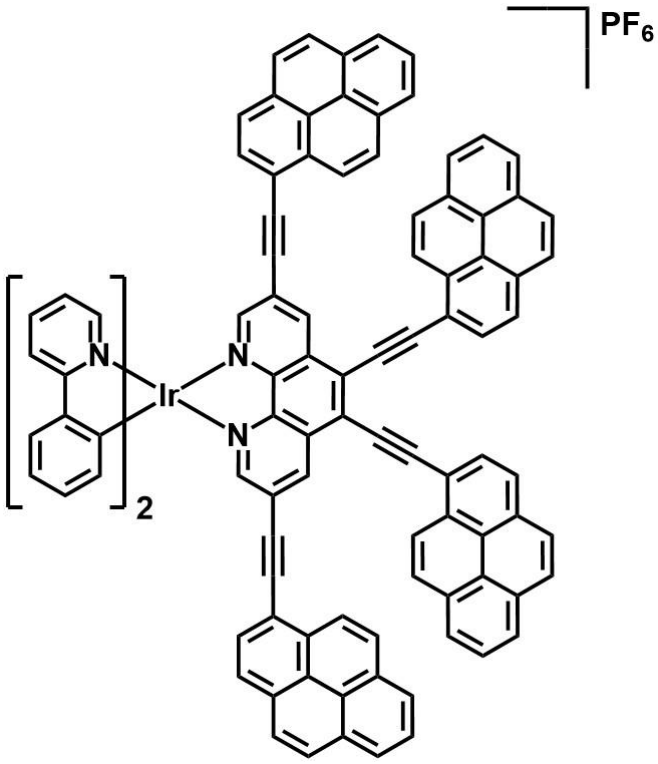

[Ir(3,5,6,8-tetra(1-ethynylpyrene)-1,10-phenanthroline)(ppy)$_2$][PF$_6$]

[Ir(3,5,6,8-dibromo-1,10-phenanthroline)(ppy)$_2$][PF$_6$] (60 mg, 0.05 mmol), 1-ethynylpyrene (35.8 mg, 0.16 mmol), CuI (7.6 mg, 0.04 mmol), PPh_3 (10.5 mg, 0.04 mmol) and $Pd(PPh_3)_4$ (8.8 mg, 0.02 mmol) were added to a round-bottomed flask before it was flushed with argon. A solvent mix of Et_3N:CH_3CN (2:5) was degassed under argon and 25 ml of this was transferred, under argon, to the degassed round-bottomed flask. The solution was heated to 80°C under argon for 48 hours. The solution was purified by column chromatography on silica gel (first with CH_2Cl_2:MeOH, 100:1, v/v; next with

CH_2Cl_2:ethyl acetate, 95:5, v/v) to give a dark purple-red product. Yield: 42.1 mg, 41 %. M.p. > 300 °C.

^{1}H NMR (400 MHz, CH_2Cl_2, 298 K, δ in ppm) 9.54 (*pseudo*-d, 2H) 8.88 (d, 2H, J = 12 Hz), 8.62 (*pseudo*-d, 2H), 8.56 (d, 2H, J = 8 Hz), 8.46 (d, 2H, J = 8 Hz), 8.22 (m, 14H), 8.09 (m, 6H), 7.93 (m, 3H), 7.84 (m, 3H), 7.60 (m, 6H), 7.51 (m, 2H), 7.43 (m, 4H), 7.30 (t, 2H, J = 8 Hz), 7.16 (t, 2H, J = 8 Hz), 7.02 (t, 2H, J = 8 Hz), 6.55 (d, 2H, J = 3 Hz).
^{13}C NMR (100 MHz, CH_2Cl_2, 298 K, δ in ppm) 168.0, 153.6, 148.8, 148.3, 144.5, 143.9, 138.7, 138.3, 132.9, 132.9, 132.8, 132.7, 132.5, 132.0, 131.9, 131.2, 131.2, 130.8, 130.7, 130.6, 130.7, 129.6, 129.5, 129.5, 128.5, 128.5, 127.2, 127.2, 126.8, 126.7, 126.6, 126.6, 126.4, 126.3, 125.4, 125.2, 124.9, 124.9, 124.8, 124.8, 124.5, 124.5, 124.4, 124.0, 123.9, 123.6, 123.4, 120.4, 115.5, 114.8, 104.4, 98.1, 90.2, 90.0.
MALDI-TOF-MS: Calc. for ($[C_{106}H_{56}IrN_4]^+$) *m/z* = 1577.4134, found *m/z* = 1577.4209.
IR (ν_{max} / cm^{-1}) 3050, 2364, 2344, 2203, 1582, 1479, 557.

Synthesis of 1,6-diethynylpyrene (L9)

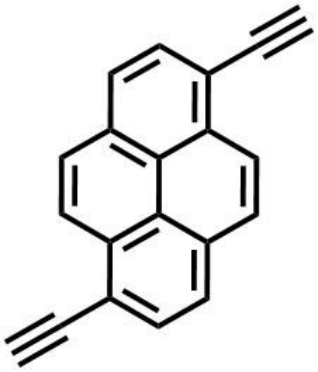

1,6-diethynylpyrene

1,6-dibromopyrene (100 mg, 0.28 mmol), 2-methylbut-3-yn-2-ol (48.1 mg, 0.57 mmol), $Pd(PPh_3)_2Cl_2$ (39.3 mg, 0.06 mmol), PPh_3 (29.4 mg, 0.11 mmol) and CuI (21.3 mg, 0.11 mmol) were degassed with argon. A solvent mixture of dry DMF:Et_3N (5:2, 12 ml) was degassed using argon, and added to the reagents under argon. The solution was reacted at 100°C for 24 hours under argon. The solution cooled to room temperature and the solvent was removed. A solution of NaOH (25 mg, 0.63 mmol) in toluene (20 ml) was added to the product and reacted at 120°C for 12 hours. The solvent was removed and the product was purified by column chromatography (petroleum ether:EtOAc, 70:30, v/v) to give a white product. Yield: 41.3 mg, 59 %.

^{1}H NMR (400 MHz, $CDCl_3$, 298 K, δ in ppm) 8.65 (d, 2H, J = 12 Hz), 8.19 (m, 6H), 3.66 (s, 2H).

Synthesis of 3-bromo-1,10-phenanthroline (L7) and 3,8-dibromo-1,10-phenanthroline (L8)

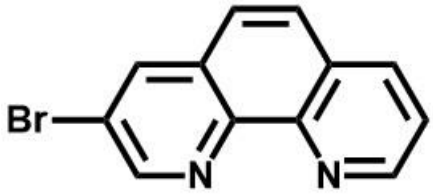

3-bromo-1,10-phenanthroline

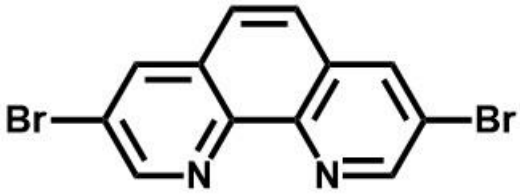

3,8-dibromo-1,10-phenanthroline

1,10-phenanthroline (5.01 g, 27.8 mmol) was dissolved in 1-chlorobutane (200 ml) under argon. S_2Cl_2 (11.15 g, 82.6 mmol), pyridine (6.48 g, 81.9 mmol) and bromine (12.41 g, 77.7 mmol) were added dropwise *via* syringe. The solution was heated at reflux at 110°C for 10 hours. The solution was cooled and added to a solution of aqueous NaOH (10%, 200 ml) and chloroform (200 ml), which was then stirred thoroughly and the organic layer separated. The solution was dried over $MgSO_4$ and the solid product purified by column chromatography on silica gel (CH_2Cl_2:MeOH, 100:1, v/v) to give multiple fractions of white solids. Yield: 3-bromo-1,10-phenanthroline: 1.01 g, 14%; 3,8-dibromo-1.10-phenanthroline: 1.56 g, 17 %.

L7:

^{1}H NMR (400 MHz, $CDCl_3$, 298 K, δ in ppm) 9.37 (s, 1H), 9.27 (*pseudo*-d, 1H), 8.49 (d, 1H, J = 4 Hz), 8.45 (d, 1H, J = 8 Hz), 7.89 (dd, 2H, J = 28 Hz), 7.82 (m, 1H).

L8:

^{1}H NMR (400 MHz, $CDCl_3$, 298 K, δ in ppm) 9.19 (d, 2H, J = 4Hz), 8.49 (d, 2H, J = 4 Hz), 7.83 (s, 2H).

Synthesis of [Ir(3-bromo-1,10-phenanthroline)$(ppy)_2$][PF_6] (IrBr5)

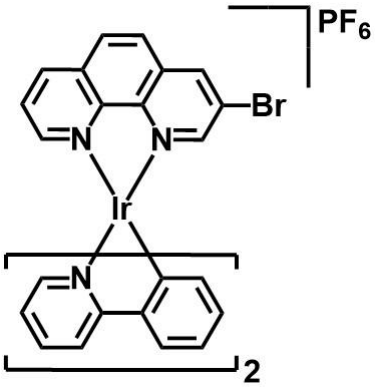

3-bromo-1,10-phenanthroline (28.1 mg, 0.11 mmol) and $[Ir(ppy)_2(\mu\text{-}Cl)]_2$ (57.7 mg, 0.054 mmol) were dissolved in CH_2Cl_2 (40 ml) with 5 drops of MeOH added. The solution was reacted at reflux overnight and allowed to cool to RT. A saturated solution of KPF_6 in MeOH was added, and the solution was dried. The product was then crashed from CH_2Cl_2 using hexane, and filtered and washed with diethyl ether to give an orange solid. Yield: 76.8 mg, 78 %.

^{1}H NMR (400 MHz, Acetone-d_6, 298 K, δ in ppm) 9.17 (s, 1H), 8.95 (d, 1H, J = 8 Hz), 8.48 (t, 2H, J = 4 Hz), 8.38 (t, 2H, J = 4 Hz), 8.26 (dd, 1H, J = 4 Hz), 7.94 (m, 4H), 7.87 (d, 1H, J = 4 Hz), 7.70 (1H, J = 4 Hz), 7.11 (dd, 2H, J = 8 Hz), 7.01 (dt, 4 H, J = 8 Hz), 8.47 (dd, 2H, J = 12, 4 Hz).

Synthesis of [Ir(3-(μ-ethynylpyrene)$_{1/2}$-1,10-phenanthroline)$(ppy)_2$][PF_6] (Ir5)

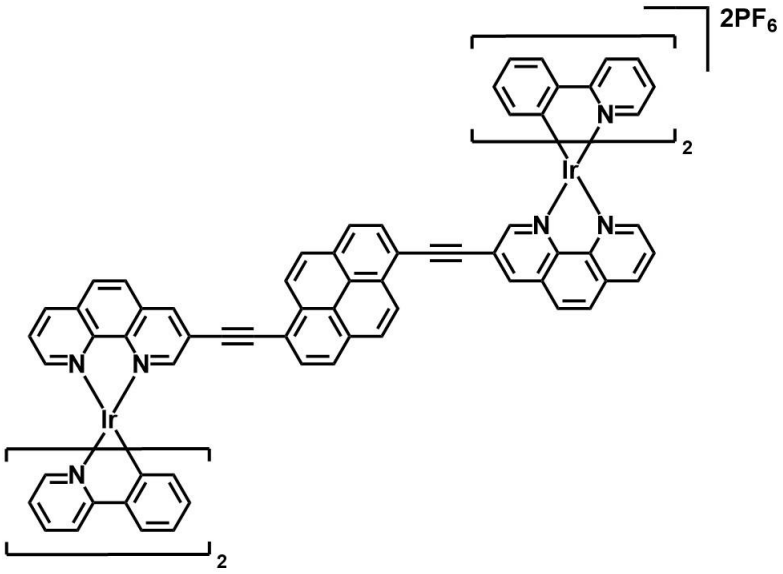

[Ir(3-bromo-1,10-phenanthroline)(ppy)$_2$][PF$_6$] (121.3 mg, 0.13 mmol) and 1,6-diethynylpyrene (15 mg, 0.06 mmol), Pd(PPH$_3$)$_2$Cl$_2$ (35.6 mg, 0.05 mmol), PPh$_3$ (26.6 mg, 0.10 mmol) and CuI (19.5 mg, 0.10 mmol) were degassed with argon. A solution of dry MeCN:Et$_3$N (5:2, v/v, 12 ml) was degassed with argon and added to the reagents under atmosphere. The solution was reacted at 80°C for 26 hours and allowed to cool to room temperature. The solvent was removed and the product was purified first by column chromatography (CH_2Cl_2:MeOH, 100:1, v/v) and then by preparative TLC plate (CH_2Cl_2:EtOAc, 95:5, v/v) to give a bright orange product. Yield: 21.1 mg, 19 %.

^{1}H NMR (600 MHz, CH_2Cl_2, 298 K, δ in ppm) 8.95 (d, 2H), 8.69 (dd, 2H, J = 6 Hz), 8.61 (d, 2H, J = 12 Hz), 8.58 (d, 2H, J = 3 Hz), 8.42 (dd, 2H, J = 6 Hz), 8.33 (m, 10H), 8.07 (d, 2H, J = 6 Hz), 8.04 (d, 2H, J = 6 Hz), 7.90 (m, 4H), 7.83 (m, 6H), 7.53 (d, 2H, J = 6 Hz), 7.43 (d, 2H, J = 6 Hz), 7.29 (td, 2H, J = 9 Hz), 7.18 (dtd, 4H, J = 6 Hz), 7.0 (td, 2H, J = 6 Hz), 6.95 (m, 4H), 6.56 (d, 2H, J = 6 Hz), 6.49 (d, 2H, J = 6 Hz).

^{13}C NMR (150 MHz, CH_2Cl_2, 298 K, δ in ppm) 167.9, 167.8, 153.0, 151.5, 149.0, 148.7, 148.6, 146.7, 145.3, 144.0, 143.8, 139.9, 138.6, 138.3, 132.5, 132.2, 132.0, 131.8, 131.7, 131.1, 130.9, 130.8, 130.5, 129.3, 129.0, 128.3, 126.8, 126.4, 125.9, 125.2, 125.0, 123.9, 123.5, 123.3, 123.1, 123.0, 120.1, 119.9, 116.6, 95.9, 90.5,

MALDI-TOF-MS: Calc. for ([$C_{88}H_{54}Ir_2N_8PF_6$]$^+$) *m/z* = 1753.3372, found *m/z* = 1753.3339.

IR (ν_{max} / cm^{-1}) 2923, 2364, 2330, 2203, 1474, 555.

Synthesis of [Ir(3-bromo-1,10-phenanthroline)(ppy)$_2$][PF$_6$] (IrBr6)

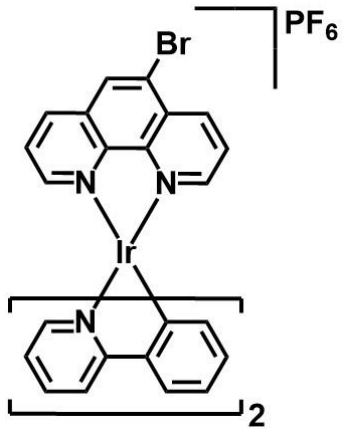

5-bromo-1,10-phenanthroline (29.4 mg, 0.11 mmol) and $[Ir(ppy)_2(\mu\text{-}Cl)]_2$ (58.1 mg, 0.054 mmol) were dissolved in CH_2Cl_2 (40 ml) with 5 drops of MeOH added. The solution was reacted at reflux overnight and allowed to cool to RT. A saturated solution of KPF_6 in MeOH was added, and the solution was dried. The product was then crashed from CH_2Cl_2 using hexane, and filtered and washed with diethyl ether to give an orange solid. Yield: 83.1mg, 91 %.

^{1}H NMR (400 MHz, Acetone-d_6, 298 K, δ in ppm) 9.05 (d, 1H, J = 8 Hz), 8.89 (m, 2 H), 8.51 (dd, 2H, J = 16, 4 Hz), 8.25 (d, 2H, J = 8 Hz), 8.21 (t, 2H, J = 8 Hz), 8.11 (t, 1H, J = 8 Hz), 7.94 (t, 3H, J = 8 Hz), 7.73 (t, 2H, J = 4 Hz), 7.09 (t, 2H, J = 4 Hz), 6.99 (m, 4 H), 6.46 (dd, 2H, J = 4 Hz).

Synthesis of [Ir(5-(μ-ethynylpyrene)$_{1/2}$-1,10-phenanthroline)(ppy)$_2$][PF$_6$] (Ir6)

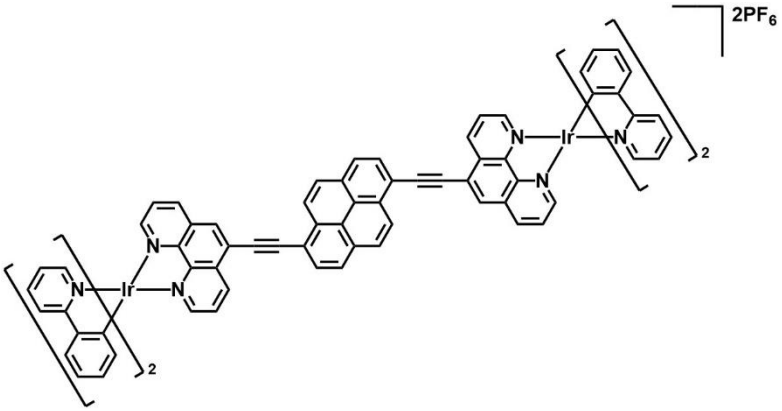

$[Ir(5\text{-bromo-1,10-phenanthroline})(ppy)_2][PF_6]$ (120.1 mg, 0.13 mmol) and 1,6-diethynylpyrene (15.1 mg, 0.06 mmol), $Pd(PPH_3)_2Cl_2$ (36.0 mg, 0.05 mmol), PPh_3 (26.5 mg, 0.10 mmol) and CuI (19.8 mg, 0.10 mmol) were degassed with argon. A solution of

dry MeCN:Et_3N (5:2, v/v, 12 ml) was degassed with argon and added to the reagents under atmosphere. The solution was reacted at 80°C for 26 hours and allowed to cool to room temperature. The solvent was removed and the product was purified first by column chromatography (CH_2Cl_2:MeOH, 100:1, v/v) and then by preparative TLC plate (CH_2Cl_2:EtOAc, 95:5, v/v) to give a bright orange product. Yield: 26.8 mg, 24 %.

^{1}H NMR (600 MHz, CH_2Cl_2, 298 K, δ in ppm) 9.32 (dd, 2H, J = 6 Hz), 8.88 (d, 2H, J = 6 Hz), 8.74 (d, 2H, J = 6 Hz), 8.71 (s, 2H), 8.48 (m, 4H), 8.38 (m, 6H), 8.06 (dd, 2H, J = 4 Hz), 8.03 (d, 2H, J = 8 Hz), 7.91 (td, 2H, J = 4 Hz), 7.85 (d, 2H, J = 3 Hz), 7.81 (t, 2H, J = 9 Hz), 7.45 (t, 2H, J = 6 Hz), 7.18 (t, 2H, J = 4 Hz), 7.07 (m, 2H), 6.95 (td, 2H, J = 4 Hz), 6.49 (t, 2H, J = 3 Hz).

^{13}C NMR (150 MHz, CH_2Cl_2, 298 K, δ in ppm) 167.8, 151.7, 151.5, 149.2, 149.0, 148.6, 147.0, 146.5, 143.9, 143.9, 138.3, 138.3, 137.3, 132.4, 132.1, 131.9, 131.8, 131.4, 131.2, 130.8, 129.0, 127.2, 126.6, 125.9, 125.0, 124.0, 123.3, 123.0, 122.7, 119.9, 117.0, 97.5, 90.0.

MALDI-TOF-MS: Calc. for ($[C_{88}H_{54}Ir_2N_8PF_6]^+$) *m/z* = 1753.3372, found *m/z* = 1753.3306.

IR (ν_{max} / cm^{-1}) 3046, 2354, 2335, 1294, 1474, 1423, 1267, 555.

References

1. K. Börjesson, D. Dzebo, B. Albinsson and K. Moth-Poulsen, *Journal of Materials Chemistry A*, 2013, **1**, 8521-8524.
2. M. Hosoyamada, N. Yanai, K. Okumura, T. Uchihashi and N. Kimizuka, *Chemical Communications*, 2018, **54**, 6828-6831.
3. K. Mase, Y. Sasaki, Y. Sagara, N. Tamaoki, C. Weder, N. Yanai and N. Kimizuka, *Angewandte Chemie*, 2018, **130**, 2856-2860.
4. K. Edel, X. Yang, J. S. A. Ishibashi, A. N. Lamm, C. Maichle-Mössmer, Z. X. Giustra, S.-Y. Liu and H. F. Bettinger, *Angewandte Chemie International Edition*, 2018, **57**, 5296-5300.
5. M. J. Kang, E. G. Santoro and Y. S. Kang, *ACS Omega*, 2018, **3**, 9505-9512.
6. L. Latterini, G. Massaro, M. Penconi, P. L. Gentili, C. Roscini and F. Ortica, *Dalton Transactions*, 2018, **47**, 8557-8565.
7. C. Ye, J. Wang, X. Wang, P. Ding, Z. Liang and X. Tao, *Physical Chemistry Chemical Physics*, 2016, **18**, 3430-3437.
8. M. Barawi, F. Fresno, R. Pérez-Ruiz and V. A. de la Peña O'Shea, *ACS Applied Energy Materials*, 2019, **2**, 207-211.
9. Q. Liu, W. Feng, T. Yang, T. Yi and F. Li, *Nature Protocols*, 2013, **8**, 2033.
10. S. H. C. Askes and S. Bonnet, *Nature Reviews Chemistry*, 2018, **2**, 437-452.
11. H.-S. Qian and Y. Zhang, *Langmuir*, 2008, **24**, 12123-12125.
12. F. Wang and X. Liu, *Chemical Society Reviews*, 2009, **38**, 976-989.
13. C. A. Parker and C. G. Hatchard, *Transactions of the Faraday Society*, 1961, **57**, 1894-1904.
14. W. Shockley and H. J. Queisser, *Journal of Applied Physics*, 1961, **32**, 510-519.
15. C. A. Parker and C. G. Hatchard, *Proc. Chem. Soc., London*, 1962, 386-387.
16. A. Monguzzi, J. Mezyk, F. Scotognella, R. Tubino and F. Meinardi, *Physical Review B*, 2008, **78**, 195112.
17. J. Zhang and K. R. Smith, *Environmental Health Perspectives*, 2007, **115**, 848-855.
18. R. Tang and Z. Wang, *Atmospheric Pollution Research*, 2018, **9**, 552-560.
19. S. Sharma, K. K. Jain and A. Sharma, *Materials Sciences and Applications*, 2015, **Vol.06No.12**, 12.
20. How Photovoltaic Cells Generate Electricity, (accessed 06/05/2018).

21. Tanaka exclusively supply ruthenium dye for dye-sensitized solar cells., https://www.printedelectronicsworld.com/articles/4062/tanaka-exclusively-supply-ruthenium-dye-for-dye-sensitized-solar-cells, (accessed 16/08/2019).
22. J. Zhao, S. Ji and H. Guo, *RSC Advances*, 2011, **1**, 937-950.
23. R. P. Wayne, *Principles and applications of photochemistry*, Oxford University Press, Incorporated, 1988.
24. W. Wu, H. Guo, W. Wu, S. Ji and J. Zhao, *The Journal of Organic Chemistry*, 2011, **76**, 7056-7064.
25. Y. Lu, J. Wang, N. McGoldrick, X. Cui, J. Zhao, C. Caverly, B. Twamley, G. M. Ó Máille, B. Irwin, R. Conway-Kenny and S. M. Draper, *Angewandte Chemie International Edition*, 2016, **55**, 14688-14692.
26. J. Wang, Y. Lu, N. McGoldrick, C. Zhang, W. Yang, J. Zhao and S. M. Draper, *Journal of Materials Chemistry C*, 2016, **4**, 6131-6139.
27. Y. Lu, R. Conway-Kenny, B. Twamley, N. McGoldrick, J. Zhao and S. M. Draper, *ChemPhotoChem*, 2017, **1**, 534-534.
28. Y. Lu, R. Conway-Kenny, J. Wang, X. Cui, J. Zhao and S. M. Draper, *Dalton Transactions*, 2018, **47**, 8585-8589.
29. J. Wang, Y. Lu, W. McCarthy, R. Conway-Kenny, B. Twamley, J. Zhao and S. M. Draper, *Chemical Communications*, 2018, **54**, 1073-1076.
30. S. M. Borisov and I. Klimant, *Analytical Chemistry*, 2007, **79**, 7501-7509.
31. J. B. Birks, *The Journal of Physical Chemistry*, 1963, **67**, 2199-2200.
32. V. Gray, D. Dzebo, M. Abrahamsson, B. Albinsson and K. Moth-Poulsen, *Physical Chemistry Chemical Physics*, 2014, **16**, 10345-10352.
33. J.-H. Kim, F. Deng, F. N. Castellano and J.-H. Kim, *ACS Photonics*, 2014, **1**, 382-388.
34. X. Cui, A. M. El-Zohry, Z. Wang, J. Zhao and O. F. Mohammed, *The Journal of Physical Chemistry C*, 2017, **121**, 16182-16192.
35. R. W. MacQueen, Y. Y. Cheng, A. N. Danos, K. Lips and T. W. Schmidt, *RSC Advances*, 2014, **4**, 52749-52756.
36. Y. Y. Cheng, B. Fückel, T. Khoury, R. G. C. R. Clady, M. J. Y. Tayebjee, N. J. Ekins-Daukes, M. J. Crossley and T. W. Schmidt, *The Journal of Physical Chemistry Letters*, 2010, **1**, 1795-1799.
37. W. Wu, W. Wu, S. Ji, H. Guo and J. Zhao, *Dalton Transactions*, 2011, **40**, 5953-5963.
38. J. Zhao, S. Ji, W. Wu, W. Wu, H. Guo, J. Sun, H. Sun, Y. Liu, Q. Li and L. Huang, *RSC Advances*, 2012, **2**, 1712-1728.
39. J. Zhao, W. Wu, J. Sun and S. Guo, *Chemical Society Reviews*, 2013, **42**, 5323-5351.
40. X. Cui, C. Zhang, K. Xu and J. Zhao, *Journal of Materials Chemistry C*, 2015, **3**, 8735-8759.
41. W. Yang and J. Zhao, *European Journal of Inorganic Chemistry*, 2016, **2016**, 5283-5299.
42. S. Baluschev, T. Miteva, V. Yakutkin, G. Nelles, A. Yasuda and G. Wegner, *Physical Review Letters*, 2006, **97**, 143903.
43. R. R. Islangulov, J. Lott, C. Weder and F. N. Castellano, *Journal of the American Chemical Society*, 2007, **129**, 12652-12653.
44. S. Baluschev, V. Yakutkin, G. Wegner, T. Miteva, G. Nelles, A. Yasuda, S. Chernov, S. Aleshchenkov and A. Cheprakov, *Applied Physics Letters*, 2007, **90**, 181103.
45. X. Zhiqing, Z. Yi, C. Jinping, Y. Tianjun, Z. Xiaohui, Y. Guoqiang and L. Yi, *Chemistry – A European Journal*, 2016, **22**, 8654-8662.
46. K. Börjesson, P. Rudquist, V. Gray and K. Moth-Poulsen, *Nature Communications*, 2016, **7**, 12689.
47. A. Fukuzaki, H. Kawai, T. Sano, K. Takehara and T. Nagamura, *ACS Biomaterials Science & Engineering*, 2017, **3**, 1809-1814.
48. H. Guo, S. Ji, W. Wu, W. Wu, J. Shao and J. Zhao, *Analyst*, 2010, **135**, 2832-2840.

49. W. Wu, J. Zhao, J. Sun, L. Huang and X. Yi, *Journal of Materials Chemistry C*, 2013, **1**, 705-716.
50. H. Sun, H. Guo, W. Wu, X. Liu and J. Zhao, *Dalton Transactions*, 2011, **40**, 7834-7841.
51. V. Balzani and S. Campagna, *Photochemistry and Photophysics of Coordination Compounds II*, Springer Berlin Heidelberg, 2007.
52. V. Balzani and S. Campagna, *Photochemistry and Photophysics of Coordination Compounds II*, Springer Berlin Heidelberg, 2010.
53. D. V. Kozlov and F. N. Castellano, *Chemical Communications*, 2004, DOI: 10.1039/B412681E, 2860-2861.
54. M. A. Filatov, F. Etzold, D. Gehrig, F. Laquai, D. Busko, K. Landfester and S. Baluschev, *Dalton Transactions*, 2015, **44**, 19207-19217.
55. K. A. El Roz and F. N. Castellano, *Chemical Communications*, 2017, **53**, 11705-11708.
56. K. Kamada, Y. Sakagami, T. Mizokuro, Y. Fujiwara, K. Kobayashi, K. Narushima, S. Hirata and M. Vacha, *Materials Horizons*, 2017, **4**, 83-87.
57. C. D. Ertl, C. Momblona, A. Pertegás, J. M. Junquera-Hernández, M.-G. La-Placa, A. Prescimone, E. Ortí, C. E. Housecroft, E. C. Constable and H. J. Bolink, *Journal of the American Chemical Society*, 2017, **139**, 3237-3248.
58. U. M. Tefashe, Q. V. Nguyen, F. Lafolet, J.-C. Lacroix and R. L. McCreery, *Journal of the American Chemical Society*, 2017, **139**, 7436-7439.
59. L.-S. Wang, Y. Lu, G. M. Ó. Máille, S. P. Anthony, D. Nolan and S. M. Draper, *Inorganic Chemistry*, 2016, **55**, 9497-9500.
60. Y. Wang, S. Wang, J. Ding and L. Wang, *ACS Omega*, 2018, **3**, 15308-15314.
61. H. S. Askes, S. M. Meijer, T. Bouwens, I. Landman and S. Bonnet, *Molecules*, 2016, **21**.
62. V. Balzani and S. Campagna, *Photochemistry and Photophysics of Coordination Compounds I*, Springer Berlin Heidelberg, 2007.
63. F. G. Gao and A. J. Bard, *Journal of the American Chemical Society*, 2000, **122**, 7426-7427.
64. J. D. Nguyen, E. M. D'Amato, J. M. R. Narayanam and C. R. J. Stephenson, *Nature Chemistry*, 2012, **4**, 854.
65. H. Shahroosvand, L. Heydari, B. N. Bideh, B. Pashaei, S. Tarighi and B. Notash, *ACS Omega*, 2018, **3**, 9981-9988.
66. H.-C. Chen, C.-Y. Hung, K.-H. Wang, H.-L. Chen, W. S. Fann, F.-C. Chien, P. Chen, T. J. Chow, C.-P. Hsu and S.-S. Sun, *Chemical Communications*, 2009, DOI: 10.1039/B905572J, 4064-4066.
67. Y. Chen, J. Zhao, L. Xie, H. Guo and Q. Li, *RSC Advances*, 2012, **2**, 3942-3953.
68. J. Zhao, K. Chen, Y. Hou, Y. Che, L. Liu and D. Jia, *Organic & Biomolecular Chemistry*, 2018, **16**, 3692-3701.
69. T. N. Singh-Rachford and F. N. Castellano, *The Journal of Physical Chemistry A*, 2009, **113**, 5912-5917.
70. P. Yang, W. Wu, J. Zhao, D. Huang and X. Yi, *Journal of Materials Chemistry*, 2012, **22**, 20273-20283.
71. S. Guo, J. Sun, L. Ma, W. You, P. Yang and J. Zhao, *Dyes and Pigments*, 2013, **96**, 449-458.
72. D. Huang, J. Zhao, W. Wu, X. Yi, P. Yang and J. Ma, *Asian Journal of Organic Chemistry*, 2012, **1**, 264-273.
73. H. Dandan, Z. Jianzhang, W. Wanhua, Y. Xiuyu, Y. Pei and M. Jie, *Asian Journal of Organic Chemistry*, 2012, **1**, 264-273.
74. P. Majumdar, R. Nomula and J. Zhao, *Journal of Materials Chemistry C*, 2014, **2**, 5982-5997.
75. S. Wang, A. Bi, W. Zeng and Z. Cheng, *Journal of Materials Chemistry B*, 2016, **4**, 5331-5348.
76. Y. Liu, X. Meng and W. Bu, *Coordination Chemistry Reviews*, 2019, **379**, 82-98.

77. M. R. Hamblin, *Dalton Transactions*, 2018, **47**, 8571-8580.
78. H. V. Tappeiner, *Med Wochenschr*, 1903, **47**, 2024.
79. V. Balzani, P. Ceroni and A. Juris, *Photochemistry and Photophysics: Concepts, Research, Applications*, Wiley, 2014.
80. P. Xueting, B. Lixin, W. Hui, W. Qingyuan, W. Hongyu, L. Shuang, X. Bolong, S. Xinghua and L. Huiyu, *Advanced Materials*, 2018, **30**, 1800180.
81. G. Canavese, A. Ancona, L. Racca, M. Canta, B. Dumontel, F. Barbaresco, T. Limongi and V. Cauda, *Chemical Engineering Journal*, 2018, **340**, 155-172.
82. C. Biray Avci, *Journal of Drug Targeting*, 2018, DOI: 10.1080/1061186X.2018.1527338, 1-5.
83. Z. Gu, S. Zhu, L. Yan, F. Zhao and Y. Zhao, *Advanced Materials*, **0**, 1800662.
84. C. Geng, Y. Zhang, T. H. Hidru, L. Zhi, M. Tao, L. Zou, C. Chen, H. Li and Y. Liu, *Life Sciences*, 2018, **207**, 304-313.
85. F. Giuntini, F. Foglietta, A. M. Marucco, A. Troia, N. V. Dezhkunov, A. Pozzoli, G. Durando, I. Fenoglio, L. Serpe and R. Canaparo, *Free Radical Biology and Medicine*, 2018, **121**, 190-201.
86. N. Armaroli, P. Ceroni, V. Balzani, J.-M. Kern, J.-P. Sauvage and J.-L. Weidmann, *Journal of the Chemical Society, Faraday Transactions*, 1997, **93**, 4145-4150.
87. G. Accorsi, A. Listorti, K. Yoosaf and N. Armaroli, *Chemical Society Reviews*, 2009, **38**, 1690-1700.
88. A. Listorti, A. Degli Esposti, R. S. K. Kishore, V. Kalsani, M. Schmittel and N. Armaroli, *The Journal of Physical Chemistry A*, 2007, **111**, 7707-7718.
89. M. Gogoi and A. Chattopadhyay, *RSC Advances*, 2016, **6**, 103095-103105.
90. F. Monti, U. Hahn, E. Pavoni, B. Delavaux-Nicot, J. F. Nierengarten and N. Armaroli, *Polyhedron*, 2014, **82**, 122-131.
91. P. Gayathri and A. Senthil Kumar, *Langmuir*, 2014, **30**, 10513-10521.
92. C.-L. Xiao, C.-Z. Wang, L.-Y. Yuan, B. Li, H. He, S. Wang, Y.-L. Zhao, Z.-F. Chai and W.-Q. Shi, *Inorganic Chemistry*, 2014, **53**, 1712-1720.
93. D. Tzalis and Y. Tor, *Journal of the American Chemical Society*, 1997, **119**, 852-853.
94. P. J. Connors, D. Tzalis, A. L. Dunnick and Y. Tor, *Inorganic Chemistry*, 1998, **37**, 1121-1123.
95. D. Tzalis and Y. Tor, *Chemical Communications*, 1996, DOI: 10.1039/CC9960001043, 1043-1044.
96. M. Hissler, W. B. Connick, D. K. Geiger, J. E. McGarrah, D. Lipa, R. J. Lachicotte and R. Eisenberg, *Inorganic Chemistry*, 2000, **39**, 447-457.
97. W. Yang and T. Nakano, *Chemical Communications*, 2015, **51**, 17269-17272.
98. V. Dénes and R. Chira, *Journal für Praktische Chemie*, 1978, **320**, 172-175.
99. S. Ji, W. Wu, W. Wu, P. Song, K. Han, Z. Wang, S. Liu, H. Guo and J. Zhao, *Journal of Materials Chemistry*, 2010, **20**, 1953-1963.
100. H. Guo, M. L. Muro-Small, S. Ji, J. Zhao and F. N. Castellano, *Inorganic Chemistry*, 2010, **49**, 6802-6804.
101. J. Sun, W. Wu, H. Guo and J. Zhao, *European Journal of Inorganic Chemistry*, 2011, **2011**, 3165-3173.
102. X. Yang, Z. Feng, J. Dang, Y. Sun, G. Zhou and W.-Y. Wong, *Materials Chemistry Frontiers*, 2019, DOI: 10.1039/C8QM00548F.
103. T. A. Niehaus, T. Hofbeck and H. Yersin, *RSC Advances*, 2015, **5**, 63318-63329.

Appendix

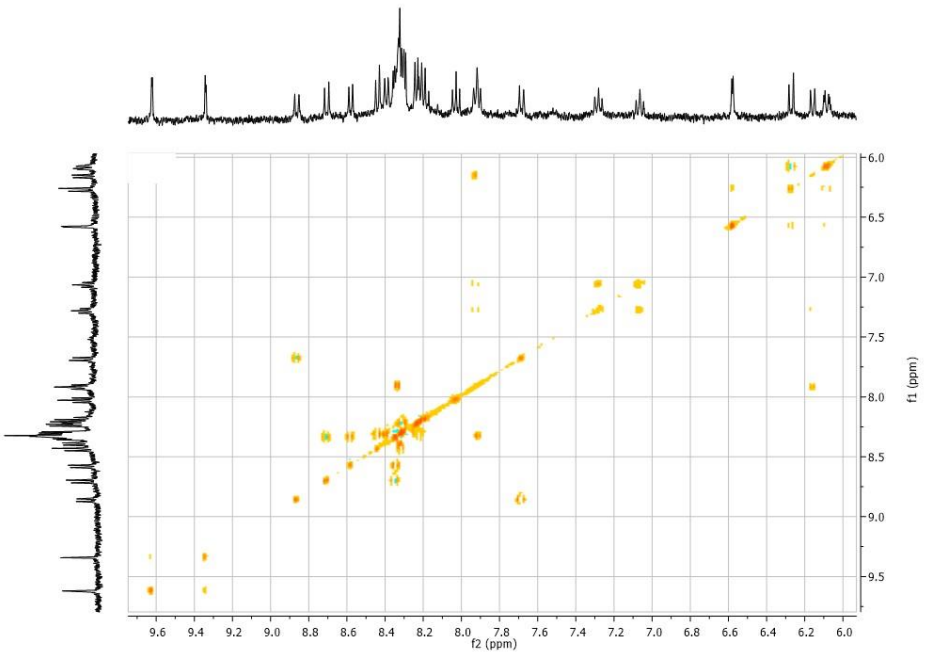

***Figure A.1**: The ^{1}H-^{1}H COSY of **Ir1**.*

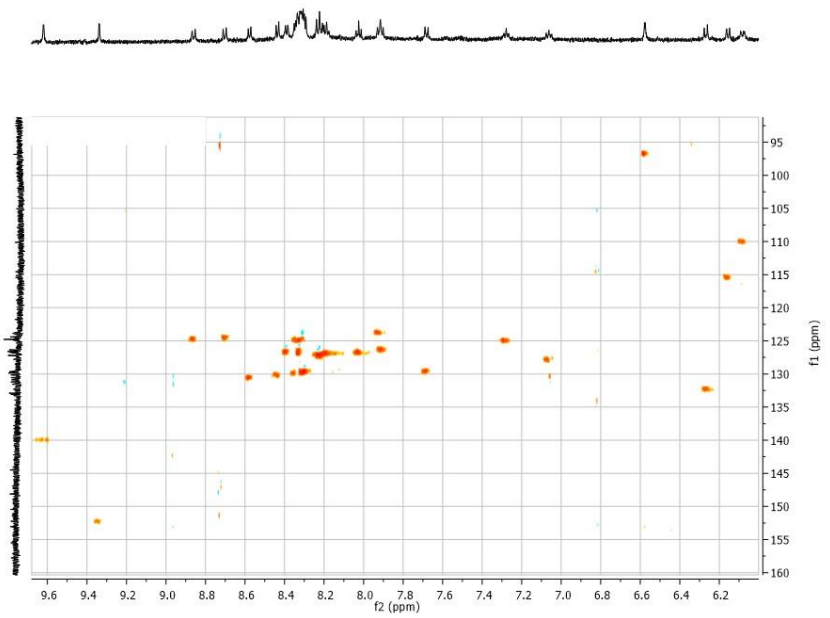

***Figure A.2**: The HSQC spectrum of **Ir1**.*

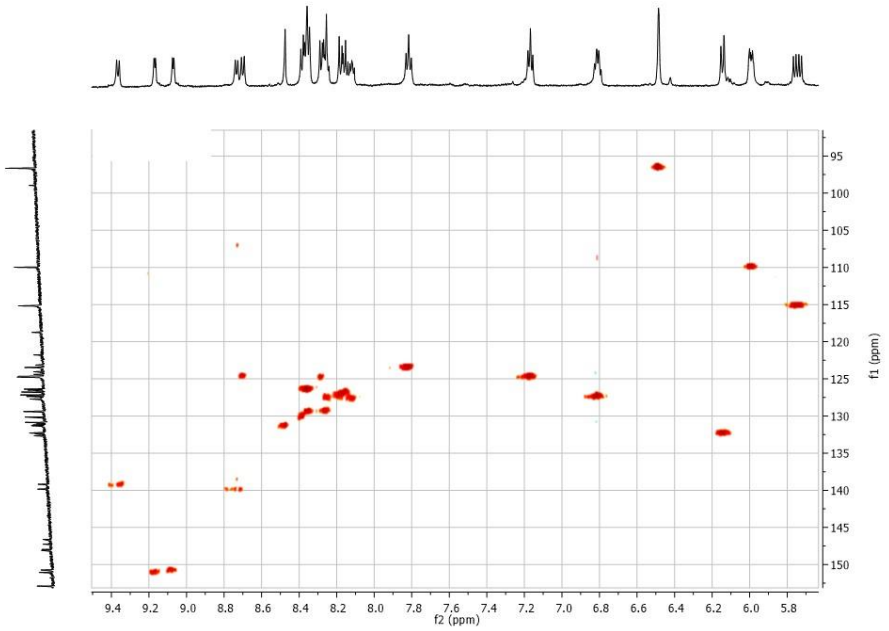

***Figure A.3**: The HSQC spectrum of **Ir2**.*

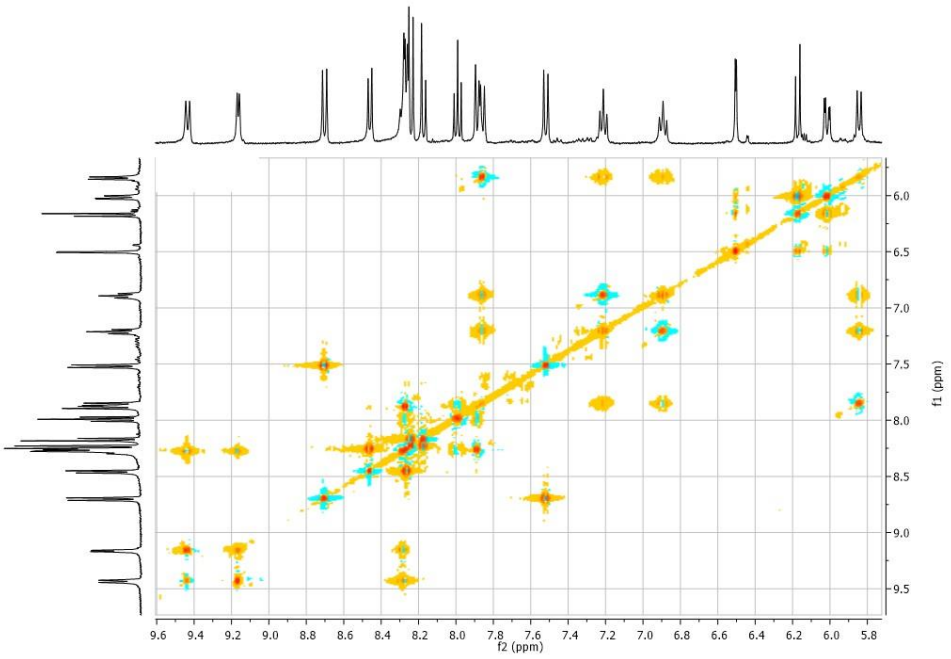

***Figure A.4**: The ^{1}H-^{1}H COSY of **Ir3**.*

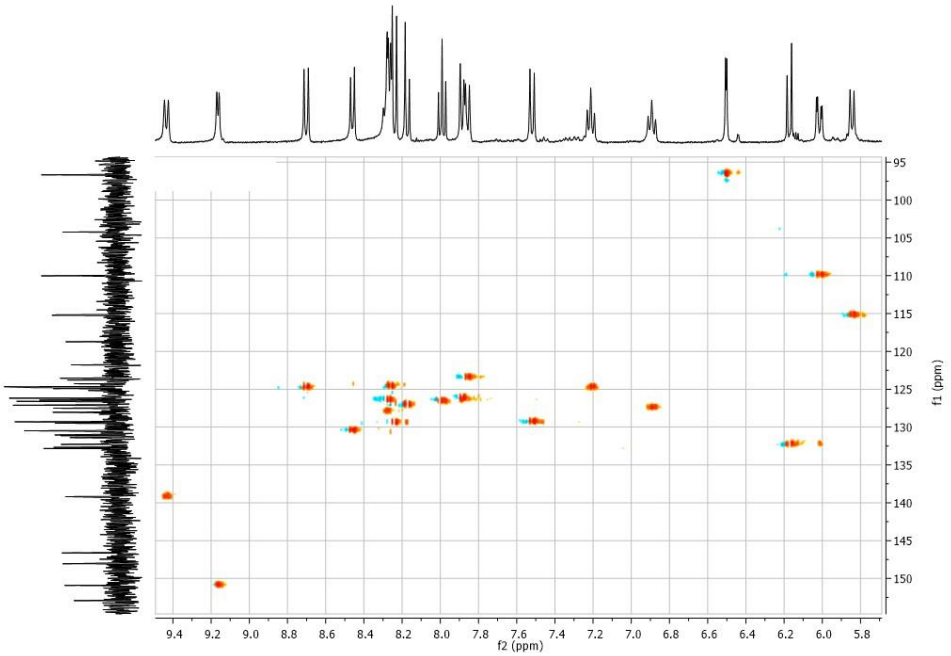

***Figure A.5**: The HSQC spectrum of **Ir3**.*

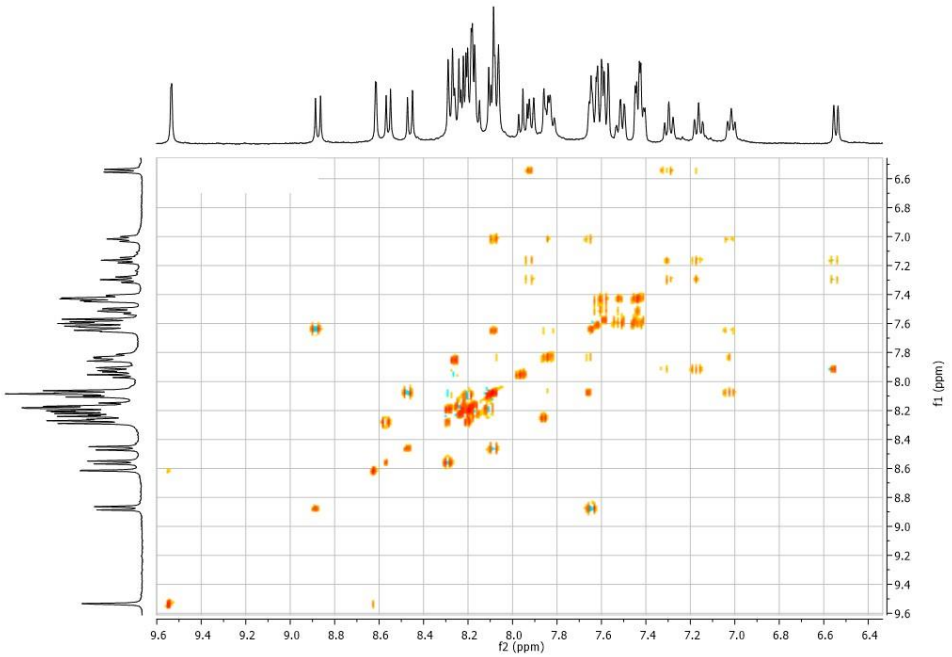

***Figure A.6**: The ^{1}H-^{1}H COSY of **Ir4**.*

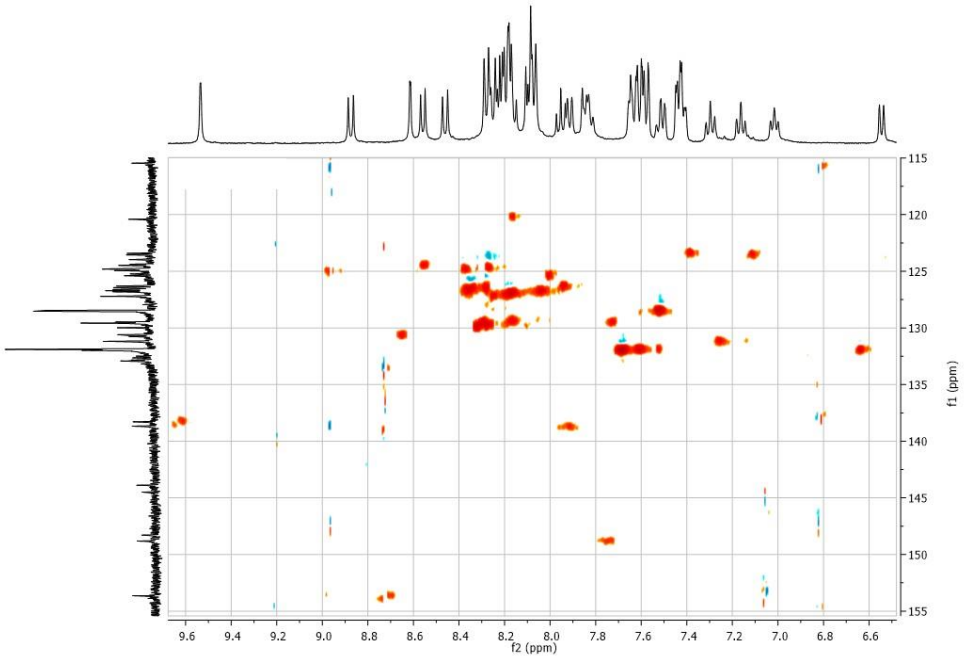

***Figure A.7**: The HSQC spectrum of **Ir4**.*

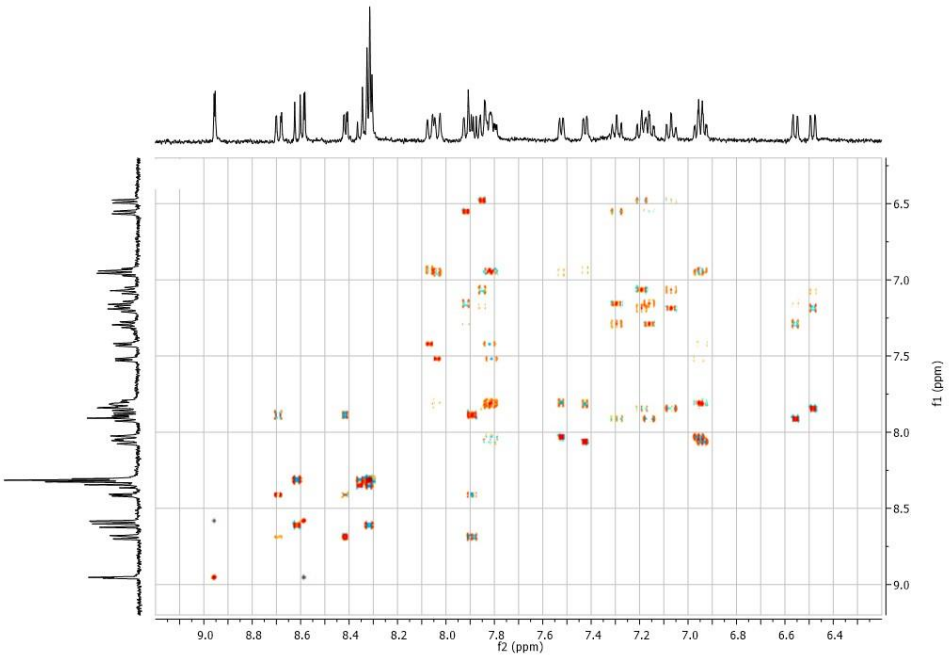

***Figure A.8**: The ^{1}H-^{1}H COSY of **Ir5**.*

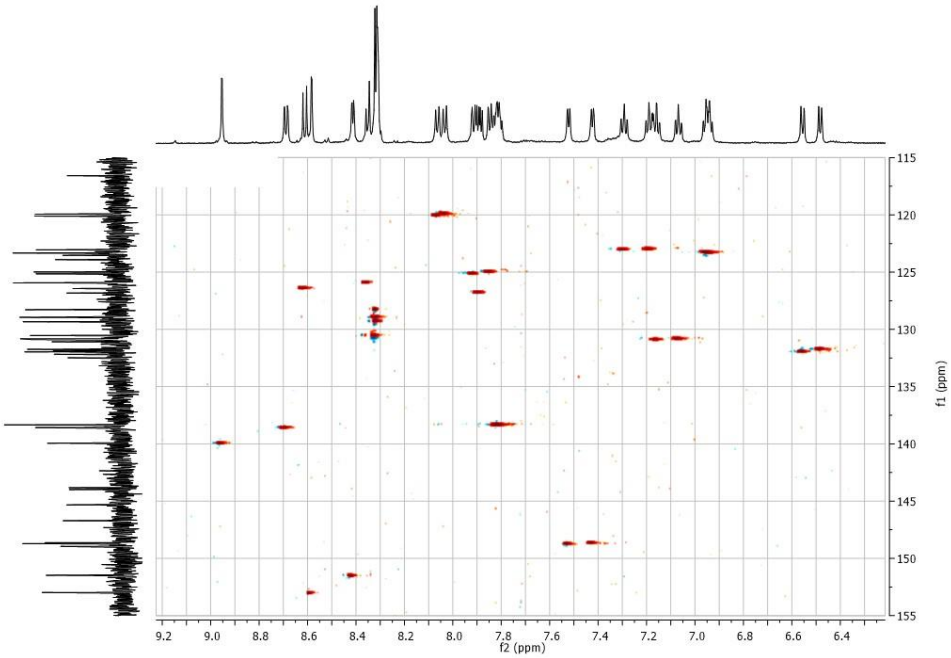

***Figure A.9**: The HSQC spectrum of **Ir5**.*

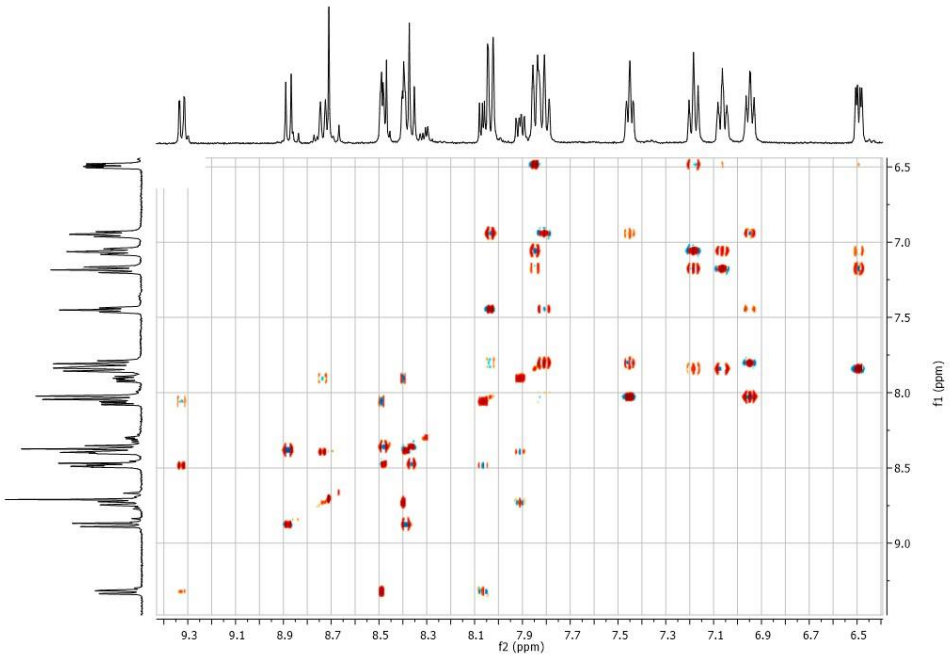

***Figure A.10**: The ^{1}H-^{1}H COSY of **Ir6**.*

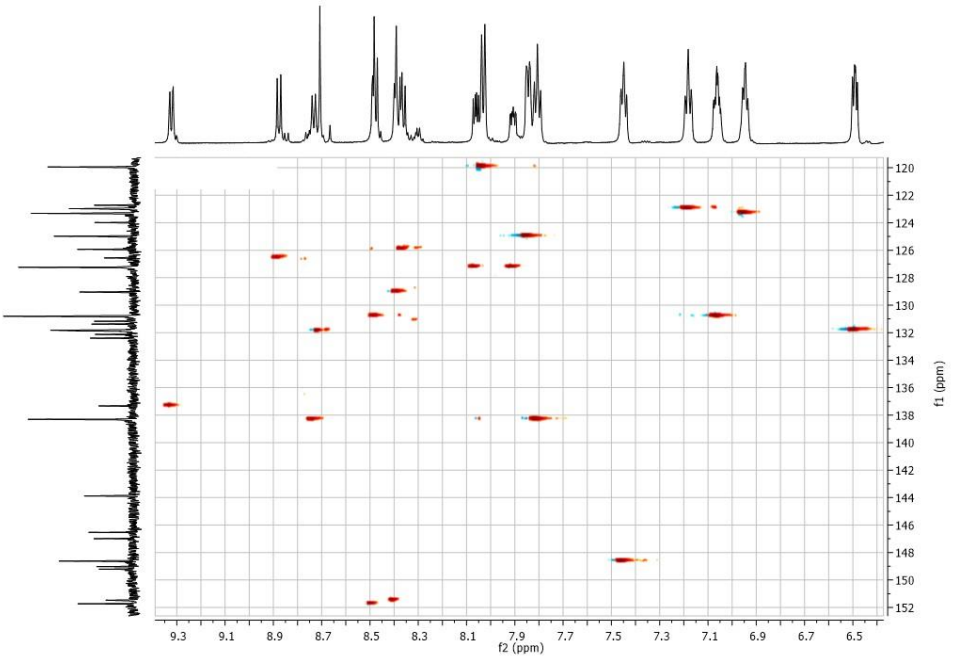

***Figure A.11**: The HSQC spectrum of **Ir6**.*

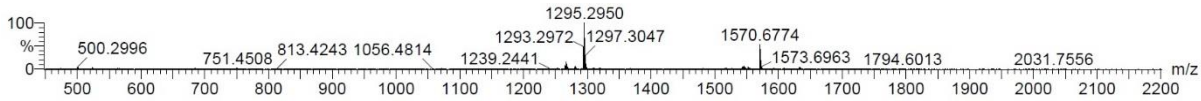

***Figure A.12**: The mass spectrometry spectrum of **Ir1**, showing the peak of the product at 1295.2950.*